



UNIVERSITÀ DEGLI STUDI DI PADOVA

FACOLTÀ DI INGEGNERIA

CORSO DI LAUREA SPECIALISTICA IN
INGEGNERIA DELLE TELECOMUNICAZIONI

TESI DI LAUREA

STUDY OF AN
OPTICAL CHAOTIC STEGANOGRAPHIC
FREE SPACE SYSTEM

RELATORE: Ing. Marco Santagiustina

CORRELATORE: Ing. Leonora Ursini

LAUREANDO: *Fabrizio Chiarello*

Padova, 20 Aprile 2010
Anno Accademico 2009 - 2010

Sommario

La ricerca di metodi per la trasmissione sicura di informazioni ricopre un ruolo sempre più centrale nelle moderne reti di telecomunicazione. In particolare, la protezione delle comunicazioni in spazio libero è di importanza cruciale, poiché, in tali ambienti, i collegamenti sono facilmente accessibili da eventuali intrusioni esterne.

Sin dall'antichità, una moltitudine di metodi per lo scambio sicuro di messaggi sono stati implementati mediante l'uso della *crittografia*¹ e della *steganografia*². L'occultamento del messaggio, in un sistema steganografico, può essere realizzato sfruttando in modo opportuno il concetto di *caos deterministico*³, che può essere definito come il comportamento totalmente aperiodico e apparentemente casuale di alcuni sistemi non lineari, la cui evoluzione, completamente deterministica, è fortemente influenzata da un'elevata dipendenza dalle condizioni iniziali e da qualsiasi perturbazione esterna. In particolare, piccole variazioni nelle condizioni iniziali di un sistema caotico determinano una divergenza esponenziale della sua evoluzione dalla traiettoria originale.

La sincronizzazione del caos è una caratteristica peculiare dei sistemi caotici, scoperta da L. Pecora e T. Carroll, a metà degli anni '80: un sistema caotico, chiamato *master*, può, sotto opportune condizioni, forzare un sistema simile, chiamato *slave*, a seguire la sua stessa evoluzione [1]. Questo fenomeno viene usato nei sistemi di comunicazione caotica per ottenere un elevato livello di sicurezza tra il trasmettitore e il ricevitore. In particolare, al trasmettitore di un sistema caotico steganografico, un dispositivo non lineare (ad esempio un laser) viene indotto in un regime caotico attraverso un'appropriata configurazione a retroazione, e un messaggio viene sovrapposto alla portante caotica così generata, ottenendo la steganografia del messaggio. Al ricevitore, il processo di sincronizzazione con lo slave permette il recupero del messaggio, mediante un'operazione di differenza e un opportuno filtraggio. L'efficacia di tale tecnica si basa sulla qualità della sincronizzazione, che dipende prima di tutto dalla disponibilità di una coppia di master-slave avente parametri molto simili, e inoltre dall'influenza degli effetti distorsivi e del rumore introdotti dal canale di trasmissione.

In questa Tesi viene studiato numericamente un sistema di comunicazione steganografica su portante ottica caotica in spazio libero. La portante caotica viene generata, al trasmettitore, mediante l'utilizzo di un laser a semiconduttore con retroazione optoelet-

¹crittografia: dalle parole greche “*kryptós*” (nascosto), e “*gráphein*” (scrivere), significa nascondere il significato di un messaggio.

²steganografia: dalle parole greche “*stéganos*” (segreto), e “*gráphein*” (scrivere), significa nascondere l'esistenza stessa di un messaggio.

³Nell'uso comune, la parola *caos* denota una assenza di ordine, e sembrerebbe un controsenso affiancarla al concetto di *determinismo*, che significa ordine. La spiegazione risiede nella definizione matematica di caos, cioè quella di un sistema deterministico non lineare, dal quale, in particolari circostanze, può emergere un disordine apparente.

tronica ritardata. Il messaggio, assunto con codifica PPM⁴, viene poi sovrapposto alla portante caotica così generata. Al ricevitore il messaggio viene recuperato usando un laser a semiconduttore, simile a quello usato al trasmettitore, in configurazione ad anello aperto.

Le prestazioni del sistema sono valutate numericamente in termini dell'errore di sincronizzazione e del fattore Q misurato in due diversi punti del sistema. L'analisi delle prestazioni è volta a determinare sia la qualità della copertura del messaggio in trasmissione (un ascoltatore non autorizzato non deve essere in grado di recuperare il messaggio), sia la qualità di recupero dell'informazione in ricezione, dopo la sincronizzazione. Una accurata analisi numerica è effettuata prima in configurazione back to back (BTB), ovvero in assenza del canale, e poi considerando la propagazione in spazio libero all'interno di un ambiente chiuso.

Il lavoro di Tesi è dunque lo studio e l'analisi numerica di un modello matematico per la generazione e la sincronizzazione del caos ottico mediante laser a semiconduttore, del loro utilizzo al fine di realizzare la steganografia caotica di un messaggio, e degli effetti introdotti da una propagazione in spazio libero.

⁴La codifica pulse position modulation (PPM) è utilizzata in molti standard per le comunicazioni ottiche nell'infrarosso, per esempio negli standard IEEE 802.11 e Irda.

To anyone who can see the world
through the eyes of a child.

Acknowledgments

First of all, I wish to thank my parents for allowing me to get here.

I would like to thank my supervisor *Ing. Marco Santagiustina* for providing me the opportunity to work on this Thesis, and his assistant *Ing. Leonora Ursini* for her guidance and support.

I am grateful to all my friends and “CdSA” senior members, who allowed me to live happily these last years. In particular, a special thank goes to *Davide, Luca & Luca* and *Simone* for the invaluable discussions and suggestions we had in front of the “quantum” coffee machine (located somewhere at DEI, usually between the ground floor and the 2nd floor); to *Gabriele, Andrea, Chris & Chris* and *Stefano* for their sincere friendship, and to *Nicola* for giving us an excuse to go to Bassano from time to time.

Fabrizio

Abstract

An optical communication system for the secure transmission of an information message in free-space is investigated.

The message hiding, at the transmitter, is achieved by a steganographic encryption process onto an optical chaotic carrier generated by a semiconductor laser subjected to delayed optoelectronic feedback.

The message recovery, at the receiver, is attained by subtracting the received signal from a reconstructed carrier obtained through the synchronization of a semiconductor laser similar to that used at the transmitter.

A detailed numerical analysis of the system performance is performed for various configurations. The aim is to determine the quality of both the message masking and recovering.

Contents

1	Introduction	1
1.1	Overview of the Thesis	3
2	Semiconductor Lasers	5
2.1	Conditions for Laser Oscillation	5
2.1.1	Effective Refractive Index	8
2.1.2	Free Spectral Range	10
2.1.3	Photon Density	10
2.1.4	Carrier Induced Frequency Shift	11
2.2	Derivation of the Rate Equations	13
2.2.1	Gain at Laser Oscillation	13
2.2.2	Rate Equation for the Electric Field	13
2.2.3	The Linewidth Enhancement Factor	15
2.2.4	Rate Equation for the Photon Density	15
2.2.5	Rate Equation for the Carrier Density	16
3	Chaos in Semiconductor Lasers	17
3.1	What is Chaos?	17
3.2	Chaos Synchronization	18
3.2.1	The Complete Replacement Method	19
3.2.2	The Active-Passive Method	20
3.3	Chaotic Lasers	21
3.3.1	Chaotic Lasers with Delayed Optoelectronic Feedback	22
3.3.2	Synchronization of Semiconductor Lasers with Optoelectronic Feedback	26
4	Chaotic Communication System	31
4.1	Overview of the System	31
4.2	The Source	32
4.2.1	PPM Encoder	33
4.3	The Transmitter	33
4.4	The Channel	35
4.4.1	Model of the Channel	35
4.4.2	Back To Back Channel	37
4.4.3	Indoor Channel	37
4.5	The Receiver	41
4.6	Message Decoding	44

4.6.1	PPM decoder	44
4.6.2	Symbol Error Probability	45
4.6.3	Bit Error Probability	46
4.6.4	Bit Error Rate and Q Factor	46
4.7	System Performance	47
4.7.1	Example	47
5	Numerical Analysis	51
5.1	System Specifications	51
5.2	Modulation Depth	52
5.3	Lasers Mismatches	53
5.4	The Role of the Relaxation Frequency f_r	57
5.5	Line of Sight Propagation	61
5.6	Multipath impairments	63
	Conclusions	71
A	Numeric Integration Scheme	73
A.1	Heun's Method	73
A.2	Stochastic Differential Equations	74
B	Photodetection	77
B.1	Photodiodes	77
B.1.1	Noise in Photodiodes	79
B.2	Preamplifiers	80
B.2.1	Noise in Preamplifiers	80
	References	84

List of Figures

2.1	Model of a Fabry-Perot resonant cavity.	6
2.2	Possible frequencies of oscillation for longitudinal modes in a Fabry-Perot cavity.	8
2.3	Front view of a buried double heterostructure edge emitting semiconductor laser with a single active region [10].	8
2.4	Linewidth broadening in a semiconductor laser due to changes in carrier density.	12
3.1	Time evolution of the Lorenz's attractor (the "butterfly").	18
3.2	Different realizations of the Lorenz's attractor.	19
3.3	Schematic diagram of a semiconductor laser with delayed all-optical feedback.	22
3.4	Schematic diagram of a semiconductor laser with delayed optoelectronic feedback.	22
3.5	Different realizations of the output power of the same laser.	23
3.6	Optical output of a semiconductor laser with optoelectronic feedback for various normalized feedback delay times $\hat{\tau}$	25
3.7	Schematic diagram of the connection from master to slave for synchronization.	27
3.8	Outputs of the ML and SL with matched parameters.	29
3.9	Synchronization diagram of the outputs of the ML and SL with matched parameters.	29
3.10	Outputs of the ML and SL with a difference of 10% in the SL differential gain parameter g_N in respect to that of the ML.	30
3.11	Synchronization diagram of the outputs of the ML and SL, when the differential gain parameter g_N of the SL differ of 10% from that of the ML.	30
4.1	Generic model of a digital communication system.	32
4.2	Chaotic communication channel.	32
4.3	Scheme of a PPM encoder.	32
4.4	M -PPM signal structure for symbol $l = 1$ and pulse $g(t) = \text{rect}(t)$	34
4.5	Signals used in 4-PPM.	34
4.6	Example of a 4-PPM encoded signal compared to a standard NRZ encoding.	34
4.7	Scheme of the transmitter.	35
4.8	Example of a message injection onto a chaotic optical carrier.	36
4.9	Model of an infrared channel.	36
4.10	Model of an indoor environment.	38

4.11	Source and receiver specification.	38
4.12	Geometric model for LOS propagation.	39
4.13	Example of k -bounces impulse responses.	42
4.14	DC gain of the components shown in Fig. 4.13.	43
4.15	Scheme of the receiver.	43
4.16	Block scheme of a PPM decoder.	44
4.17	Block scheme of a MLD [37].	44
4.18	Q factor vs. BER.	47
4.19	Example of a message as seen by Alice, Bob and Eve for the CMS scheme with a modulation depth of $\zeta = 0.03$	48
4.20	Frame level eye diagrams as seen by Bob and Eve for the CMS scheme with a modulation depth of $\zeta = 0.03$	48
4.21	Example of a message as seen by Alice, Bob and Eve for the CMS scheme with a modulation depth of $\zeta = 0.2$	49
4.22	Frame level eye diagrams as seen by Bob and Eve for the CMS scheme with a modulation depth of $\zeta = 0.2$	49
4.23	Example of a message as seen by Alice, Bob and Eve for the CMS scheme, where the receiver differs of 10% in the SL differential gain parameters g_N in respect to that of the ML.	50
4.24	Frame level eye diagrams as seen by Bob and Eve for the CMS scheme, where the receiver differs of 10% in the SL differential gain parameters g_N in respect to that of the ML.	50
5.1	Synchronization error vs. bit rate for various modulation depths ζ	54
5.2	Q factor for Eve vs. bit rate for various modulation depths ζ	54
5.3	Q factor for Bob vs. bit rate for various modulation depths ζ	55
5.4	Q factor vs. modulation depth ζ , for a bit rate of $R_{\text{bit}} = 150 \text{ Mbit s}^{-1}$	55
5.5	Q factor vs. bit rate R_{bit} , for a modulation depth of $\zeta = 0.03$	56
5.6	Q factor vs. SL gain parameter g_N variation in respect to that of the ML.	56
5.7	Synchronization error vs. bit rate for various PPM orders, CMS case.	58
5.8	Synchronization error vs. bit rate for various PPM orders, ACM case.	58
5.9	Q factor for Bob vs. bit rate for various PPM orders, CMS case.	59
5.10	Q factor for Bob vs. bit rate for various PPM orders, ACM case.	59
5.11	Q factor for Eve vs. bit rate for various PPM orders, CMS case.	60
5.12	Q factor for Eve vs. bit rate for various PPM orders, ACM case.	60
5.13	Synchronization error vs. LOS DC gain.	62
5.14	Q factor for Bob vs. LOS DC gain.	62
5.15	Sketch of the indoor environment used in simulations.	63
5.16	Channel DC gain and delay vs. transmitter azimuth.	64
5.17	Channel DC gain and delay vs. distance.	65
5.18	Channel DC gain and delay vs. transmitter HWHM.	65
5.19	Channel LOS to non-LOS ratio vs. transmitter azimuth.	66
5.20	Indoor Q factor vs. distance.	66
5.21	Indoor Q factor vs. transmitter HWHM.	67
5.22	Indoor Q factor vs. transmitter azimuth.	67
5.23	Indoor Q factor vs. transmitter azimuth, with a transmitter HWHM of 5 deg.	68

5.24	Indoor synchronization error vs. transmitter azimuth, with a transmitter HWHM of 5 deg.	68
5.25	Indoor Q factor vs. LOS to non-LOS ratio.	69
5.26	Indoor synchronization error vs. LOS to non-LOS ratio.	69
5.27	Indoor Q factor vs. LOS to non-LOS ratio, for a bit rate of $R_{\text{bit}} = 250 \text{ Mbit s}^{-1}$	70
5.28	Indoor Q factor vs. LOS to non-LOS ratio, by only considering an unmasked message propagation.	70
B.1	Scheme of a photodiode connection.	78
B.2	Schematic of the equivalent circuit of a photodiode.	78
B.3	Schematic of a transimpedance amplifier.	80

List of Tables

4.1	Bit mapping for 4-PPM.	33
4.2	Parameters used for the channel of Fig. 4.13.	42
5.1	Parameters of the semiconductor lasers.	52
5.2	Parameters of the photodetectors.	53

List of Acronyms

ACM	additive chaos modulation. 35, 53, 57, 61, 64
APD	avalanche photodiode. 77
AWGN	additive white Gaussian noise. 45
BER	bit error rate. 46
BTB	back to back. iv, 2, 37, 51, 63, 71
CMS	chaos masking. 35, 47, 53, 57, 61
DC	direct current. 37, 40, 41, 63
DD	direct detection. 41, 47
EHP	electron-hole pair. 77
FSR	free spectral range. 10
HWHM	half-width at half-maximum. 12, 39, 63
ISO/OSI	International Standard Organization/Open System Interconnection. 32
IVP	initial value problem. 73
LOS	line of sight. 39, 41, 51, 61, 63, 64, 71
LPF	low-pass filter. 41
ML	master laser. 27, 28, 35, 41, 47, 51, 53
MLD	maximum likelihood detector. 44
NRZ	Non Return to Zero. 33, 34
ODE	ordinary differential equation. 73
p-i-n	positive-intrinsic-negative. 77, 78
PHY/IR	infrared physical layer. 31
PPM	pulse position modulation. iv, 2, 32–34, 43, 44, 52, 57, 64
PSD	power spectral density. 79

SDE	stochastic differential equation. 74
SHS	stochastic Heun's scheme. 74
SL	slave laser. 27, 28, 41, 47, 53, 61
SVEA	slowly varying envelope approximation. 13
TIA	trans-impedance amplifier. 80

Chapter 1

Introduction

$$e^{j\pi} + 1 = 0$$

Leonhard Paul Euler (1707 – 1783)

In modern world-wide communication networks, the research of methods for the secure transmission of critical information is gaining more and more attention. In particular, the protection of free-space communications is of a crucial importance, since in such environments the communication is easily accessible by an eavesdropper.

Since the ancient times, several methods to secure a message have been implemented, through *cryptography*¹ and *steganography*². The process of hiding a message in a steganographic system can be achieved by opportunely exploiting the concept of *deterministic chaos*³, which can be defined as a totally aperiodic and apparently random behavior of some nonlinear systems, whose evolution is completely deterministic, but strongly dependent on their initial conditions and to any small perturbation. In particular, small variations in the initial conditions of a chaotic system lead to an exponential divergence of its evolution from the unperturbed trajectory.

Chaos synchronization is a peculiar behavior of chaotic systems, discovered by L. Pecora and T. Carroll, in the mid-80s: a chaotic system, called *master*, can, under proper conditions, force another similar system, called *slave*, to follow its same evolution [1]. This phenomenon is employed in chaotic communication systems to achieve the goal of providing an high level of privacy between the transmitter and the receiver. In particular, at the transmitter of a steganographic system, a nonlinear device, *e.g.*, a semiconductor laser, can

¹cryptography: from the Greek words “*kryptós*” (hidden), and “*gráphein*” (writing), means to hide the meaning of the message.

²steganography: from the Greek words “*stéganos*” (secret), and “*gráphein*” (writing), means to hide the existence of the message.

³In the usual meaning, the word *chaos* denotes an absence of order, and it seems a nonsense to compare it with the concept of *determinism*, which means order. The explanation comes from the mathematical definition of chaos, *i.e.*, that of a nonlinear deterministic system, from which an apparent disorder can appear in some particular circumstances.

be routed into a chaotic state through a proper feedback configuration, and a message can then be embedded onto the generated chaotic carrier, obtaining the steganography of the message. At the receiver, the synchronization of the slave with the master, together with a difference operation and an opportune filtering, permits the recovery of the message.

The security resides in the fact that an eavesdropper cannot easily identify a chaotic signal, because it is noise-like, and cannot reproduce the chaotic carrier exactly, which is needed for the message recovery process. Furthermore, the synchronization quality depends on the availability of “twin” master-slave systems⁴, having very close parameters, and also on the influence of the transmission impairments and noise.

In recent years, optical chaotic systems have been heavily studied by considering the propagation on an optical fiber, as explained in some of the several works developed over the years [2–7]. In particular, a fully functional chaotic link over optical fibers has been realized in Athens, Greece [4]. The aim of this Thesis is to extend the study of an optical chaotic system to a free-space link. Wireless infrared links are becoming more attractive over traditional radio ones, for several reasons: infrared communications have very large, free and unlicensed available bandwidth, and the wide availability of low cost hardware devices makes such systems preferable in terms of final product prices. Moreover, infrared radiation is already physically confined in closed environments, due to the presence of walls. Furthermore, optical systems typically require higher power consumptions than system operating in the microwave band, posing problems for mobile devices with low power availability. Also, particular attention must be done for the eye safety.⁵

In this Thesis, an optical chaotic steganographic free space communication system is studied numerically. The chaotic optical carrier generation, at the transmitter, is obtained by using a semiconductor laser with delayed optoelectronic feedback. The message, assumed to be PPM encoded⁶, is embedded onto the generated chaotic carrier through superposition. At the receiver, the message is recovered by using a semiconductor laser similar to that used at the transmitter, but operated in an open loop configuration. The system performance is evaluated in terms of the synchronization error and of the Q factor measured at two different points of the system. The performance analysis is aimed to verify both the effective masking of the message at the transmitter (an eavesdropper should not be able to recover the hidden message) and the quality of the message recovery at the receiver, after the synchronization. Furthermore, a detailed numerical analysis is done first in a BTB configuration, and then by considering the free-space propagation in a closed indoor environment.

⁴For instance, for a couple of semiconductor lasers, in order to have very similar parameters, they must be built in the same wafer.

⁵Sufficiently powerful visible to near infrared laser radiation (400 nm to 1400 nm) penetrates the eyeball and may cause heating of the retina, whereas exposure to laser radiation with wavelengths less than 400 nm and greater than 1400 nm are largely absorbed by the cornea and lens, leading to the development of cataracts or burn injuries [8]. However, in this Thesis, the lasers operate at a wavelength of 1550 nm with a maximum average optical power of 0.1 mW. A laser of this type is classified as a *Class 1* laser, *i.e.*, its emitted radiation is not dangerous under reasonable conditions of use [9].

⁶PPM is employed in several standards for optical infrared communications, *e.g.*, in IEEE 802.11 and Irda standards.

1.1 Overview of the Thesis

The Thesis is organized as follows.

Chapter 2 Here it will be briefly explained how a semiconductor laser works. The conditions needed to achieve laser emission will be briefly reviewed in the case of a Fabry-Perot cavity, and the rate equations describing the dynamics of the laser will be derived.

Chapter 3 In this chapter, the concept of chaos will be introduced, by defining the main peculiarities of generic chaotic systems.

Then, the generation and the synchronization of optical chaos through semiconductor lasers will be treated, by introducing a numerical model to simulate and analyze the chaotic behaviors of such systems.

Chapter 4 This chapter provides an overview of an optical chaotic communication system operating in free-space. The building blocks and their interconnections will be explained in detail, together with some design choices which will be used in the numerical analysis of the system.

Furthermore, the estimation of the system performance will be defined.

Chapter 5 The main results of numerical simulations are presented and commented, together with possible solutions to prevent some noticed problems and limitations.

Chapter 2

Semiconductor Lasers

Truth is much too complicated to allow anything but approximations.

John von Neumann (1903 – 1957)

The simplest setup of a semiconductor laser is constituted by a pn -junction diode combined with an optical resonant cavity filled by an active medium. When the junction is forward polarized, the injected carriers recombine, generating photons through stimulated emission [10]. If the carrier density exceeds a certain threshold value, the generated light is amplified, yielding the laser emission [10].

In this chapter, by following the treatment explained in [11] and [12], the conditions needed to achieve laser emission will be briefly reviewed in the case of a Fabry-Perot cavity, and the rate equations describing the dynamics of the laser will be derived.

2.1 Conditions for Laser Oscillation

The model of a Fabry-Perot resonator shown in Fig. 2.1 is used to approximate the physics of the active region of a semiconductor laser [11, 12]. Basically, it is constituted by a gain medium, delimited by two partially reflecting mirrors; usually the mirrors are built by appropriately cleaving the back and front facets of the laser diode.

The cavity length is l , and the amplitude reflectivities of the front and back facets are r_1 and r_2 respectively. The active medium inside the cavity has a power gain per unit length g (Np m^{-1}), and a (Np m^{-1}) is the total power loss per unit length due to absorption and scattering.

The phase constant in the medium, for a wave with frequency ν , is

$$\beta = n \frac{2\pi\nu}{c} = n \frac{\omega}{c}, \quad (2.1)$$

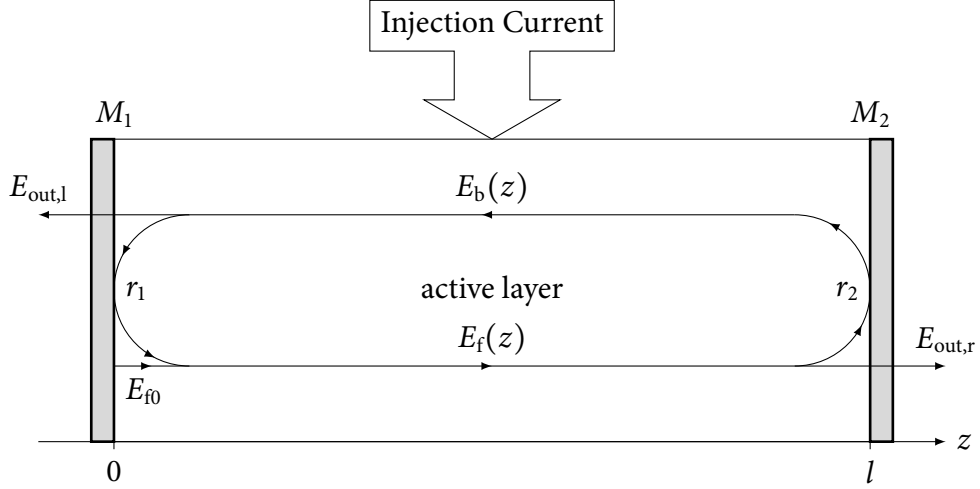


Figure 2.1: Model of a Fabry-Perot resonant cavity.

where c is the speed of light in vacuum, ω is the angular frequency, and n is the refractive index of the medium.

Due to the presence of gain and loss, a wave propagates with a complex propagation constant given by [11, 12]:

$$k = j\beta - \frac{g - a}{2}, \quad (2.2)$$

with $j = \sqrt{-1}$ being the imaginary unit.

If a photon enters the cavity from the left mirror M_1 , a forward wave E_f propagates toward the right mirror M_2 , where it is partially transmitted out ($E_{out,r}$), and partially bounced back (E_b) up to M_1 , where, again, it is partially transmitted out ($E_{out,l}$), and partially bounced back, and the entire process can restart.

A stable oscillation is reached if two conditions are satisfied [11]:

- the gain balances the losses introduced by the medium and the mirrors;
- the backward wave couples back in phase with the forward one.

Moreover, by using Steinmetz representation, a generic electric field $e(z, t)$, at an angular frequency $\omega = 2\pi\nu$, can be described by [13]:

$$e(z, t) = \text{Re} \{ E(z) e^{j\omega t} \}, \quad (2.3)$$

where $E(z)$ is the complex amplitude of the field.

The forward propagating wave E_f , assumed to be a plane wave, starts to propagate inside the cavity at $z = 0$ with a complex amplitude $E_{f,0}^i$ and angular frequency ω .¹ The evolution of the forward propagating field can be, therefore, described by:

$$E_f^i(z) = E_{f,0}^i e^{-kz}. \quad (2.4)$$

At $z = l$, the wave is partially reflected by the right facet M_2 , and the backward propagating wave is then described by:

$$E_b^i(z) = E_{b,0}^i e^{k(l-z)}, \quad (2.5)$$

¹The superscript i is used to referring to the i -th round trip.

with the initial amplitude $E_{b,0}^i$ given by the boundary condition at the right mirror M_2 :

$$E_b^i(l) = r_2 E_f^i(l). \quad (2.6)$$

By combining Eqs. (2.4) to (2.6), at $z = l$, $E_{b,0}^i$ can be expressed in terms of $E_{f,0}^i$:

$$E_{b,0}^i = r_2 E_{f,0}^i e^{-kl}. \quad (2.7)$$

The amplitude of the wave transmitted out, at $z = l$, is given by:

$$E_{\text{out},r}^i = (1 - r_2) E_f^i(l). \quad (2.8)$$

Similar considerations hold at the left mirror M_1 . In particular, at $z = 0$, a reflection of the backward propagating wave takes place, under the boundary condition

$$E_f^{i+1}(0) = r_1 E_b^i(0), \quad (2.9)$$

and the amplitude of the forward propagating wave, for the next round trip $i + 1$, easily becomes:

$$E_{f,0}^{i+1} = r_1 r_2 E_{f,0}^i e^{-2kl}. \quad (2.10)$$

The amplitude of the wave transmitted out, at M_1 , is given by:

$$E_{\text{out},l}^i = (1 - r_1) E_b^i(0). \quad (2.11)$$

The complex round trip gain G_{rt} can be defined as the ratio between the amplitude of the forward propagating waves for two consecutive round trips, *i.e.*, between $E_{f,0}^{i+1}$ and $E_{f,0}^i$:

$$\begin{aligned} G_{\text{rt}} &= \frac{E_{f,0}^{i+1}}{E_{f,0}^i} = r_1 r_2 e^{-2kl} \\ &= r_1 r_2 e^{-2j\beta l + (g-a)l}, \end{aligned} \quad (2.12)$$

where the last equality is achieved by using the Eq. (2.2). A stable laser output is attained if

$$G_{\text{rt}} = 1, \quad (2.13)$$

which can be rewritten as:

$$r_1 r_2 e^{-2j\beta l + (g-a)l} = 1. \quad (2.14)$$

Eq. (2.13) leads to two conditions: one for the modulus and one for the phase of G_{rt} . In particular, by taking the modulus of Eq. (2.14), the condition

$$r_1 r_2 e^{(g-a)l} = 1 \quad (2.15)$$

must be satisfied.

The value of the power gain g for which Eq. (2.15) is satisfied is indicated with g_{th} , as follows:

$$g_{\text{th}} = a + \frac{1}{l} \ln \frac{1}{r_1 r_2}. \quad (2.16)$$

The value g_{th} defines the threshold value of the medium gain necessary to have laser oscillation. This condition is reached by opportunely controlling the injection current.

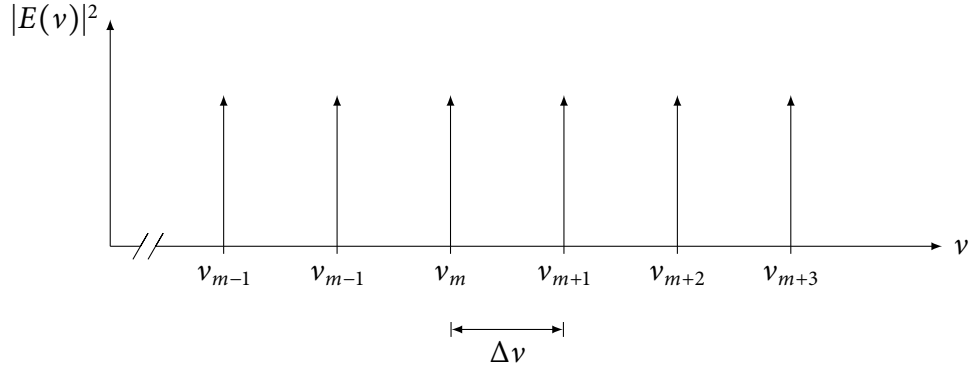


Figure 2.2: Possible frequencies of oscillation for longitudinal modes in a Fabry-Perot cavity.

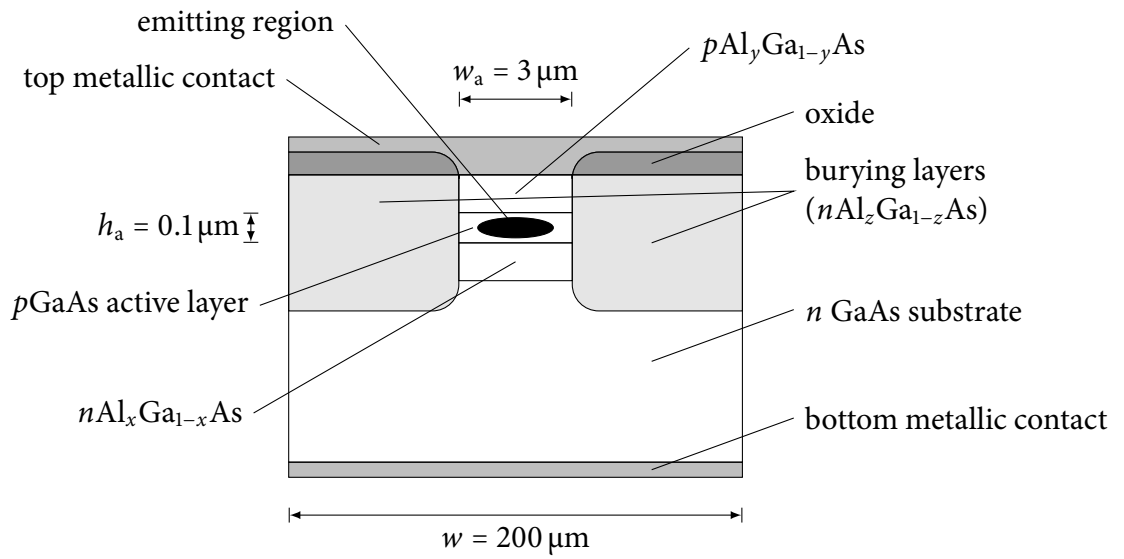


Figure 2.3: Front view of a buried double heterostructure edge emitting semiconductor laser with a single active region [10].

The phase of Eq. (2.14) yields:

$$e^{-2j\beta l} = 0, \quad (2.17)$$

which is verified for

$$\beta l = m\pi, \quad \forall m \in \mathbb{Z} \quad (2.18)$$

Eq. (2.18), by replacing β with Eq. (2.1), becomes:

$$\nu_m = m \frac{c}{2nl}, \quad \forall m \in \mathbb{Z}. \quad (2.19)$$

The ν_m values represent the only possible values of the oscillation frequencies, sketched in Fig. 2.2. Each ν_m corresponds to a “so-called” longitudinal mode of the cavity [11].

2.1.1 Effective Refractive Index

Most modern semiconductor lasers adopt particular structures in order to keep the injection current low and to control the distribution of the optical field [10]. A schematic

illustration of the front section of a buried double heterostructure semiconductor laser [10] is shown in Fig. 2.3. The burying layers, and the layers on the top and bottom of the active region, have a lower refractive index than that of the active region, hence a built-in guiding structure is present. For this reason, these type of lasers are also called “index-guided” lasers. Moreover, these four layers, surrounding the active region, form a double heterostructure junction, which have high efficiency. The particular structure profile allows the oscillation of a single longitudinal mode [12].

Furthermore, the oxide insulating layers force the injection current to flow only through a small region, so that the total required current is reduced [10, 14].

The structure of a real laser is, indeed, more complicated than that of a single isolated Fabry-Perot cavity, and, consequently, the effects of the particular structure design have to be considered in the preceding Fabry-Perot model.

The effective refractive index n_e , which can be calculated from the refractive indexes of the laser structure by using methods developed in the field of dielectric waveguides engineering, *e.g.*, with the Marcatili’s method [15], is used to account for the guiding properties of the structure. Just as an example, for the buried double heterostructure of Fig. 2.3, the effective refractive index can be approximated by [16]:

$$n_e = \sqrt{\Gamma n_a^2 + (1 - \Gamma) n_c^2}, \quad (2.20)$$

where n_a is the refractive index of the active region and n_c is that of the surrounding cladding layers (assumed to be equal for all layers). The confinement factor Γ represents the fraction of the power confined in the active region [14, 17, 18].

Consequently, the threshold gain g_{th} from Eq. (2.16) should be expressed by taking into account for Γ :

$$\Gamma g_{th} = a + \frac{1}{l} \ln \frac{1}{r_1 r_2}. \quad (2.21)$$

For the sake of clarity, in the following, the confinement factor will be considered as unity.

By substituting the refractive index n with the effective refractive index n_e , the phase constant in Eq. (2.1) becomes:

$$\beta = n_e \frac{\omega}{c} = n_e \frac{2\pi\nu}{c}, \quad (2.22)$$

and the frequencies of oscillation ν_m , given by Eq. (2.19), are modified into:

$$\nu_m = m \frac{c}{2n_e l}. \quad (2.23)$$

In order to account for the dispersion of the material, which is induced by the dependence of the refractive index on the frequency ν , from the definition of the group velocity [13]:

$$\nu_g = \left(\frac{\partial \beta}{\partial \omega} \right)^{-1}, \quad (2.24)$$

the effective group refractive index n_g is defined as:

$$n_g = \frac{c}{\nu_g} = c \frac{\partial \beta}{\partial \omega} = \frac{\partial n_e \nu}{\partial \nu} = n_e + \nu \frac{\partial n_e}{\partial \nu}. \quad (2.25)$$

Therefore, the round trip time τ_{rt} is defined as the time necessary to do a round trip in the cavity and is given by:

$$\tau_{rt} = \frac{2l}{\nu_g} = \frac{2ln_g}{c}. \quad (2.26)$$

2.1.2 Free Spectral Range

From Eq. (2.23), the product of the oscillation frequency and the effective refractive index νn_e is a constant:

$$\nu n_e = m \frac{c}{2l}. \quad (2.27)$$

An implicit differentiation, with respect to m , yields:

$$\begin{aligned} \frac{\partial \nu n_e}{\partial m} &= n_e \frac{\partial \nu}{\partial m} + \nu \frac{\partial n_e}{\partial m} \\ &= n_e \frac{\partial \nu}{\partial m} + \nu \frac{\partial n_e}{\partial \nu} \frac{\partial \nu}{\partial m} \\ &= \frac{\partial \nu}{\partial m} \left(n_e + \nu \frac{\partial n_e}{\partial \nu} \right) \\ &= \frac{\partial \nu}{\partial m} n_g = \frac{c}{2l}. \end{aligned} \quad (2.28)$$

Eq. (2.28) permits to define the spacing between two adjacent emission frequencies, ν_{m+1} and ν_m , also known in the literature as the free spectral range (FSR):

$$\Delta \nu = \nu_{m+1} - \nu_m = \frac{\partial \nu}{\partial m} = \frac{c}{2ln_g} = \frac{1}{\tau_{rt}}. \quad (2.29)$$

2.1.3 Photon Density

The photon density S inside the cavity is related to the square of the modulus of the electric field E by the following relation [12]:

$$S(t) = \frac{1}{h\nu} \frac{\epsilon_0 \bar{n} n_g}{2V} |E|^2, \quad (2.30)$$

where $h = 6.626 \times 10^{-34}$ J s is the Planck's constant, $h\nu$ is the energy of a photon, $\epsilon_0 = 8.854 \times 10^{-12}$ F m⁻¹ is the electric permittivity of vacuum, \bar{n} is the modal refractive index and V is the volume.

For the sake of simplicity, in the following, the photon density S will be considered normalized to the square of the modulus of the electric field E :

$$S = |E|^2. \quad (2.31)$$

Furthermore, in absence of gain, *i.e.*, if $g = 0$, the photon density $S(t) = |E(t)|^2$ inside the cavity decays with a rate given by the following differential equation [10]:

$$\frac{dS(t)}{dt} = -\frac{S(t)}{\tau_{ph}} = -\gamma_c S(t), \quad (2.32)$$

where τ_{ph} is the photon lifetime and $\gamma_c = 1/\tau_{ph}$ is the photon decay rate (also known in the literature as the cavity decay rate).

The general solution of Eq. (2.32) is:

$$S(t) = S(0) e^{-t/\tau_{ph}}, \quad (2.33)$$

which, after a round trip time τ_{rt} , gives:

$$S(\tau_{rt}) = S(0) e^{-\tau_{rt}/\tau_{ph}} . \quad (2.34)$$

The square of the modulus of the round trip gain G_{rt} , of Eq. (2.12), is, for $g = 0$:

$$|G_{rt}|^2 = |r_1 r_2|^2 e^{-2al} , \quad (2.35)$$

and it can be expressed also in terms of the photon density S as:

$$|G_{rt}|^2 = \frac{S(\tau_{rt})}{S(0)} = e^{-\tau_{rt}/\tau_{ph}} . \quad (2.36)$$

By equating Eq. (2.34) with Eq. (2.36), and by using the definition of the round trip time from Eq. (2.26), the photon decay rate becomes:

$$\frac{1}{\tau_{ph}} = \nu_g \left(a + \frac{1}{l} \ln \frac{1}{r_1 r_2} \right) = \nu_g g_{th} . \quad (2.37)$$

2.1.4 Carrier Induced Frequency Shift

The power gain g of the active medium depends on the carrier density N [10–12]. The threshold carrier density N_{th} is defined as the carrier density required to approach the threshold gain g_{th} of Eq. (2.16):

$$g(N_{th}) = g_{th} . \quad (2.38)$$

The effective refractive index n_e depends on the frequency ν and also on the carrier density N [11], and it can be rewritten in terms of its first order Taylor expansion around the threshold point (ν_{th}, N_{th}) :

$$n_e = n_{e,th} + \left. \frac{\partial n_e}{\partial \nu} \right|_{\nu=\nu_{th}} (\nu - \nu_{th}) + \left. \frac{\partial n_e}{\partial N} \right|_{N=N_{th}} (N - N_{th}) . \quad (2.39)$$

For a given mode m , from Eq. (2.23), the frequencies ν and ν_{th} can be expressed as:

$$\nu = m \frac{c}{2n_e l} \quad (2.40a)$$

$$\nu_{th} = m \frac{c}{2n_{e,th} l} . \quad (2.40b)$$

A change of the refractive index n_e , in Eq. (2.40a), implies a change of the frequency ν . The induced frequency shift is defined as [11]:

$$\nu - \nu_{th} = - \frac{\nu_{th}}{n_{g,th}} \left. \frac{\partial n_e}{\partial N} \right|_{N=N_{th}} (N - N_{th}) . \quad (2.41)$$

Eq. (2.41) defines the shift of the oscillation frequency caused by a change in the carrier density. This means that the power spectrum of the longitudinal modes is not constituted only by discrete components, as shown in Fig. 2.2. Instead, each oscillation mode covers

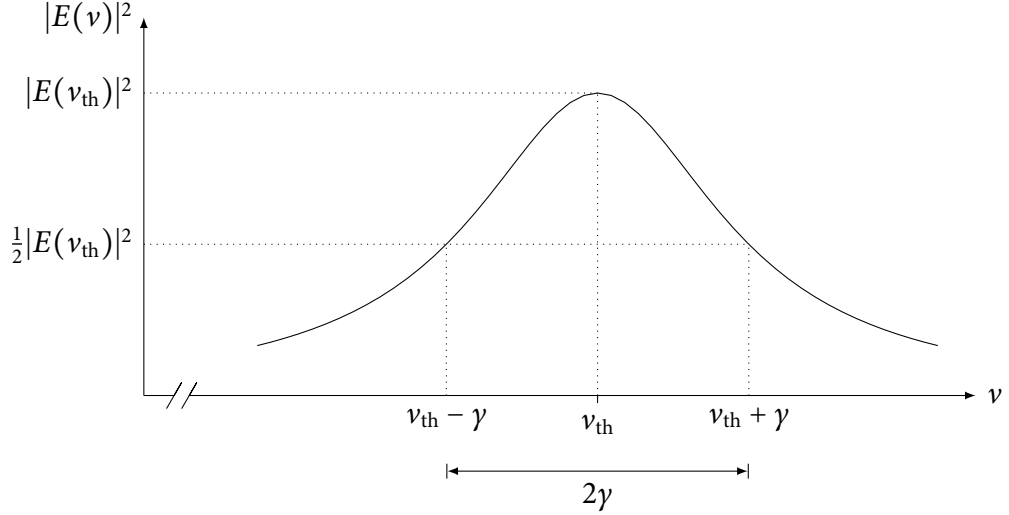


Figure 2.4: Linewidth broadening in a semiconductor laser due to changes in carrier density.

a finite continuous band of frequencies. This effect is called linewidth broadening. Furthermore, it can be shown that the shape of these broadened lines, near their resonant frequencies ν_{th} , is approximatively of Lorentzian form [10]:

$$|E(\nu)|^2 \approx |E(\nu_{th})|^2 \frac{\gamma^2}{(\nu - \nu_{th})^2 + \gamma^2}, \quad (2.42)$$

where, as shown in Fig. 2.4, γ is the half-width at half-maximum (HWHM).

Similar considerations can be also applied to the phase constant β . Eq. (2.22) can be rewritten in terms of its first order Taylor expansion around the threshold point (ω_{th}, N_{th}) :

$$\begin{aligned} \beta &= \beta_{th} + \left. \frac{\partial \beta}{\partial \omega} \right|_{\omega=\omega_{th}} (\omega - \omega_{th}) + \left. \frac{\partial \beta}{\partial N} \right|_{N=N_{th}} (N - N_{th}) \\ &= \frac{\omega_{th}}{c} \left(n_{e,th} + \frac{n_{g,th}}{\omega_{th}} (\omega - \omega_{th}) + \left. \frac{\partial n_e}{\partial N} \right|_{N=N_{th}} (N - N_{th}) \right), \end{aligned} \quad (2.43)$$

where both Eq. (2.25) and the following relation,

$$\beta_{th} = \beta(\omega_{th}, N_{th}) = \frac{\omega_{th} n_{e,th}}{c}, \quad (2.44)$$

have been used.

2.2 Derivation of the Rate Equations

2.2.1 Gain at Laser Oscillation

In the expression of the round trip gain G_{rt} of Eq. (2.12), the term $-2j\beta l$ can be rewritten by using the expansion of β introduced in Eq. (2.43), yielding:

$$\begin{aligned} -2j\beta l &= -2jl \frac{\omega_{th}}{c} \left(n_{e,th} + \frac{n_{g,th}}{\omega_{th}} (\omega - \omega_{th}) + \left. \frac{\partial n_e}{\partial N} \right|_{N=N_{th}} (N - N_{th}) \right) \\ &= -j2m\pi - j\tau_{rt}(\omega - \omega_{th}) - j2l \frac{\omega_{th}}{c} \left. \frac{\partial n_e}{\partial N} \right|_{N=N_{th}} (N - N_{th}). \end{aligned} \quad (2.45)$$

The first term $-j2m\pi$ is attained from Eq. (2.44), whereas the second term $-j\tau_{rt}(\omega - \omega_{th})$ is derived by using the relations in Eqs. (2.25) and (2.26).

The round trip gain G_{rt} is, actually, a function of the frequency, and can be written as a product of a frequency independent function $G_{rt}^{(1)}$, and of a function $G_{rt}^{(2)}(\omega)$ directly dependent on the frequency:

$$G_{rt}(\omega) = G_{rt}^{(1)} G_{rt}^{(2)}(\omega). \quad (2.46)$$

By considering the Eqs. (2.12) and (2.45), $G_{rt}^{(1)}$ and $G_{rt}^{(2)}(\omega)$ can be expressed by:

$$G_{rt}^{(1)} = r_1 r_2 e^{(g-a)l + j\varphi} \quad (2.47a)$$

$$G_{rt}^{(2)}(\omega) = e^{-j\tau_{rt}(\omega - \omega_{th})}, \quad (2.47b)$$

where the phase term φ is given by:

$$\varphi = -2l \frac{\omega_{th}}{c} \left. \frac{\partial n_e}{\partial N} \right|_{N=N_{th}} (N - N_{th}). \quad (2.48)$$

The term $e^{-j2m\pi} = 1$, $\forall m \in \mathbb{Z}$ has been eliminated.

2.2.2 Rate Equation for the Electric Field

In Eq. (2.4), the initial complex amplitude $E_{f,0}$ was assumed to be constant. By relaxing this condition, and assuming $E_{f,0}$ to be slowly varying, *i.e.*, having the form:

$$E_{f,0}(t) = \tilde{E}_{f,0}(t) e^{j\omega_{th}t}, \quad (2.49)$$

where $\tilde{E}_{f,0}(t)$ satisfies the slowly varying envelope approximation (SVEA)², it can be shown that the total intra-cavity electric field $E(t)$ is given by [12]:

$$E(t) = G_{rt}^{(1)} E(t - \tau_{rt}). \quad (2.51)$$

² The SVEA is a common approximation based on the assumption that the envelope of a traveling wave pulse varies slowly in time or space compared to a period or wavelength.

This requires the spectrum of the signal to be narrow band respect to the carrier frequency ω_0 , and for a signal $A(t) e^{j\varphi(t)}$ the requirements are [13]:

$$\left| \frac{dA(t)}{dt} \right| \ll \omega_0 |A(t)|, \quad (2.50a)$$

$$\left| \frac{d\varphi(t)}{dt} \right| \ll \omega_0 |\varphi(t)|. \quad (2.50b)$$

By replacing $E(t - \tau_{rt})$ with its first order Taylor expansion,

$$E(t - \tau_{rt}) = E(t) - \tau_{rt} \frac{dE(t)}{dt}, \quad (2.52)$$

into Eq. (2.51), $E(t)$ can be expressed by:

$$E(t) = G_{rt}^{(1)} \left(E(t) - \tau_{rt} \frac{dE(t)}{dt} \right), \quad (2.53)$$

which can be written in following form:

$$\frac{dE(t)}{dt} = \frac{1}{\tau_{rt}} \left(1 - \frac{1}{G_{rt}^{(1)}} \right) E(t). \quad (2.54)$$

For laser operation, the round trip gain G_{rt} should be close to unity, and so $G_{rt}^{(1)}$ should do. By using the common approximation of an exponential function:

$$e^x \approx 1 + x, \quad \text{for } x \approx 0, \quad (2.55)$$

the reciprocal of Eq. (2.47a) is:

$$\begin{aligned} \frac{1}{G_{rt}^{(1)}} &= (r_1 r_2 e^{(g-a)l + j\varphi})^{-1} = e^{\ln \frac{1}{r_1 r_2} - gl + al - j\varphi} \\ &\approx 1 + \ln \frac{1}{r_1 r_2} - gl + al - j\varphi. \end{aligned} \quad (2.56)$$

By inserting Eq. (2.56) into Eq. (2.54), the electric field evolution is given by the following differential equation:

$$\frac{dE(t)}{dt} = \frac{1}{\tau_{rt}} \left(-\ln \frac{1}{r_1 r_2} + gl - al + j\varphi \right) E(t). \quad (2.57)$$

The term φ/τ_{rt} can be rewritten as $\omega - \omega_{th}$ by using Eqs. (2.26) and (2.41), whereas, by combining the definition of the photon lifetime τ_{ph} from Eq. (2.37), and the definition of the round trip time τ_{rt} from Eq. (2.26), the term

$$\frac{1}{\tau_{rt}} \left(-\ln \frac{1}{r_1 r_2} + gl - al \right) \quad (2.58)$$

can be rewritten as:

$$\frac{1}{2} \left(gv_g - \frac{1}{\tau_{ph}} \right). \quad (2.59)$$

Therefore, the rate equation of the cavity electric field finally becomes:

$$\frac{dE(t)}{dt} = \left[j(\omega - \omega_{th}) + \frac{1}{2} \left(gv_g - \frac{1}{\tau_{ph}} \right) \right] E(t). \quad (2.60)$$

2.2.3 The Linewidth Enhancement Factor

It can be demonstrated that the dependence of the refractive index on the carrier density causes a broadening in the emission spectrum, as already mentioned. This effect can be quantified by considering the linewidth enhancement factor [19]:

$$\alpha = -2 \frac{\omega}{c} \frac{\partial n_e / \partial N}{\partial g / \partial N}. \quad (2.61)$$

By using Eq. (2.61) into Eq. (2.41), for the angular frequency $\omega = 2\pi\nu$, a new relation for the angular frequency shift can be obtained:

$$\begin{aligned} \omega - \omega_{\text{th}} &= -\frac{\omega_{\text{th}}}{n_{\text{g,th}}} \left. \frac{\partial n_e}{\partial N} \right|_{N=N_{\text{th}}} (N - N_{\text{th}}) \\ &= \frac{1}{2} \alpha \nu_{\text{g}} \left. \frac{\partial g}{\partial N} \right|_{N=N_{\text{th}}} (N - N_{\text{th}}). \end{aligned} \quad (2.62)$$

Moreover, the rate equation for the electric field, given in Eq. (2.60), can be rewritten as:

$$\frac{dE(t)}{dt} = \frac{1}{2} \left[j \alpha \nu_{\text{g}} \left. \frac{\partial g}{\partial N} \right|_{N=N_{\text{th}}} (N - N_{\text{th}}) + g \nu_{\text{g}} - \frac{1}{\tau_{\text{ph}}} \right] E(t). \quad (2.63)$$

The power gain g near the threshold can be expanded as [11]:

$$g \approx g_{\text{th}} + \left. \frac{\partial g}{\partial N} \right|_{N=N_{\text{th}}} (N - N_{\text{th}}), \quad (2.64)$$

and by considering the following position, from Eq. (2.37):

$$\frac{1}{\tau_{\text{ph}}} = \nu_{\text{g}} g_{\text{th}}, \quad (2.65)$$

the rate equation is simplified to:

$$\begin{aligned} \frac{dE(t)}{dt} &= \frac{1}{2} \left[(1 + j \alpha) \nu_{\text{g}} \left. \frac{\partial g}{\partial N} \right|_{N=N_{\text{th}}} (N - N_{\text{th}}) \right] E(t) \\ &= \frac{1}{2} (1 + j \alpha) G_N (N - N_{\text{th}}) E(t), \end{aligned} \quad (2.66)$$

where G_N is the modal optical gain, defined as [12]:

$$G_N = \nu_{\text{g}} g_N = \nu_{\text{g}} \left. \frac{\partial g}{\partial N} \right|_{N=N_{\text{th}}}. \quad (2.67)$$

2.2.4 Rate Equation for the Photon Density

The rate equation for the photon density $S(t) = |E(t)|^2$ is easily derived by taking the derivative of $S(t) = E(t)E^*(t)$, which yields:

$$\frac{dS(t)}{dt} = \frac{dE(t)E^*(t)}{dt} = E^*(t) \frac{dE(t)}{dt} + E(t) \frac{dE^*(t)}{dt}, \quad (2.68)$$

which, by using Eq. (2.66), yields:

$$\frac{dS(t)}{dt} = G_N(N(t) - N_{th})S(t). \quad (2.69)$$

By reintroducing the confinement factor Γ and the photon decay rate γ_c , Eq. (2.69) can be rewritten as [12]:

$$\boxed{\frac{dS(t)}{dt} = -\gamma_c S(t) + \Gamma g S(t)}. \quad (2.70)$$

2.2.5 Rate Equation for the Carrier Density

The rate equation for the carrier density $N(t)$ is given by [11,12,14]:

$$\frac{dN(t)}{dt} = \frac{J(t)}{eh_a} - \frac{N(t)}{\tau_s} - G_N(N(t) - N_{tr})S(t), \quad (2.71)$$

where $J(t)$ is the injection current density, h_a is the thickness of active layer and $e = 1.602 \times 10^{-19}$ C is the electric charge constant.

The first term $J(t)/eh_a$ is the current pumping, whereas the second term $N(t)/\tau_s$ is the carrier recombination due to spontaneous emissions. The last term $G_N(N(t) - N_{tr})S(t)$ is the carrier recombination induced by the laser emission, with N_{tr} being the carrier density at the transparency. The carrier density at the transparency N_{tr} is related to the threshold gain g_{th} and to the threshold carrier density N_{th} by [12]:

$$g_{th} = g_N(N_{th} - N_{tr}). \quad (2.72)$$

By defining the spontaneous carrier decay rate:

$$\gamma_s = \frac{1}{\tau_s}, \quad (2.73)$$

Eq. (2.71) can be rewritten as:

$$\boxed{\frac{dN(t)}{dt} = \frac{J(t)}{eh_a} - \gamma_s N(t) - g S(t)}. \quad (2.74)$$

Chapter 3

Chaos in Semiconductor Lasers

Chaos is inherent in all compounded things.
Strive on with diligence.

Gautama Buddha (566 BCE – 486 BCE)

In this chapter, the concept of chaos will be introduced, by defining the main peculiarities of generic chaotic systems.

Then, the generation of optical chaos through semiconductor lasers will be explained, by introducing a numerical model to simulate and analyze the chaotic behaviors of such systems.

Finally, it will be explained how two chaotic systems can be synchronized.

3.1 What is Chaos?

Chaos is a phenomenon related to the occurrence of apparent randomness, aperiodic and irregular behavior, and unpredictability in completely deterministic systems. The main feature of a chaotic system is that small changes of initial conditions lead to exponential changes of trajectories, even when no external perturbations are present. This also implies that it is not possible to make any accurate long-term prediction about the behavior of the system.

A classical example of a dynamical continuous system exhibiting chaotic behavior is the Lorenz's attractor [20], introduced in 1963 by the meteorologist Edward Lorenz, who was working on the problem of weather forecast.

The system is described by the following differential equations:

$$\begin{aligned}\frac{dx(t)}{dt} &= \sigma(y - x) \\ \frac{dy(t)}{dt} &= x(\rho - z) - y \\ \frac{dz(t)}{dt} &= xy - \beta z,\end{aligned}\tag{3.1}$$

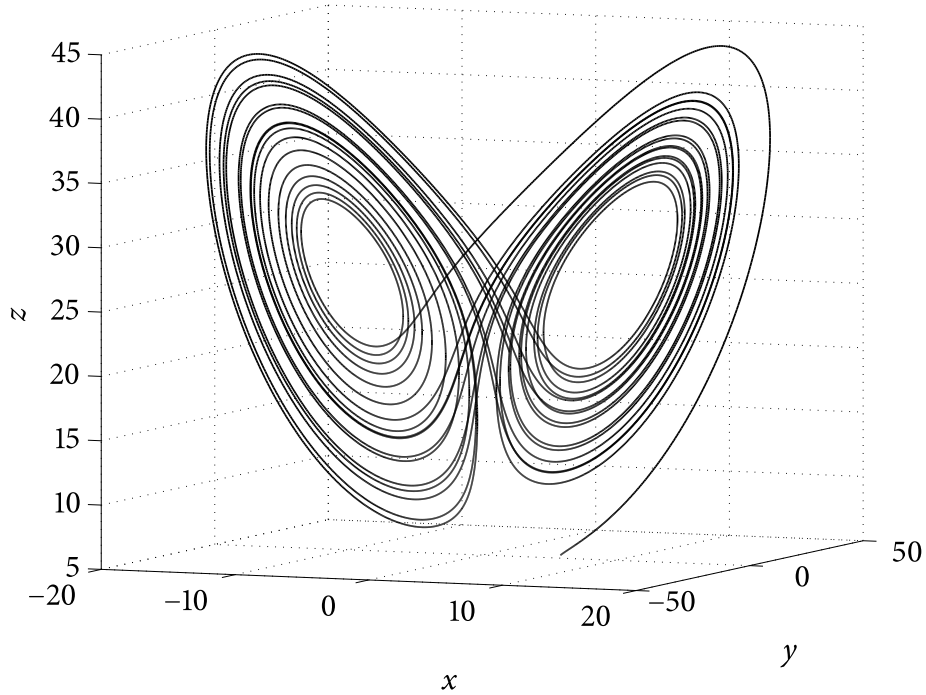


Figure 3.1: Time evolution in the phase space of the Lorenz's attractor (the “butterfly”) of Eq. (3.1) with the parameters given in Eq. (3.2) and initial condition $\mathbf{u}(0) = (5, 5, 5)$, where $\mathbf{u}(t) = (x(t), y(t), z(t))$.

with σ and ρ being the Prandtl and the Rayleigh numbers.

In Fig. 3.1, the system evolution in the phase space is shown, when the following parameters are considered:

$$\begin{aligned}\sigma &= 10 \\ \rho &= 28 \\ \beta &= \frac{8}{3}.\end{aligned}\tag{3.2}$$

The evolution is described by a complex and non repeating curve, a double spiral. The trajectory repeatedly leaves one spiral and enters the other. The sequence of the number of turns that the trajectory spends in one spiral and then in the other is not predictable.

Fig. 3.2 shows the time evolution of the x components of two realization of the Lorenz's attractor with initial conditions that differ of 0.1%. This clearly shows that a small change in initial conditions leads to a big change in the system trajectories evolution.

3.2 Chaos Synchronization

As already mentioned, chaotic systems have strong sensitivity to initial condition variations and to any perturbation. In the phase space, two identical isolated chaotic systems follow different and uncorrelated trajectories, because they start from different initial points, or because some perturbation alters their trajectories.

Chaos synchronization is a peculiar property of chaotic systems discovered by L. Pecora and T. Carroll, in mid-80s: two similar chaotic systems can synchronize, showing the

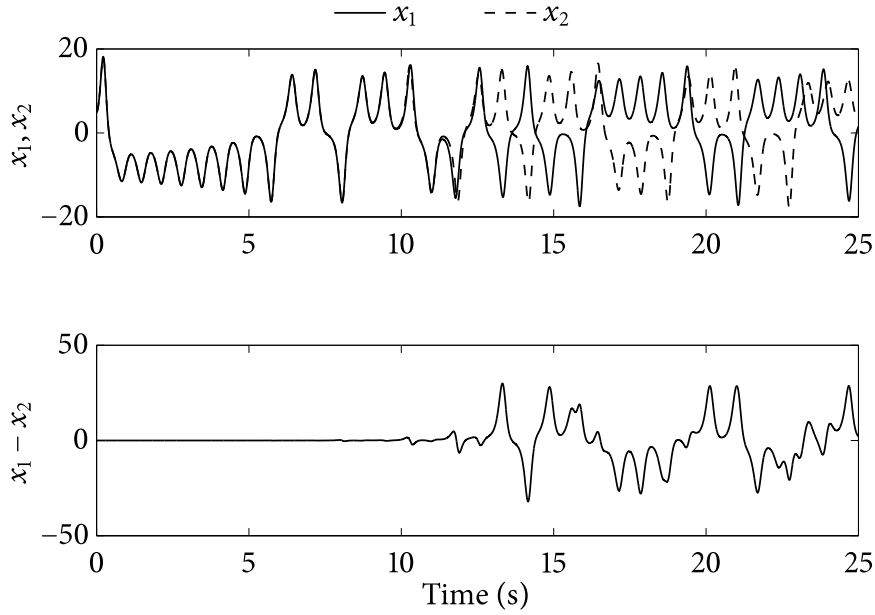


Figure 3.2: Time evolution of the x components of two realizations of the Lorenz's attractor of Eq. (3.1) with the parameters given in Eq. (3.2) and initial conditions $\mathbf{u}_1(0) = (5, 5, 5)$, $\mathbf{u}_2(0) = (5.005, 5, 5)$, where, for $i = 1, 2$, $\mathbf{u}_i(t) = (x_i(t), y_i(t), z_i(t))$.

same evolution, if the first, called master, forces, under proper conditions, the evolution of the second, called slave [1, 21].

The theory proposed in [1] has demonstrated the feasibility of chaos synchronization when a proper driving signal is used to couple the two systems. In particular, it can be shown that the difference signal between the outputs of two coupled chaotic systems has a stable fixed point in the origin of the phase space, *i.e.*, the difference signal is near zero as the time evolves.

There are several schemes to achieve synchronization of two chaotic systems. In the following, two schemes will be briefly examined: the complete replacement method and the active-passive method.

3.2.1 The Complete Replacement Method

The complete replacement method was the first scheme proposed in [1, 21] to obtain the synchronization of two isolated chaotic systems using a proper coupling signal.

Two n -dimensional chaotic systems can be described by their generic dynamical equations:

$$\frac{d\mathbf{u}_M}{dt} = \mathbf{F}_M(\mathbf{u}_M) \quad (3.3a)$$

$$\frac{d\mathbf{u}_S}{dt} = \mathbf{F}_S(\mathbf{u}_S), \quad (3.3b)$$

where the subscripts M and S refer to master and slave, respectively.

Each of the two systems can be decomposed into two subsystems \mathbf{v} and \mathbf{w} by separating

the variables $\mathbf{u}_i = (\mathbf{v}_i, \mathbf{w}_i)$, obtaining, for $i = M, S$:

$$\frac{d\mathbf{v}_i}{dt} = \mathbf{G}_i(\mathbf{v}_i, \mathbf{w}_i) \quad (3.4a)$$

$$\frac{d\mathbf{w}_i}{dt} = \mathbf{H}_i(\mathbf{v}_i, \mathbf{w}_i), \quad (3.4b)$$

where

$$\mathbf{v}_i = (u_{i,1}, \dots, u_{i,m}) \quad (3.5)$$

$$\mathbf{w}_i = (u_{i,m+1}, \dots, u_{i,n}) \quad (3.6)$$

$$\mathbf{G}_i = (F_{i,1}(\mathbf{u}_i), \dots, F_{i,m}(\mathbf{u}_i)) \quad (3.7)$$

$$\mathbf{H}_i = (F_{i,m+1}(\mathbf{u}_i), \dots, F_{i,n}(\mathbf{u}_i)). \quad (3.8)$$

The subsystem \mathbf{v}_M is used as the driving signal to couple the two chaotic systems and, at the same time, to replace the corresponding dynamical variables \mathbf{v}_S in the slave chaotic system. Synchronization is achieved when the remaining subsystems \mathbf{w}_M and \mathbf{w}_S are synchronized.

In terms of system equations, this method is mathematically described as:

$$\frac{d\mathbf{v}_M}{dt} = \mathbf{G}_M(\mathbf{v}_M, \mathbf{w}_M) \quad (3.9a)$$

$$\frac{d\mathbf{w}_M}{dt} = \mathbf{H}_M(\mathbf{v}_M, \mathbf{w}_M) \quad (3.9b)$$

$$\frac{d\mathbf{w}_S}{dt} = \mathbf{H}_S(\mathbf{v}_M, \mathbf{w}_S), \quad (3.9c)$$

where in Eq. (3.9c) the slave subsystem \mathbf{v}_S is completely replaced by the master subsystem \mathbf{v}_M .

When synchronization is obtained, the error (or difference signal)

$$\mathbf{e} = \mathbf{w}_M - \mathbf{w}_S \quad (3.10)$$

approaches zero. The condition

$$\mathbf{H}_S = \mathbf{H}_M \quad (3.11)$$

defines the fact that the two subsystems are identical, and it is required to attain a perfect synchronization.

The proper choice of the subsystem used as the driving signal is fundamental for chaos synchronization, and the driving subsystem must be fully extractable and separable from the master chaotic system.

3.2.2 The Active-Passive Method

The active-passive method [22] is a generalization of the complete replacement method, and it is more suitable in practical applications.

By considering the generic dynamical equations for master and slave of Eqs. 3.3, the driving signal $\mathbf{s}(t)$ can be defined as a function of the variables \mathbf{u}_M of the master system:

$$\mathbf{s}(t) = \mathbf{h}(\mathbf{u}_M). \quad (3.12)$$

For two chaotic systems that are physically coupled by a signal $\mathbf{s}(t)$, the equations that describe each system can be mathematically rewritten, by using an appropriate choice of F' , and by considering a common driving signal $\mathbf{D}(\mathbf{s}(t))$ for both systems, as:

$$\frac{d\mathbf{u}_M}{dt} = F'_M(\mathbf{u}_M, \mathbf{D}(\mathbf{s}(t))) \quad (3.13a)$$

$$\frac{d\mathbf{u}_S}{dt} = F'_S(\mathbf{u}_S, \mathbf{D}(\mathbf{s}(t))). \quad (3.13b)$$

If the error

$$\mathbf{e} = \mathbf{u}_M - \mathbf{u}_S \quad (3.14)$$

has a stable fixed point in the origin of the phase space, the two chaotic systems can synchronize. The existence of such a fixed point is guaranteed only if the average Lyapunov exponents¹ of the error \mathbf{e} are all negative, and only if the systems are identical, *i.e.*, if:

$$F'_S = F'_M. \quad (3.16)$$

Differently from the case of the complete replacement method, in the active-passive method the driving signal does not replace any dynamical variable of the slave system. Moreover, the variables of the slave system which correspond to those contained in the driving signal asymptotically approach the correspondent variables of the master system. When the two systems are synchronized, the remaining variables of the slave system also synchronize with those of the master system.

3.3 Chaotic Lasers

Semiconductor lasers, because of their intrinsic nonlinear nature, under proper conditions show chaotic behaviors, exhibiting fast, irregular and aperiodic pulsing of the optical emission. The generation of optical chaos is generally obtained by lasers subjected to feedback [12, 24, 25].

In the following, two approaches are presented. The first, called all-optical scheme, will be briefly introduced. The second, called optoelectronic scheme, will be investigated in details, through a proper numerical model.

Chaotic Lasers with Delayed All-Optical Feedback

A semiconductor laser with delayed all-optical feedback [24, 26, 27] is sketched in Fig. 3.3. The optical chaos is obtained by optical feedback from an external cavity, realized through a mirror M_{ext} . The reflected injection stimulates the nonlinear dynamics for the chaos generation. Furthermore, the dynamics of this scheme depends on both the amplitude and phase of the injected field.

¹The Lyapunov exponents are used to quantify the rate of exponential divergence from perturbed initial conditions. By defining $\delta(t)$ as the average deviation from the unperturbed trajectory at time t , then the Lyapunov exponents are defined as [23]:

$$\lambda_i = \lim_{t \rightarrow +\infty} \frac{1}{t} \ln |\delta_i(t)|. \quad (3.15)$$

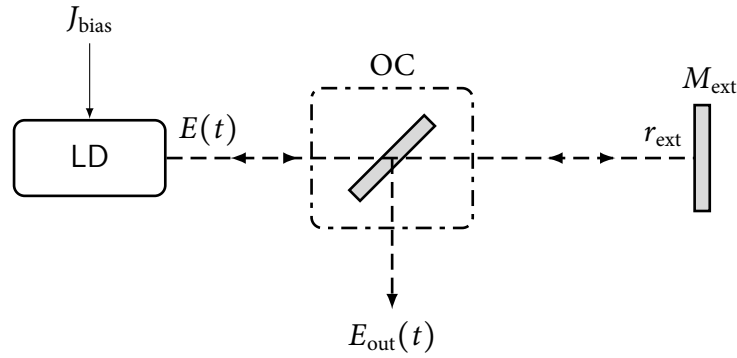


Figure 3.3: Schematic diagram of a semiconductor laser with delayed all-optical feedback (LD: semiconductor laser diode, OC: optical coupler).

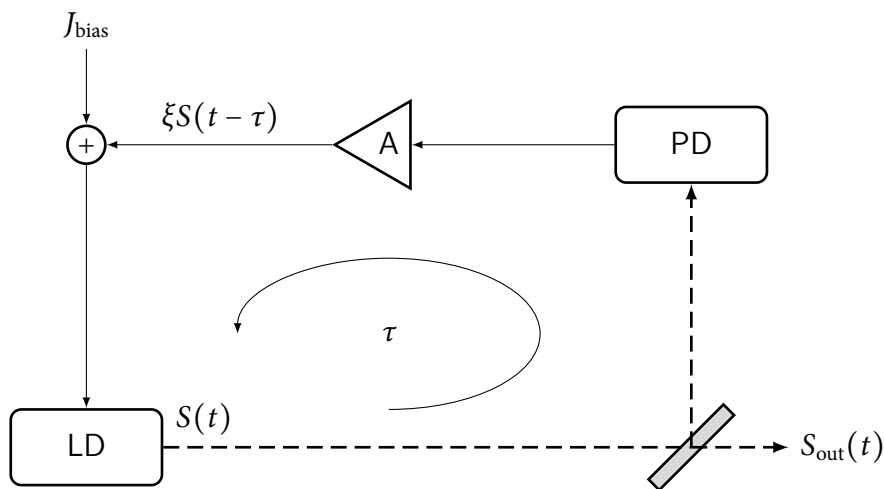


Figure 3.4: Schematic diagram of a semiconductor laser with delayed optoelectronic feedback (LD: semiconductor laser diode, PD: photodiode, A: amplifier, solid lines represent electrical links, whereas dashed lines are optical paths).

3.3.1 Chaotic Lasers with Delayed Optoelectronic Feedback

A semiconductor laser with delayed optoelectronic feedback [28–30] is schematically shown in Fig. 3.4. As it can be seen, a photodiode (PD), followed by an electric amplifier (A), is used to convert the optical output $S(t)$ of the laser into an electrical signal $\xi S(t - \tau)$ that is fed back to the laser by adding it to the injection current. This injection disturbs the “normal” laser bias, stimulating the generation of chaos.

The photodiode output depends solely on the intensity of the input light, so the feedback signal only contains information about the laser intensity, which is proportional to the photon density in the laser cavity. Contrary to systems with an external cavity optical feedback, the dynamics of this configuration does not include informations about the phase of the optical field.

The dynamical equations of the system, in terms of photon and carrier density, are

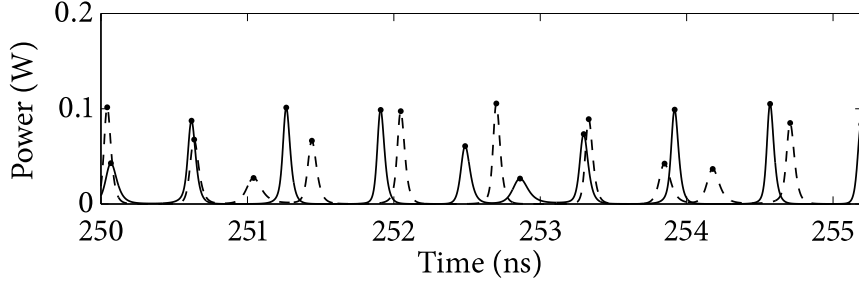


Figure 3.5: Time evolution of two realization of the output power of the same laser: the different evolutions are due only by internal noises.

derived by starting from Eqs. (2.70) and (2.74):

$$\frac{dS(t)}{dt} = -\gamma_c S(t) + \Gamma g S(t) + 2\sqrt{S_0 S(t)} F_S \quad (3.17a)$$

$$\frac{dN(t)}{dt} = \frac{J(t)}{eh_a} [1 + \xi y(t - \tau)] - \gamma_s N(t) - g S(t) \quad (3.17b)$$

$$y(t) = \int_{-\infty}^t \frac{f(t - \eta) S(\eta)}{S_0} d\eta, \quad (3.17c)$$

where ξ is the feedback strength, τ is the feedback delay time, and the term $f(t)$ is the normalized response function of the optoelectronic feedback loop. The function $f(t)$ contains the information about the finite bandwidth of both the photodetector and amplifier, and also accounts for any electric parasitic effect of the loop. The normalization term S_0 is the steady state value of the photon density for the free running laser. The term $2\sqrt{S_0 S(t)} F_S$ is a Langevin noise accounting for spontaneous emissions.²

Fig. 3.5 shows the time evolution of two realization of the output power of the same laser with same parameters: the different behaviors are due only to the Langevin internal noises, which, acting as very small perturbations, give totally different dynamics.

In the ideal case, the feedback loop has a flat and unlimited frequency response, so $f(t) = \delta(t)$ and $y(t) = S(t)/S_0$. In a realistic situation, however, $f(t) \neq \delta(t)$, and the dynamical system of Eqs. 3.17 is a system of coupled, stochastic and delayed integral-differential equations.

²A Langevin noise source $F(t)$ is a Gaussian stochastic processes satisfying the following conditions:

$$E[F(t)] = 0 \quad (3.18a)$$

$$E[F(t)F(s)] = 2D\delta(t - s), \quad (3.18b)$$

with D being the noise force, and $\delta(t)$ being the Dirac's delta function:

$$\delta(t) = \begin{cases} 1 & t = 0 \\ 0 & t \neq 0. \end{cases} \quad (3.19)$$

By defining the following normalized variables, as [30]:

$$\tilde{s}(t) = \frac{S(t) - S_0}{S_0} \quad (3.20a)$$

$$\tilde{n}(t) = \frac{N(t) - N_0}{N_0} \quad (3.20b)$$

$$\tilde{J}(t) = \frac{1}{\gamma_s N_0} \left[\frac{J(t)}{e h_a} - \gamma_s N_0 \right] \quad (3.20c)$$

$$\tilde{F}_S = \sqrt{S_0} F_S, \quad (3.20d)$$

where, analogously to S_0 , N_0 is the steady state carrier density, the coupled system of Eqs. 3.17 can be rewritten in the following normalized form:

$$\frac{d\tilde{s}(t)}{dt} = \frac{\gamma_c \gamma_n}{\tilde{J}(t) \gamma_s} \tilde{n}(t) [\tilde{s}(t) + 1] - \gamma_p \tilde{s}(t) [\tilde{s}(t) + 1] + 2\sqrt{S_0} [\tilde{s}(t) + 1] \tilde{F}_S \quad (3.21a)$$

$$\begin{aligned} \frac{d\tilde{n}(t)}{dt} = & \gamma_s \xi y(t - \tau) [1 + \tilde{J}(t)] - \gamma_s \tilde{n}(t) - \gamma_s \tilde{J}(t) \tilde{s}(t) \quad (3.21b) \\ & - \gamma_n \tilde{n}(t) [\tilde{s}(t) + 1] + \frac{\gamma_s \gamma_p}{\gamma_c} \tilde{J}(t) \tilde{s}(t) [\tilde{s}(t) + 1] \end{aligned}$$

$$y(t) = \int_{-\infty}^t f(t - \eta) [\tilde{s}(\eta) + 1] d\eta. \quad (3.21c)$$

The gain g is expanded near the free running condition (S_0, N_0) as [31]:

$$g \approx g_0 + g_N (N(t) - N_0) + g_S (S(t) - S_0), \quad (3.22)$$

where $g_0 = \gamma_c / \Gamma$ is the gain coefficient at free-running condition, $g_N = \partial g / \partial N$ is the differential gain parameter, and $g_S = \partial g / \partial S$ is the nonlinear gain parameter. It has been demonstrated that both g_N and g_S are constant and independent of the laser output power over a large range [28]. The differential carrier relaxation rate γ_n and the nonlinear carrier relaxation rate γ_p are defined as [29]:

$$\gamma_n = g_N S_0 \quad (3.23)$$

$$\gamma_p = -\Gamma g_S S_0. \quad (3.24)$$

The system of Eqs. 3.21 is composed by two equations in terms \tilde{s} and \tilde{n} , which are real scalar quantities. The system can exhibit chaotic behavior because, for a sufficiently long delay time τ , it can improve its intrinsic dimensionality.

The dynamics of the system is determined by the parameters $\gamma_c, \gamma_s, \gamma_n, \gamma_p$. The parameters that can be externally controlled are the bias current \tilde{J} , the feedback strength ξ and the feedback delay time τ . The feedback strength ξ is an important parameter, and it can be positive [28], $\xi > 0$, or negative [30], $\xi < 0$. The choice of the sign of ξ influences the system dynamics, but both options can lead to chaotic behavior. In this Thesis, a positive feedback strength will be assumed.

Finally, it can be observed that the response function $f(t)$ of the feedback loop has an important role in the dynamics of the system [28]. In particular, if $f(t)$ is a narrow bandpass filter, the chaotic dynamics can be completely eliminated. Such a filtering is used for example to stabilize the laser output. Because the aim of this Thesis is to exploit the chaotic behavior of a semiconductor laser, the function $f(t)$ should have a broad bandwidth [28]. More informations about the photodetection process can be found in Appendix B.

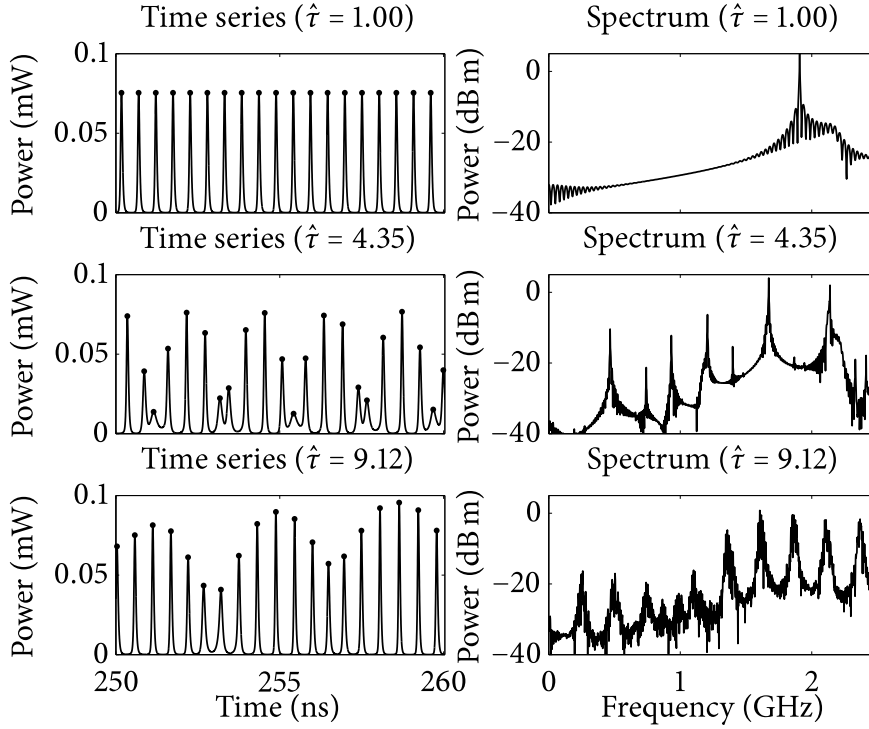


Figure 3.6: Optical output of a semiconductor laser with optoelectronic feedback for various normalized feedback delay times $\hat{\tau}$.

Route to Chaos

As already mentioned, the optoelectronic delayed feedback induces chaos generation in semiconductor lasers, and the “quality” of such chaotic behaviors depends on the time delay.

Fig. 3.6 shows the time series and the spectra of the output of an optoelectronic feedback laser for various normalized feedback delay time $\hat{\tau} = \tau f_r$, where f_r is the relaxation resonance frequency of the free running laser, defined as [12]:

$$f_r = \frac{1}{2\pi} \sqrt{\gamma_c \gamma_n + \gamma_s \gamma_p}. \quad (3.25)$$

For $\hat{\tau} = 1$ the pulses have constant peaks and spacing, and the spectrum has a clear line component at the frequency f_r' , which is close to the relaxation frequency f_r ³. For instance, this choice of feedback time can be used to stabilize the laser output and to narrow its bandwidth, which is the opposite of the aim of this Thesis.

By increasing the normalized time delay $\hat{\tau}$, the laser output starts to show chaotic characteristics. For example, as it can be viewed, for $\hat{\tau} = 4.35$ the pulses peaks and spacings are not constant anymore, nor they are periodic; also the spectrum is broader than before, with more line components. For $\hat{\tau} = 9.12$ the generated chaos is further improved, with an even broader spectrum.

³For stable pulsing states, the shift of the pulsing frequency f_r' from the relaxation frequency f_r depends mainly on the bias current [12].

3.3.2 Synchronization of Semiconductor Lasers with Optoelectronic Feedback

Chaos synchronization of semiconductor lasers cannot be realized by using the complete replacement method, described in Section 3.2.1, because the dynamical variables used for the driving signal are not separable from others, and not extractable from the laser. For instance, the carrier density is not directly accessible, so it cannot be used as the driving signal from the master to the slave laser. Moreover, a semiconductor laser is an integrated entity, and therefore all the dynamical variables are definitely not replaceable.

Fortunately, chaos synchronization of semiconductor lasers can be achieved by using the active-passive method, described in Section 3.2.2.

The driving signal $\mathbf{D}(\mathbf{s}(t))$ is defined as $\alpha\mathbf{D}(\mathbf{u}_M)$, where α is the coupling strength between master and slave, and the general system of Eqs. 3.13 can be rewritten as:

$$\frac{d\mathbf{u}_M}{dt} = \mathbf{F}'_M(\mathbf{u}_M, \alpha\mathbf{D}(\mathbf{u}_M)) \quad (3.26a)$$

$$\frac{d\mathbf{u}_S}{dt} = \mathbf{F}'_S(\mathbf{u}_S, \alpha\mathbf{D}(\mathbf{u}_M)), \quad (3.26b)$$

which can be simplified by defining the following functions:

$$\mathbf{f}_M(\mathbf{u}_M) = \mathbf{F}'_M(\mathbf{u}_M, \alpha\mathbf{D}(\mathbf{u}_M)) \quad (3.27a)$$

$$\mathbf{f}_S(\mathbf{u}_S) = \mathbf{F}'_S(\mathbf{u}_S, \alpha\mathbf{D}(\mathbf{u}_S)), \quad (3.27b)$$

to obtain:

$$\frac{d\mathbf{u}_M}{dt} = \mathbf{f}_M(\mathbf{u}_M) \quad (3.28a)$$

$$\frac{d\mathbf{u}_S}{dt} = \mathbf{f}_S(\mathbf{u}_S) + \alpha(\mathbf{D}(\mathbf{u}_M) - \mathbf{D}(\mathbf{u}_S)). \quad (3.28b)$$

In order to have perfect synchronization, all the parameters of master and slave lasers have to be matched, *i.e.*, it must be $\mathbf{F}_S = \mathbf{F}_M$ and $\mathbf{f}_S = \mathbf{f}_M$. Any mismatch between the equations describing the two systems can either deteriorate the quality of synchronization, or make the synchronization impossible.

Therefore, by assuming matched parameters, Eqs. 3.28 is rewritten as:

$$\frac{d\mathbf{u}_M}{dt} = \mathbf{f}(\mathbf{u}_M) \quad (3.29a)$$

$$\frac{d\mathbf{u}_S}{dt} = \mathbf{f}(\mathbf{u}_S) + \alpha(\mathbf{D}(\mathbf{u}_M) - \mathbf{D}(\mathbf{u}_S)), \quad (3.29b)$$

where $\mathbf{f} = \mathbf{f}_M = \mathbf{f}_S$. If the error $\mathbf{e} = \mathbf{u}_M - \mathbf{u}_S$ has a stable fixed point in the origin of the phase space, then $\mathbf{D}(\mathbf{u}_M) - \mathbf{D}(\mathbf{u}_S) = 0$, *i.e.*, the two outputs are equal.

In optoelectronic feedback systems, considered in this Thesis, the coupling between the two lasers is achieved through the photon density S . Furthermore, the slave system is operated with an open loop configuration, *i.e.*, there is not a feedback loop. The open loop configuration for the slave is more stable, with smaller synchronization error, than the closed loop configuration, because the synchronization error is strongly dependent on mismatches between the feedback delay times of the master and the slave [29,31]. For other

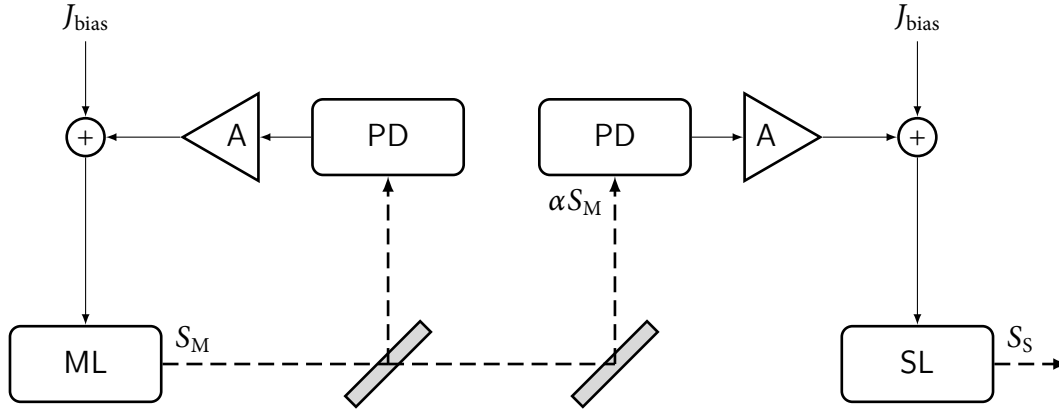


Figure 3.7: Schematic diagram of the connection from master to slave for synchronization (ML: master laser, SL: slave laser, PD: photodiode, A: amplifier, solid lines represent electrical links, whereas dashed lines are optical paths).

parameters, the dependence of the synchronization error is less impacted by mismatches, but still present [29].

Therefore for the dynamical system of Eqs. 3.17, the variables \mathbf{u}_M , \mathbf{u}_S are defined as:

$$\mathbf{u}_M(t) = (S_M(t), N_M(t)) \quad (3.30a)$$

$$\mathbf{u}_S(t) = (S_S(t), N_S(t)). \quad (3.30b)$$

and the driving signal is:

$$\mathbf{D}(\mathbf{s}(t)) = \alpha S_M(t). \quad (3.31)$$

The scheme of the coupling between the master and slave systems is shown in Fig. 3.7.

Synchronization Error

In order to quantify the synchronization quality, a synchronization error can be defined in terms of the statistical correlation coefficient $\Gamma_{M,S}$ ⁴ between the master and slave outputs.

The synchronization error ρ is then defined as the complement to one of the modulus of the correlation coefficient between the master and slave output power:

$$\rho = 1 - |\Gamma_{M,S}|, \quad (3.33)$$

where values near 0 indicate good synchronization, while values near 1 indicate very bad synchronization.

For instance, in Fig. 3.8, the outputs of the master laser (ML) and the slave laser (SL) for perfect matching of laser parameters are shown. The temporal range is taken after a

⁴For two signals X and Y , the correlation coefficient is a measure of the statistical dependence of the two signals. It is defined as:

$$\Gamma_{X,Y} = \text{corr}(X, Y) = \frac{\text{cov}(X, Y)}{\sigma_X \sigma_Y} = \frac{E[(X - \mu_X)(Y - \mu_Y)]}{\sigma_X \sigma_Y}, \quad (3.32)$$

where μ and σ refer to the mean and the standard deviation, and $\Gamma_{X,Y}$ is bounded in $-1 \leq \Gamma_{X,Y} \leq 1$. A value of $\Gamma_{X,Y}$ near 0 indicates that the two signals X and Y are weakly correlated, while values near 1 indicates a strong correlation.

transient of $t = 250$ ns, where the system is in a full chaotic state. Clearly, the output of the SL follow exactly the same evolution of the ML output. The synchronization diagram, shown in Fig. 3.9, represents the output of the SL as a function of the output of the ML. The diagram is very narrow, and this indicates a very good synchronization. Fig. 3.10 shows the time evolution of the master and slave outputs, when the differential gain parameter g_N of the SL differs of 10% from that of the ML, and, as shown in Fig. 3.11, the synchronization diagram is very confused and broad, indicating very poor synchronization.

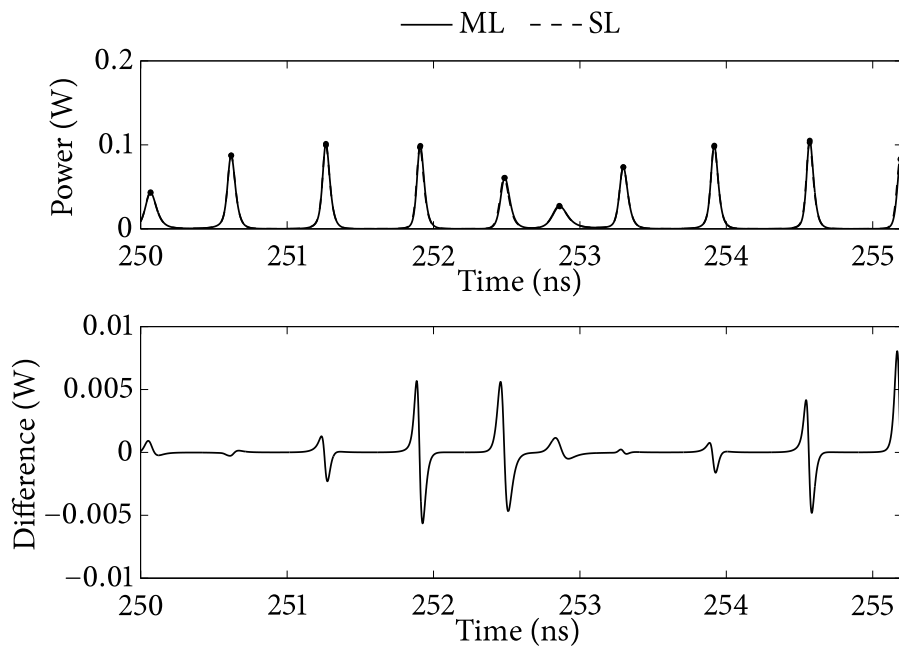


Figure 3.8: Outputs of the ML and SL with matched parameters.

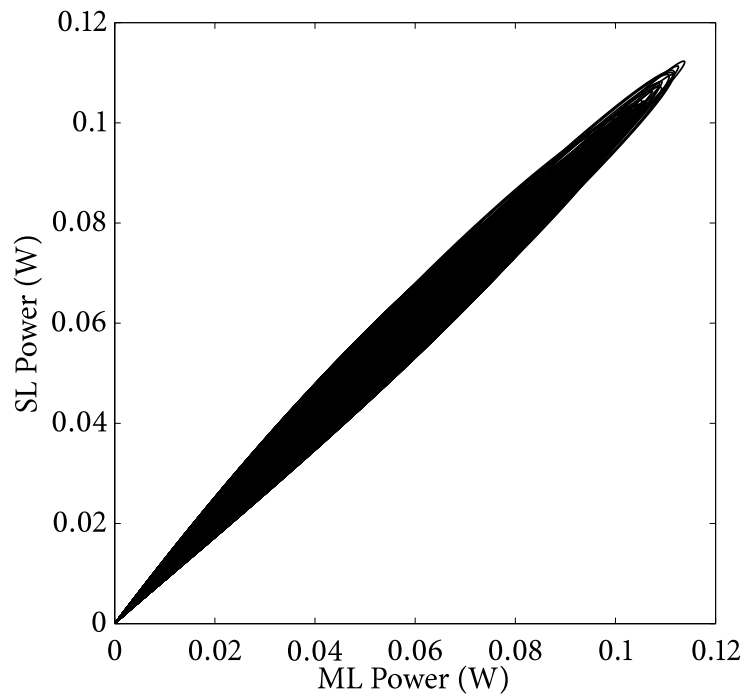


Figure 3.9: Synchronization diagram of the outputs of the ML and SL with matched parameters (the synchronization error is $\rho = 1.72 \times 10^{-3}$).

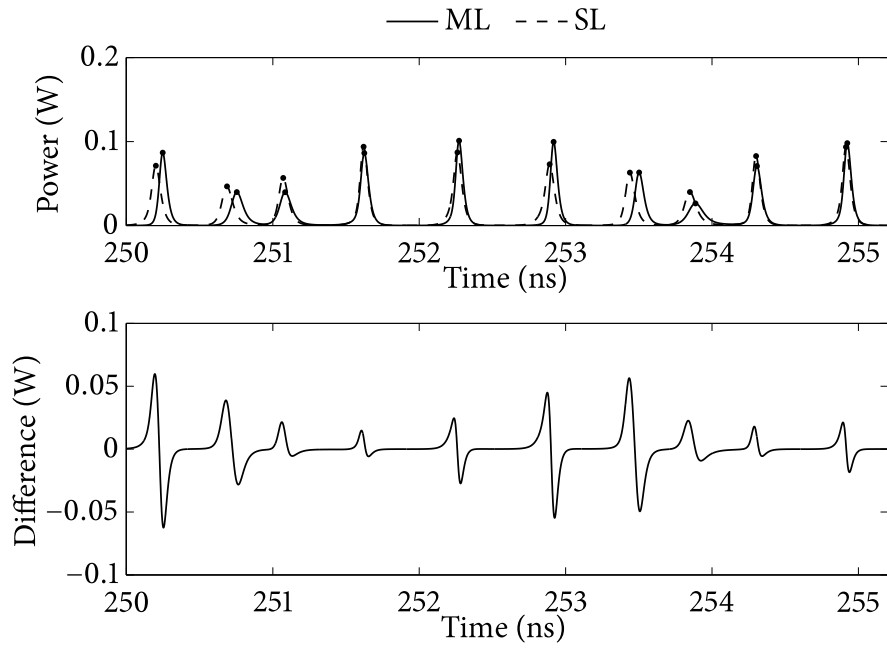


Figure 3.10: Outputs of the ML and SL with a difference of 10% in the SL differential gain parameter g_N in respect to that of the ML.

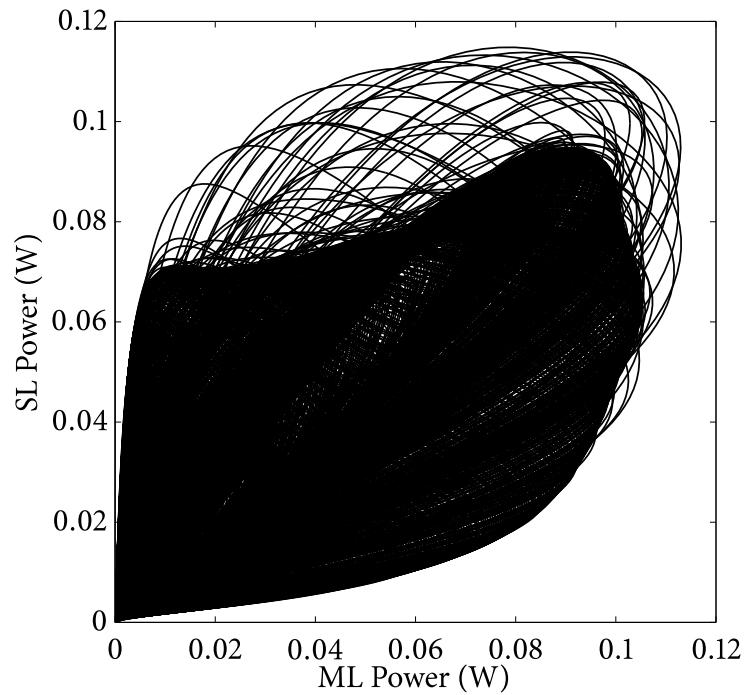


Figure 3.11: Synchronization diagram of the outputs of the ML and SL, when the differential gain parameter g_N of the SL differ of 10% from that of the ML (the synchronization error is $\rho = 9.92 \times 10^{-2}$).

Chapter 4

Chaotic Communication System

Scientists investigate that which already is;
engineers create that which has never been.

Albert Einstein (1879 – 1955)

This chapter provides an overview of an optical chaotic communication system operating in free-space. The building blocks and their interconnections will be explained in detail, together with some design choices which will be used in the numerical analysis of the system. Furthermore, the measure of the system performance will be defined.

Finally, an example of the signals at various points of the system, and for various parameters, is given.

4.1 Overview of the System

A picture of a secure digital communication system is given in Fig. 4.1, where the names Alice, Bob and Eve are commonly used in cryptography: Alice wants to send a message m to Bob in a way that Eve, the eavesdropper, can't understand.

To this aim the information message m must be appropriately transformed by the transmitter. If Eve intercepts the optical power signal P_{tx} at the transmitter output, or in any other point between the transmitter and the receiver, then she cannot recover the message m , because it is hidden or encrypted. At the receiver, the inverse transformation operated by the transmitter is applied to the power signal P_{rx} , and a message \hat{m} , close to the original message m , is recovered by Bob. All methods that operate in this way are called steganographic or cryptographic systems.¹

The aim of this Thesis is to analyze the performance of one of this schemes: a chaotic steganographic communication system working at the wireless infrared physical layer

¹A cryptographic system hides the meaning of the message, while a steganographic system hides its existence.

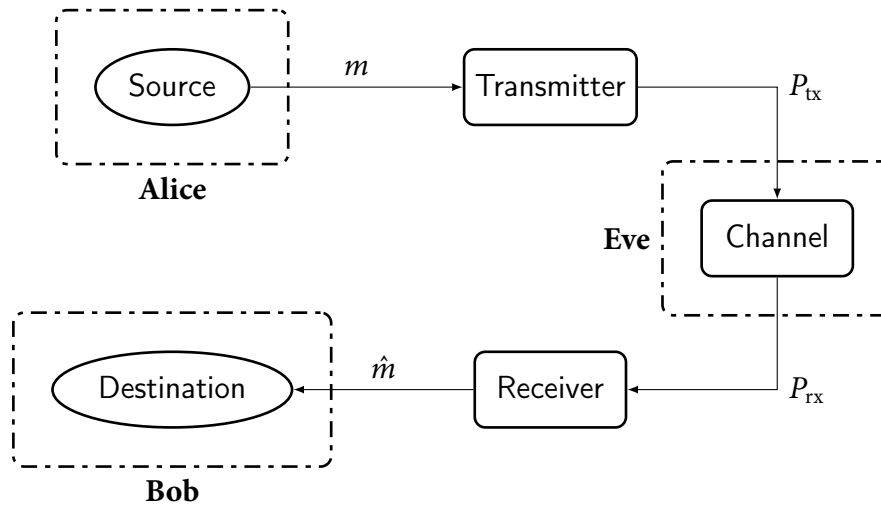


Figure 4.1: Generic model of a digital communication system.

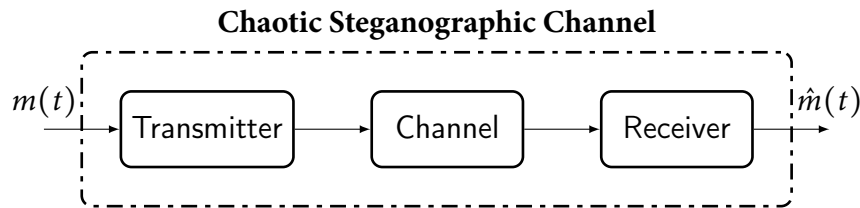


Figure 4.2: Chaotic communication channel.

(PHY/IR) (layer 1 of the ISO/OSI stack), which uses delayed optoelectronic feedback semiconductor lasers for the message hiding and recovering processes.

The message generated from the source is assumed to be PPM encoded, because PPM modulation is employed in most optical infrared communication systems, *e.g.*, in IEEE 802.11 and Irda standards.

Moreover, as shown in Fig. 4.2, for the source Alice, and the destination Bob, the system is equivalent to a digital channel.

4.2 The Source

As shown in Fig. 4.3, the source (Alice), generates a sequence of bits a_n , which encodes the information message m . The sequence a_n is then passed to the bit mapper. The bit mapper splits the sequence into groups, and then encodes each group into a symbol l . The

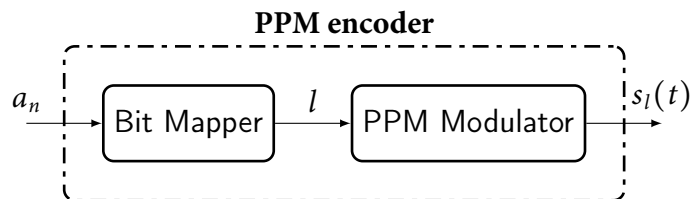


Figure 4.3: Scheme of a PPM encoder.

bits	l
00	0
01	1
10	2
11	3

Table 4.1: Bit mapping for 4-PPM.

PPM modulator, then, generates an appropriate signal $s_l(t)$ for each symbol, which will be passed to the transmitter for the chaotic masking and transmitting processes.

4.2.1 PPM Encoder

PPM is a baseband orthogonal modulation scheme in which the value of a symbol is encoded in the time position of a defined pulse within a given temporal frame.

In M -PPM, the bit mapper associates to each sequence of $k = \log_2 M$ bits a symbol l from the alphabet $\mathcal{A} = \{0, 1, 2, \dots, M-1\}$.

A common choice is to associate to each group of bits its decimal representation. An example of such a choice for the case of 4-PPM is shown in Table 4.1.

The modulator, then, generates an appropriate signal $s_l(t)$ based on the symbol l . For M -PPM, each signal $s_l(t)$ has the same duration $T_{\text{frame}} = T_{\text{bit}} \log_2 M$. Given a pulse shape $g(t)$, with unitary maximum duration and support in $-\frac{1}{2} \leq t \leq \frac{1}{2}$, the signal $s_l(t)$ is simply a shifted version of the pulse $g(t)$ with maximum duration $T_{\text{slot}} = T_{\text{frame}}/M$. The pulse can be shorter than the maximum allowed duration, *i.e.*, the pulse can have duration $T_{\text{pulse}} = dT_{\text{slot}}$, where $0 < d \leq 1$ is the duty cycle. Reducing the pulse duration can increase slot synchronization [32], at the cost of a larger bandwidth. A common choice used in this Thesis is $d = 0.5$.

The signal for symbol l is given by:

$$s_l(t) = g\left(\frac{t - \left(l + \frac{1}{2}\right) T_{\text{slot}}}{T_{\text{pulse}}}\right). \quad (4.1)$$

For instance, for the pulse $g(t) = \text{rect}(t)$, the signals are defined as:

$$s_l(t) = \text{rect}\left(\frac{t - \left(l + \frac{1}{2}\right) T_{\text{slot}}}{T_{\text{pulse}}}\right). \quad (4.2)$$

An example of transmitted signal for the symbol $l = 1$ is shown in Fig. 4.4, and in Fig. 4.5, the four signals in the case of 4-PPM, using the map given in Table 4.1, are presented. In Fig. 4.6, an example of a 4-PPM encoded signal is compared to a standard Non Return to Zero (NRZ) format, for the bit sequence 0100101101.

4.3 The Transmitter

The block scheme of the transmitter is shown in Fig. 4.7. The semiconductor laser with delayed optoelectronic feedback generates the optical chaotic carrier, as explained in Section 3.3.1.

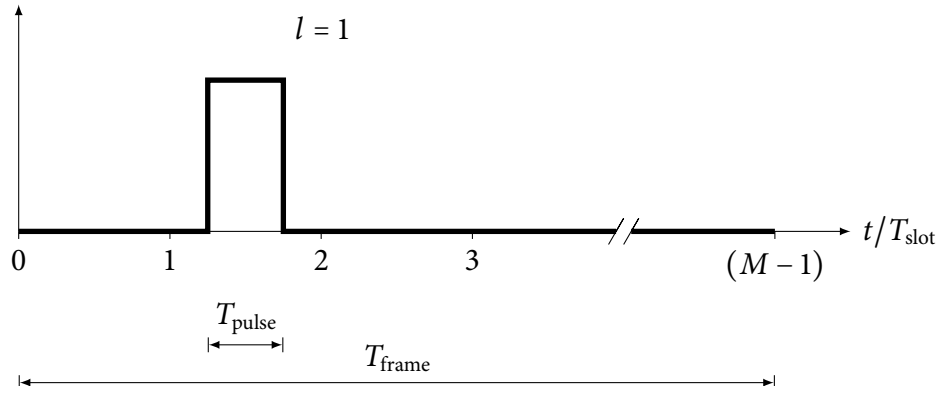


Figure 4.4: M -PPM signal structure for symbol $l = 1$ and pulse $g(t) = \text{rect}(t)$.

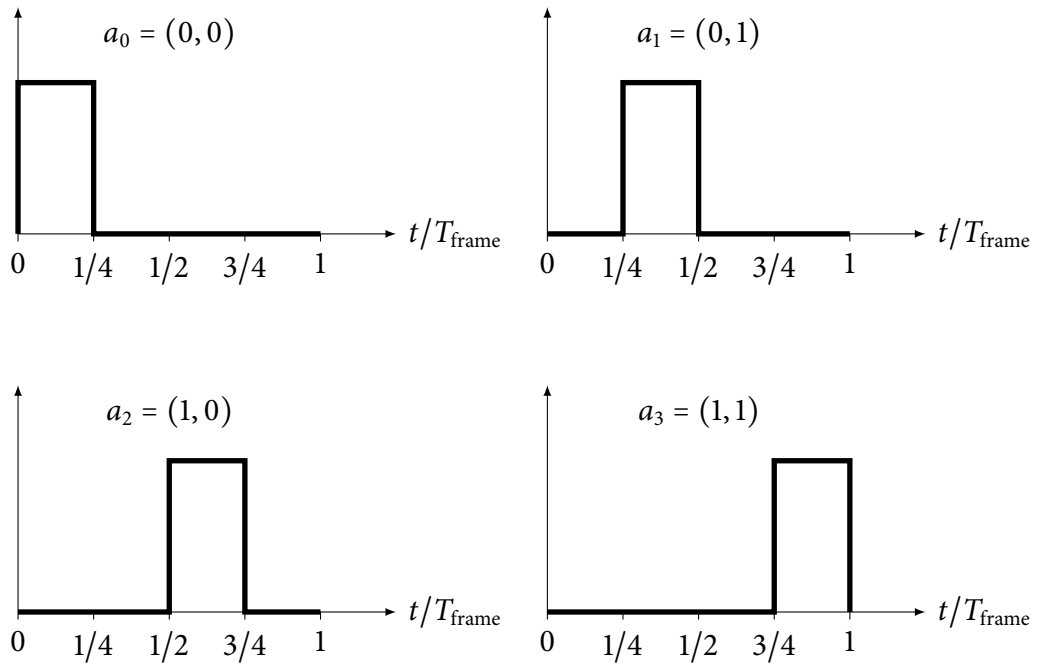


Figure 4.5: Signals used in 4-PPM.

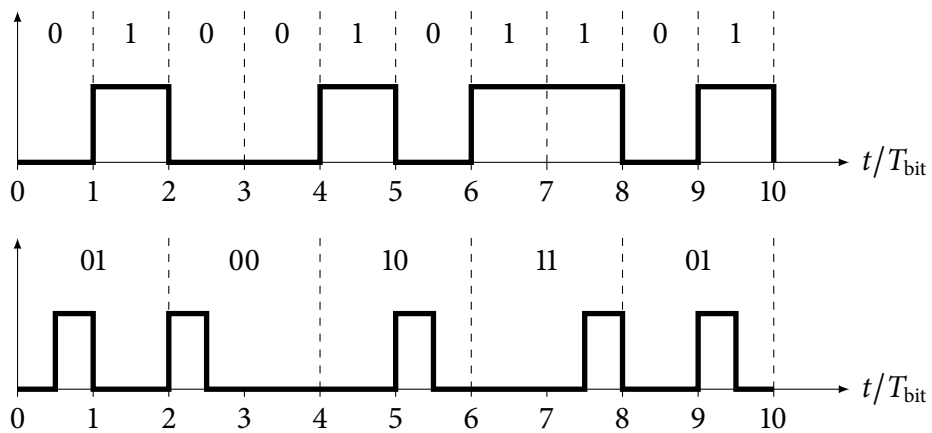


Figure 4.6: Example of a 4-PPM encoded signal compared to a standard NRZ encoding.

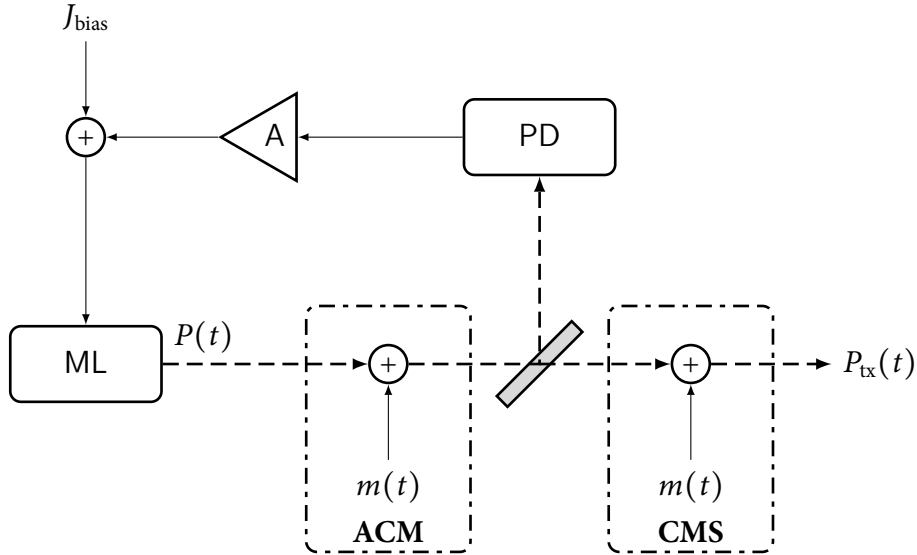


Figure 4.7: Scheme of the transmitter (ML: master laser, PD: photodiode, A: amplifier, solid lines represent electrical links, whereas dashed lines are optical paths).

There are different methods to superpose the message onto the chaotic carrier [12, 27]. Two of these schemes, considered in this Thesis, are the chaos masking (CMS) and the additive chaos modulation (ACM). Both of these two schemes work in a similar way: the message is simply superimposed on the optical chaotic carrier by an intensity modulation, e.g., by using a Mach-Zehnder modulator, and the transmitted power can be expressed as:

$$P_{\text{tx}}(t) = [1 + \zeta m(t)] P(t), \quad (4.3)$$

where ζ is the modulation depth, and $P(t)$ is the optical power emitted by the ML. The main difference is the point of the message injection. In CMS, the message is injected just before the transmitter output, while in ACM case the message is injected inside the feedback loop, and thus, contrary to the CMS, the message will alter the dynamics of the ML.

An example of message injection is shown in Fig. 4.8. As can be seen, the total transmitted optical power $P_{\text{tx}}(t)$ is the result of the superposition of the optical power $P(t)$, coming from the ML, and of a version of $P(t)$ itself modulated by the information message $m(t)$. In the figure, for the sake of clarity, the modulation depth $\zeta = 1$ has been chosen very high. Optimal values of the modulation depth ζ , to obtain good message masking, are in the order of 10^{-2} .

4.4 The Channel

4.4.1 Model of the Channel

The model of an infrared channel is illustrated in Fig. 4.9. The transmitter emits an optical power signal $P_{\text{tx}}(t)$. The optical power at the receiver is [33]:

$$P_{\text{rx}}(t) = (P_{\text{tx}} * h)(t) + N(t), \quad (4.4)$$

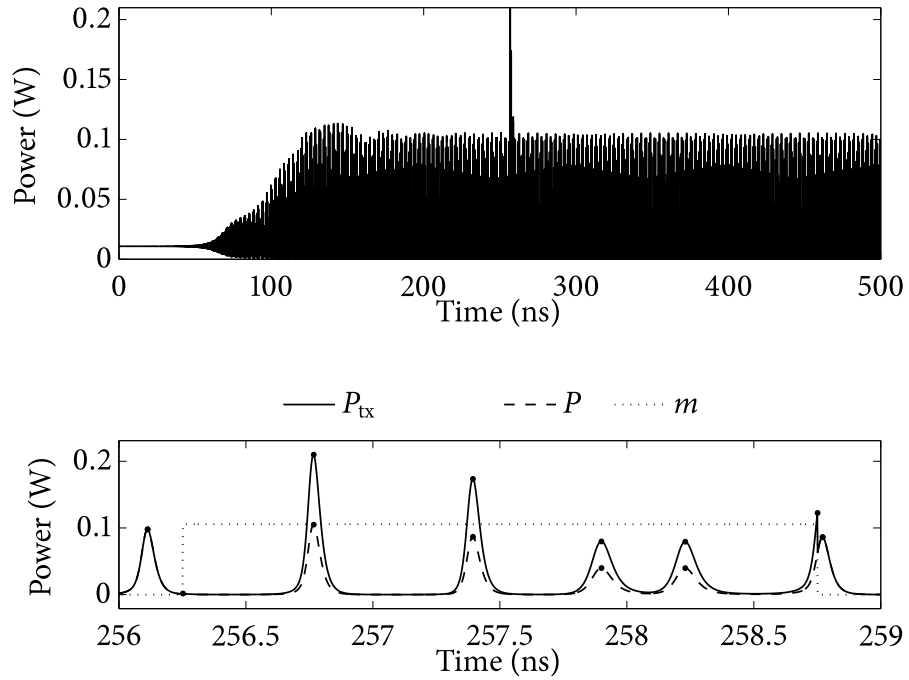


Figure 4.8: Example of a message injection onto a chaotic optical carrier: the bit rate is $R_{\text{bit}} = 100$ MHz. The upper plot is the transmitted power. The high peak is due to the exaggerated choice of $\zeta = 1$, as clarified in the bottom plot.

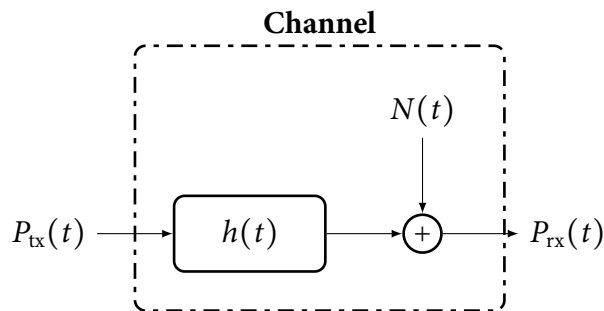


Figure 4.9: Model of an infrared channel.

where $h(t)$ is the impulse response of the channel, and $N(t)$ is an additive noise.

Eq. (4.4) is simply a linear filter with an additive noise. The input signal $P_{\text{tx}}(t)$ represents an instantaneous optical power, so it is a non negative quantity:

$$P_{\text{tx}}(t) \geq 0. \quad (4.5)$$

The average transmitted optical power is given by:

$$\overline{P_{\text{tx}}} = \lim_{T \rightarrow \infty} \frac{1}{2T} \int_{-T}^T P_{\text{tx}}(t) dt. \quad (4.6)$$

Excluding noise, the average received optical power is given by:

$$\overline{P_{\text{rx}}} = H(0)\overline{P_{\text{tx}}}, \quad (4.7)$$

where $H(f)$ is the Fourier transform of $h(t)$:

$$H(f) = \int_{-\infty}^{+\infty} h(t) e^{-j2\pi ft} dt, \quad (4.8)$$

and $H(0)$ is the channel direct current (DC) gain:

$$H(0) = \int_{-\infty}^{+\infty} h(t) dt. \quad (4.9)$$

4.4.2 Back To Back Channel

The BTB configuration is fundamental to analyze the generic system behavior.

It consists of studying the system in complete absence of the channel, with the optical power output P_{tx} of the transmitter directly injected, as the input power P_{rx} , to the receiver.

Indeed, referring to the general model of Fig. 4.9 and Eq. (4.4), the impulse response of the channel is a Dirac's delta:

$$h(t) = \delta(t), \quad (4.10)$$

and the noise is always zero:

$$N(t) = 0. \quad (4.11)$$

This configuration permits to test and analyze all the components of the system without the distortions and degradations introduced by the channel.

The system performance measured in BTB will serve primarily to search for good parameters of the system, e.g., the modulation depth ζ , and will also serve as a reference for the performance that will be measured when including the channel effects.

4.4.3 Indoor Channel

For a given set of source properties S , receiver properties R , and environment properties E , the baseband impulse response $h(t)$ is fixed and completely determined [34, 35], so the impulse response $h(t)$ can be written as $h_E(t; S, R)$.

In this Thesis the computation of the response function $h_E(t; S, R)$ is carried out using the software package *IrSimIt* [34]. In *IrSimIt*, the environment E is modeled as a set of N_b boxes $\{B_1, B_2, \dots, B_{N_b}\}$, as shown in Fig. 4.10. The box B_1 is the largest one, and

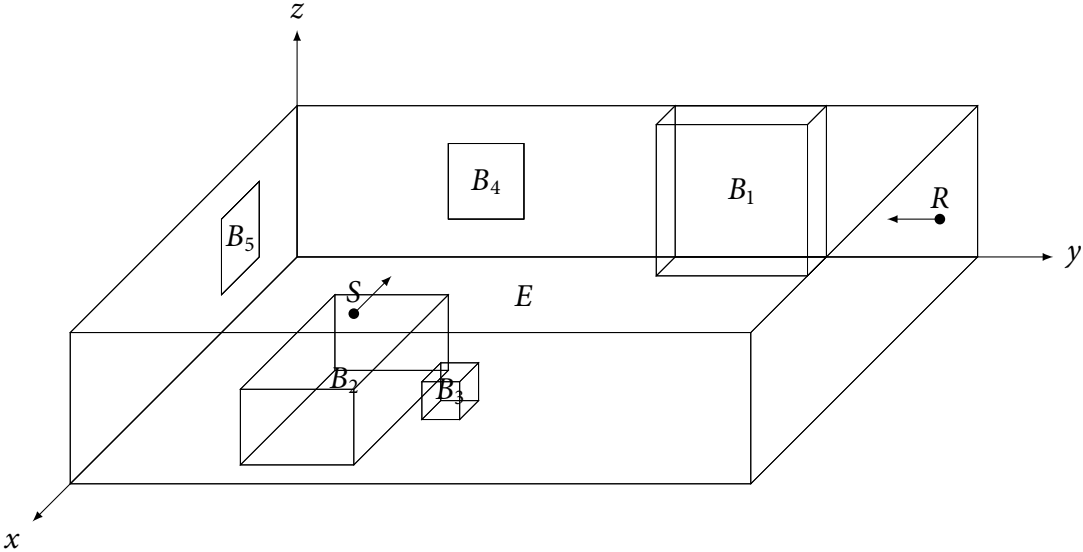


Figure 4.10: Model of an indoor environment.

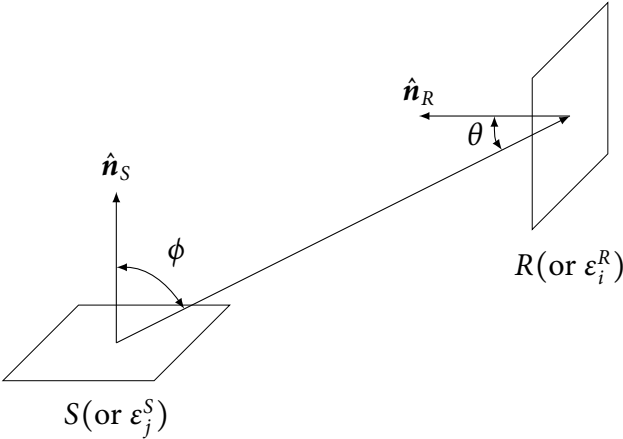


Figure 4.11: Source and receiver specification.

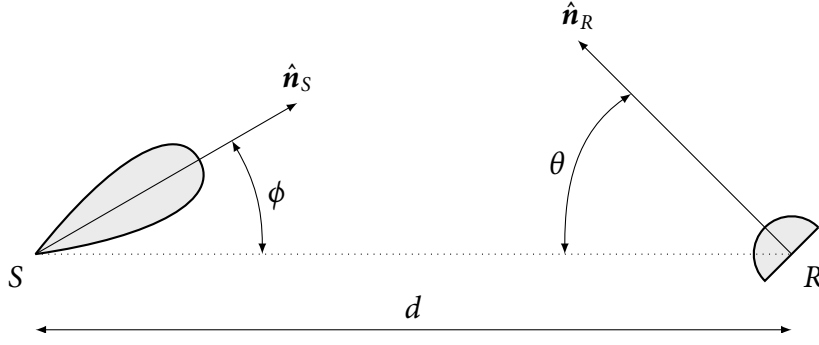


Figure 4.12: Geometric model for LOS propagation.

can represent a room, a floor or an entire building. The other boxes represent all internal objects, such as tables, windows, doors and so on.

As shown in Fig. 4.11, the source S is described by a position vector \mathbf{r}_S , an orientation vector $\hat{\mathbf{n}}_S$, and a radiation pattern $T(\phi)$. The radiation pattern is assumed to be a generalized Lambertian pattern of order n , defined as [33, 36]:

$$T(\phi) = \frac{n+1}{2} \cos^n \phi. \quad (4.12)$$

The order n can be calculated from the HWHM $\phi_{-3\text{dB}}$, by taking the logarithm base $\cos \phi$ of Eq. (4.12) for $\phi = \phi_{-3\text{dB}}$ (and so $T(\phi_{-3\text{dB}}) = 1/2$), which gives:

$$n = \frac{\ln 1/2}{\ln \cos \phi_{-3\text{dB}}}. \quad (4.13)$$

Each box B_i can have different reflection coefficients for each of its six faces. Each face F_j is modeled as a Lambertian diffusive surface of reflectivity ρ_{F_j} , *i.e.*, with a generalized Lambertian pattern of order $n = 1$:

$$T(\phi) = \cos \phi. \quad (4.14)$$

The receiver R is described by a position vector \mathbf{r}_R , an orientation vector $\hat{\mathbf{n}}_R$, an optical collection area A_R , and an effective optical area at incident angles θ defined as [34]:

$$A(\theta) = A_R g(\theta) = \begin{cases} A_R \cos(\theta) & \theta \leq \Psi_{\text{FOV}} \\ 0 & \text{otherwise.} \end{cases} \quad (4.15)$$

The angle Ψ_{FOV} is the HWHM at the receiver, *i.e.*, its field of view.

Line of Sight Impulse Response

The calculation of the line of sight (LOS) response function is quite straightforward.

The transmitter emits a radiant intensity I_{tx} (W sr^{-1}), which is related to the average transmitted power \overline{P}_{tx} of Eq. (4.6) by [33]:

$$I_{\text{tx}}(\phi) = \overline{P}_{\text{tx}} T(\phi). \quad (4.16)$$

The irradiance I_{rx} (W m^{-2}) at the receiver is:

$$I_{\text{rx}}(d, \phi) = \frac{I_{\text{tx}}(\phi)}{d^2} = \frac{\overline{P_{\text{tx}}} T(\phi)}{d^2}, \quad (4.17)$$

where, as shown in Fig. 4.12, $d = |\mathbf{r}_S - \mathbf{r}_R|$ is the distance between the transmitter and the receiver, and $T(\phi)$ is assumed to be normalized so that:

$$2\pi \int_0^\pi T(\phi) d\phi = 1. \quad (4.18)$$

The average received power is:

$$\overline{P_{\text{rx}}} = I_{\text{rx}}(d, \phi) A(\theta) = \frac{\overline{P_{\text{tx}}} T(\phi) A(\theta)}{d^2}, \quad (4.19)$$

so the DC gain of the channel is, from Eqs. (4.7) and (4.15):

$$H_{\text{LOS}}(0) = \frac{\overline{P_{\text{rx}}}}{\overline{P_{\text{tx}}}} = \begin{cases} \frac{A_R}{d^2} T(\phi) \cos(\theta) & \theta \leq \Psi_{\text{FOV}} \\ 0 & \text{otherwise.} \end{cases} \quad (4.20)$$

Furthermore, in the time domain, the impulse response becomes:

$$h(t) = H_{\text{LOS}}(0) \delta\left(t - \frac{d}{c}\right), \quad (4.21)$$

where c is the speed of light.

Total Impulse Response

To calculate the total impulse response, the reflections due to walls and objects have to be taken into account. If $h_E^{(k)}(t; S, R)$ is the impulse response due to signal undergoing exactly k bounces during its path from the transmitter to the receiver, then the total impulse response is given by [34]:

$$h_E(t; S, R) = \sum_{k=0}^{\infty} h_E^{(k)}(t; S, R). \quad (4.22)$$

The k -bounce impulse response $h_E^{(k)}(t; S, R)$ is calculated from the $(k-1)$ -bounce impulse response $h_E^{(k-1)}(t; S, R)$ as [34]:

$$h_E^{(k)}(t; S, R) = \int_E \rho_{d\epsilon} h_E^{(k-1)}(t; S, d\epsilon^R) * h_E^{(0)}(t; d\epsilon^S, R) d\epsilon, \quad (4.23)$$

where $d\epsilon$ is a differential surface in E , with reflectivity $\rho_{d\epsilon}$, and the quantities $d\epsilon^R$ and $d\epsilon^S$ represent a differential surface acting first as a receiver from the transmitter S , and then, as a transmitter to the receiver R .

Considering only M bounces, the total response $h_E(t; S, R)$ can be approximated as [34]:

$$h_E(t; S, R) \approx \sum_{k=0}^M h_E^{(k)}(t; S, R). \quad (4.24)$$

The integration of Eq. (4.24) is achieved by discretization of the faces F_i into smaller elements of size $1/P \cdot 1/P$, for a total of $N_i = P^2$ partitions ε_i . The total number of elements N is the sum of the number of elements per face N_i , over all faces F_i .

Eq. (4.23) is then estimated as [34]:

$$h_E^{(k)}(t; S, R) \approx \sum_{i=1}^N \rho_{d\varepsilon_i^R} h_E^{(k-1)}(t; S, d\varepsilon_i^R) * h_E^{(0)}(t; d\varepsilon_i^S, R). \quad (4.25)$$

The term $h_E^{(k-1)}(t; S, d\varepsilon_i^R)$ in Eq. (4.25) can be rewritten by using Eq. (4.25) itself with $R = \varepsilon_i^R$, which gives:

$$\begin{aligned} h_E^{(k)}(t; S, \varepsilon_i^R) &\approx \sum_{j=1}^N \rho_{d\varepsilon_j^R} h_E^{(k-1)}(t; S, d\varepsilon_j^R) * h_E^{(0)}(t; d\varepsilon_j^S, d\varepsilon_i^R) \\ &= \sum_{j=1}^N \alpha_{ij} h_E^{(k-1)}(t - \tau_{ij}; S, d\varepsilon_j^R), \end{aligned} \quad (4.26)$$

where

$$\alpha_{ij} = V(\mathbf{r}_{\varepsilon_j^S}, \mathbf{r}_{\varepsilon_i^R}, E) \frac{\rho_{\varepsilon_j^R} T(\phi_{ij}) g(\theta_{ij})}{P^2 d_{ij}^2}, \quad (4.27)$$

and

$$\tau_{ij} = \frac{d_{ij}}{c} = \frac{|\mathbf{r}_{\varepsilon_j^S} - \mathbf{r}_{\varepsilon_i^R}|}{c}. \quad (4.28)$$

The function $V(\mathbf{r}_{\varepsilon_j^S}, \mathbf{r}_{\varepsilon_i^R}, E)$ is a visibility function which is 1 if the elements ε_j^S and ε_i^R are in line of sight, and 0 otherwise.

In Fig. 4.13, the first 4-bounces impulse responses for the environment defined in Table 4.2 are shown. The response in the bottom graph is the effective response of the channel excluding the LOS component ($k = 0$). The DC gain of each component is compared with that of the LOS in Fig. 4.14.

4.5 The Receiver

The scheme of the receiver is shown in Fig. 4.15. First, the received optical power P_{rx} is demodulated by a direct detection (DD) process using a photodetector. The electrical signal resulting from the photodetection is then injected to the SL. As explained in Section 3.3.2, the slave laser is operated with an open loop configuration, *i.e.*, there is not a feedback loop.

The message $\hat{m}(t)$ is then recovered by a simple difference between the signal photodetected from the received power, and the SL output, after another photodetection process. The low-pass filter (LPF) used after the difference has a bandwidth of $B_{\text{LPF}} = 1/T_{\text{pulse}}$, where T_{pulse} is the pulse duration of the message, as explained in Section 4.2.

If the SL is matched with the ML, the output of the SL is a replica of the carrier generated by the ML through the synchronization process. By considering the message $m(t)$ injected at the transmitter as a perturbation of its natural chaotic evolution, the difference operation just reveals this perturbation, *i.e.*, it recovers a message $\hat{m}(t)$ which should be a replica of the source message $m(t)$.

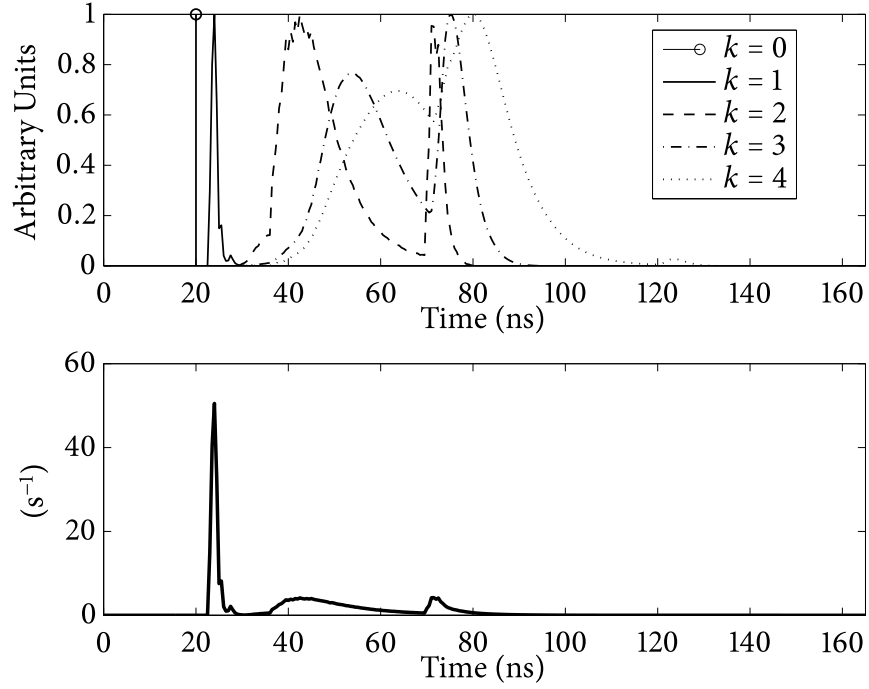


Figure 4.13: Example of k -bounces impulse responses: in the upper are shown the k -bounces responses (normalized to 1), and in the bottom the global response excluding the LOS component for $k = 0$.

Description	Parameter	Value
divisions per meter	P	4
room size	L_x	7.5 m
	L_y	5.5 m
	L_z	3.5 m
walls reflectivities	$\rho(x = 0)$	0.58
	$\rho(x = L_x)$	0.56
	$\rho(y = 0)$	0.12
	$\rho(y = L_y)$	0.30
	$\rho(z = 0)$	0.69
	$\rho(z = L_z)$	0.09
location of S	\mathbf{r}_S	(0.75, 2.75, 1.75)m
elevation of S (angle from x - y plane)		0 deg
azimuth of S (angle in x - y plane)		0 deg
transmitter HWHM	$\phi_{-3\text{dB}}$	15 deg
location of R	\mathbf{r}_R	(6.75, 2.75, 1.75)m
elevation of R (angle from x - y plane)		0 deg
azimuth of R (angle in x - y plane)		180 deg
receiver area	A_R	$1 \times 10^{-4} \text{ m}^2$
receiver FOV	Ψ_{FOV}	60 deg

Table 4.2: Parameters used for the channel of Fig. 4.13.

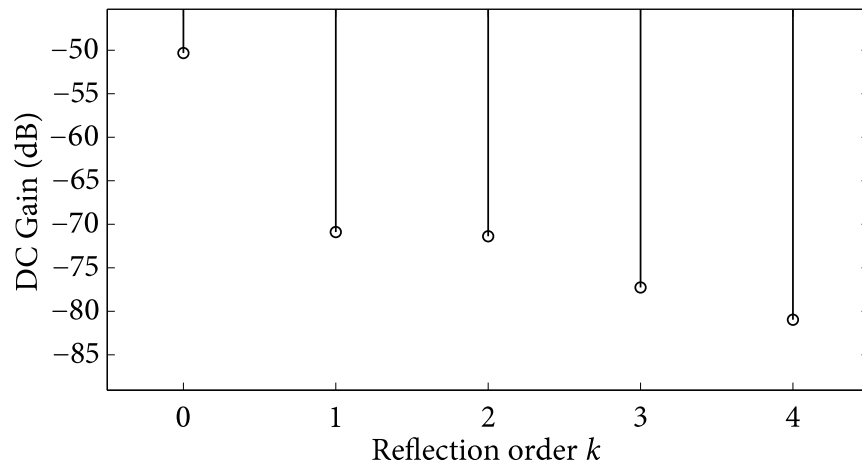


Figure 4.14: DC gain of the components shown in Fig. 4.13.

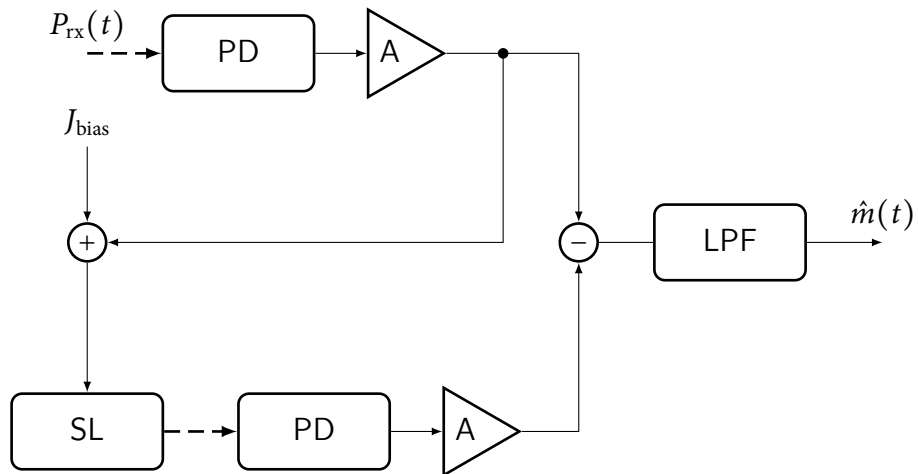


Figure 4.15: Scheme of the receiver (SL: slave laser, PD: photodiode, A: amplifier, LPF: low-pass filter, solid lines represent electrical links, whereas dashed lines are optical paths).

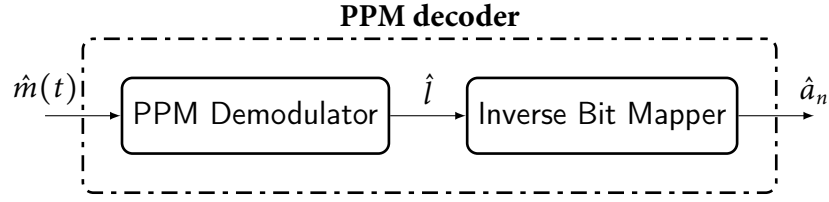


Figure 4.16: Block scheme of a PPM decoder.

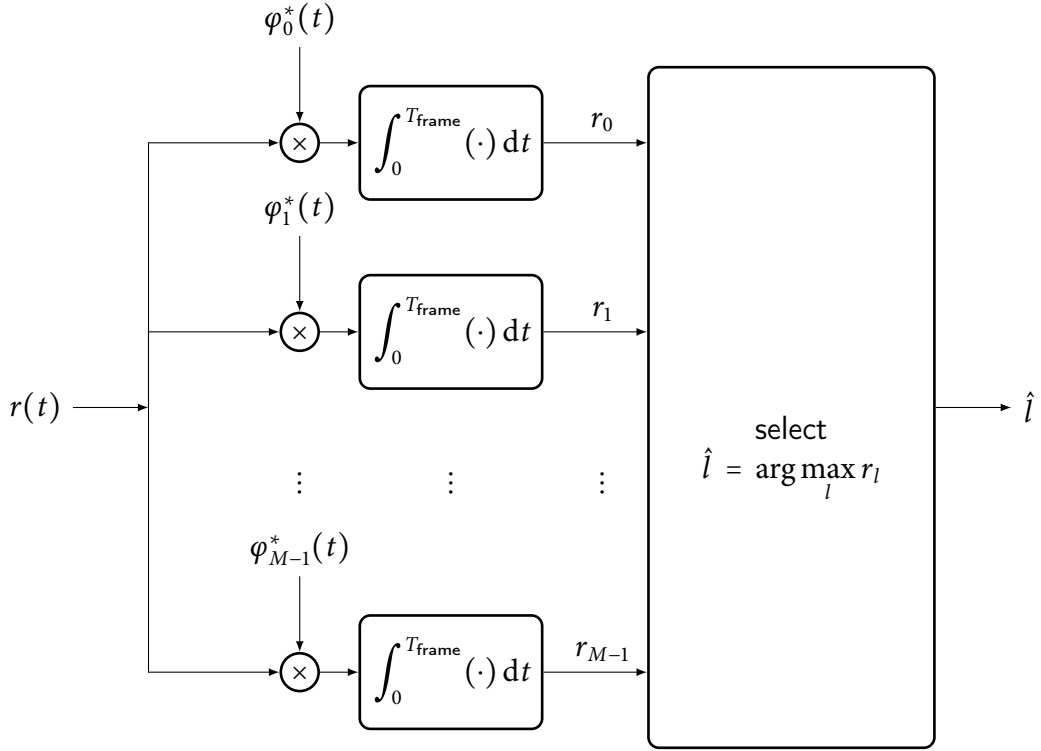


Figure 4.17: Block scheme of a MLD [37].

4.6 Message Decoding

The scheme of a PPM decoder is shown in Fig. 4.16. The recovered message signal $\hat{m}(t)$, after a synchronization with a proper clock, is split in frames of duration T_{frame} ; each frame is then passed to the PPM demodulator, which, using a maximum likelihood detector (MLD), estimates which one of the M symbols $l = 0, 1, \dots, M - 1$ has been transmitted. An inverse bit mapper, then, applies the inverse mapping used at the source, *e.g.*, the mapping in Table 4.1, and gives out the bit sequence \hat{a}_n .

4.6.1 PPM decoder

The MLD [37], shown in Fig. 4.17, by observing the received signal $r(t) = \hat{m}(t)$, estimates which one of the M symbols $l = 0, 1, \dots, M - 1$ has been transmitted.

As discussed in Section 4.2, the source sends one of the signal $s_l(t)$. The received signal $r(t)$, in the case of additive noise $n(t)$, is then given by:

$$r(t) = s_l(t) + n(t). \quad (4.29)$$

The MLD calculates the projections of $r(t)$ over the base $\{\varphi_0, \varphi_1, \dots, \varphi_{M-1}\}$, and then selects the one which is maximum. This is equivalent to choose the signal $s_l(t)$ with the minimum distance from the received signal $r(t)$. Moreover, the simplest setup of a MLD, for the case of a PPM constellation, is to integrate the received signal over each slot, and then to select the one which yields the maximum in the frame.

4.6.2 Symbol Error Probability

The isolated signals $s_l(t)$ of Eq. (4.1) are orthogonal with support in $[0, T_{\text{frame}}]$, each of them with energy:

$$E_s = \int_0^{T_{\text{frame}}} |s_l(t)|^2 dt. \quad (4.30)$$

A basis for these signals is:

$$\varphi_l(t) = \frac{s_l(t)}{\sqrt{E_s}}, \quad l = 0, 1, \dots, M-1 \quad (4.31)$$

and each signal can be represented in a vectorial space by [37]:

$$\begin{aligned} \mathbf{s}_0 &= \sqrt{E_s}(1, 0, 0, \dots, 0) \\ \mathbf{s}_1 &= \sqrt{E_s}(0, 1, 0, \dots, 0) \\ &\vdots \\ \mathbf{s}_{M-1} &= \sqrt{E_s}(0, 0, 0, \dots, 1). \end{aligned} \quad (4.32)$$

Under the hypothesis that signal $s_l(t)$ is transmitted, the conditional probability of the received signal $r(t)$ being correct is given by [37]:

$$\begin{aligned} P[\mathbf{r} = \mathbf{s} | \mathbf{s} = \mathbf{s}_l] &= P\left[\bigcap_{\substack{i=0 \\ i \neq l}}^{M-1} r_i > r_l\right] \\ &= \int_{-\infty}^{+\infty} p_{r_l}(a) \prod_{\substack{i=0 \\ i \neq l}}^{M-1} \int_{-\infty}^a p_{r_i}(b_i) db_i da. \end{aligned} \quad (4.33)$$

The components r_i are given by:

$$r_i = \langle \mathbf{r} | \mathbf{s}_i \rangle = E_s \delta_{il} + \sqrt{E_s} w_i, \quad (4.34)$$

where δ_{il} is the Kronecker's delta, and w_i are the noise components. By assuming additive white Gaussian noise (AWGN), the probability of the symbol of being correct is:

$$\begin{aligned} P_c &= P[\mathbf{r} = \mathbf{s} | \mathbf{s} = \mathbf{s}_l] \\ &= \frac{1}{\sqrt{2\pi\sigma_l^2}} \int_{-\infty}^{+\infty} e^{-\frac{(a-\mu_l)^2}{2\sigma_l^2}} \left[1 - \frac{1}{2} \operatorname{erfc}\left(\frac{a-\mu_n}{\sqrt{2\sigma_n^2}}\right)\right]^{M-1} da, \end{aligned} \quad (4.35)$$

where μ_l, σ_l^2 are the mean and the variance of the decision point, and μ_i, σ_i^2 , for $i \neq l$, are those of the noise components. The complementary error function $\operatorname{erfc}(a)$ is defined as [37]:

$$\operatorname{erfc}(a) = \frac{2}{\sqrt{\pi}} \int_a^{+\infty} e^{-b^2} db. \quad (4.36)$$

Finally, the symbol error probability is given by:

$$P_e = 1 - P_c. \quad (4.37)$$

4.6.3 Bit Error Probability

If $M = 2^k$ is a power of two, then each signal s_l has a binary representation of k bits. A signal error occurs if any of the bits is incorrectly received, which happens with probability P_e given by Eq. (4.37). For each transmitted symbol, of the $M - 1$ possible wrong received symbols, only $M/2$ yield a wrong bit, indeed, the bit error probability is given by [37]:

$$P_{\text{bit}} = \frac{M/2}{M-1} P_e = \frac{2^{k-1}}{2^k - 1} P_e. \quad (4.38)$$

4.6.4 Bit Error Rate and Q Factor

The bit error rate (BER) is the ratio of the wrong detected bits to the total number of transmitted bits:

$$\text{BER} = \frac{\# \text{ of wrong bits}}{\# \text{ of transmitted bits}}. \quad (4.39)$$

The Q factor is a parameter implicitly defined as [38]:

$$\text{BER} = \frac{1}{2} \operatorname{erfc} \left(\frac{Q}{\sqrt{2}} \right), \quad (4.40)$$

Indeed, the Q factor is calculated from the BER, by inverting Eq. (4.40), as:

$$Q = \sqrt{2} \operatorname{erfc}^{-1} (2\text{BER}). \quad (4.41)$$

For a typical optical communication system, a BER of 10^{-9} is the reference value of a good system. A BER of 10^{-9} corresponds to a $Q_{\text{dB}} = 15.6$ dB, with $Q_{\text{dB}} = 20 \log_{10} Q$. A plot of the Q factor as a function of the BER is shown in Fig. 4.18.

The usual way to estimate the BER (or the Q factor) via numeric simulations is to use a Monte Carlo method [39]. The use of such a method requires a huge amount of computational time and memory, due to the high accuracy needed to numerical modeling the chaotic carrier generation and processing through the various stages of the system. Furthermore, in this Thesis, the Q factor is estimated as follows:

1. each simulation is performed for an adequate number N of random realizations;
2. for each realization i , the bit error probability $P_{\text{bit}}(i)$ is estimated by using Eq. (4.38);
3. the BER for the realization i is taken equal to the bit error probability $P_{\text{bit}}(i)$, and the Q factor is calculated, by using Eq. (4.41);
4. the final Q factor is estimated by a mean over all the realizations:

$$Q_{\text{avg}} = \frac{1}{N} \sum_{i=1}^N Q(i) \quad (4.42a)$$

$$Q_{\text{dB}} = 20 \log_{10} Q_{\text{avg}}. \quad (4.42b)$$

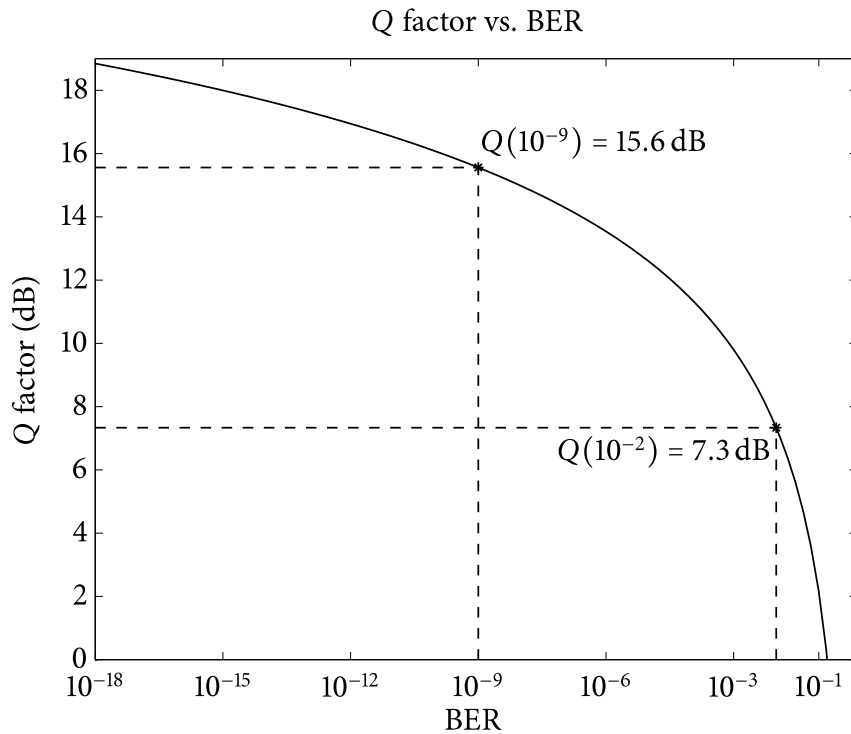


Figure 4.18: Q factor vs. BER.

4.7 System Performance

The system performances of the system are evaluated in terms of the synchronization error ρ , defined in Section 3.3.2, and of the Q factors at two different points. The synchronization error gives an indication of the goodness of the coupling between the ML and the SL, whereas the Q factor measured just after the transmitter serves to quantify how good is the system in hiding the message, and the Q factor measured after the receiver gives an evidence of how good is the system in recovering the message.

4.7.1 Example

An example of the message as seen by the source Alice, by the eavesdropper Eve (with DD) and by the destination Bob, with the receiver explained in Section 4.5, is shown in Fig. 4.19. As it can be seen, the message is absolutely undetectable by Eve. The negative ripple following the positive pulse, seen by Bob, is an effect caused by the synchronization process with the CMS scheme. The eye diagrams at the frame level, for a message of 24 bits, are shown in In Fig. 4.20, together with the values of the Q factor. If the modulation depth ζ is too strong, the transmitted power P_{tx} can show up some information about the message. The same message as in Figs. 4.19 and 4.20, but with an higher modulation depth ζ , is shown in Figs. 4.21 and 4.22. These figures clearly shows that now Eve can decode the message. As mentioned in Section 3.3.2, the SL must be similar as possible to the ML. For instance, in Figs. 4.23 and 4.24 the recovered message in the case the parameters of the SL are not matched with those of the ML, is shown. If Eve uses such a receiver, instead of a DD, then she cannot recover the message. As a drawback, if such a receiver is used by Bob, then the communication becomes totally unreliable.

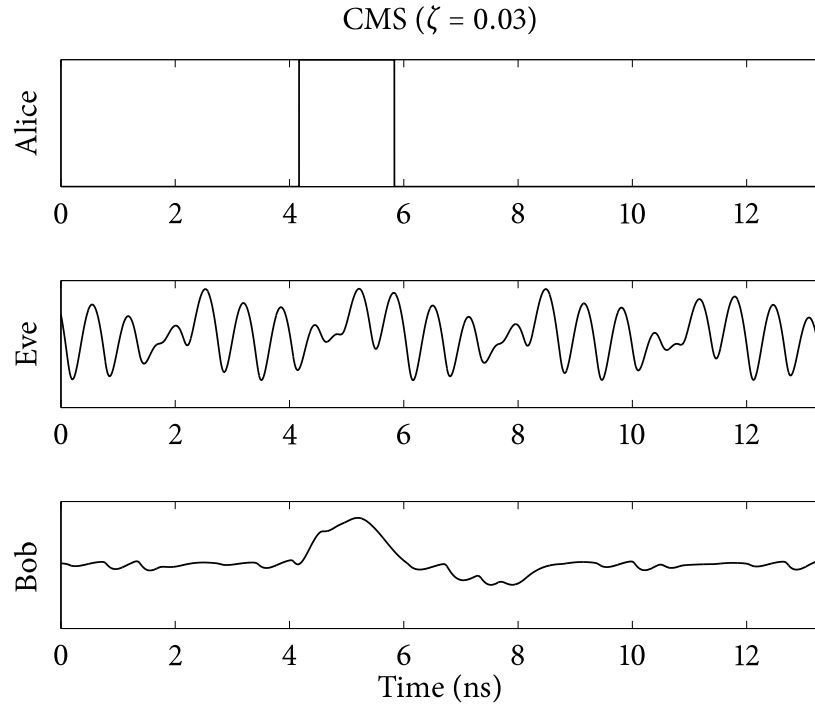


Figure 4.19: Example of a message (bits 01) as seen by Alice, Bob and Eve for the CMS scheme with a modulation depth of $\zeta = 0.03$ and bit rate $R_{\text{bit}} = 150$ MHz.

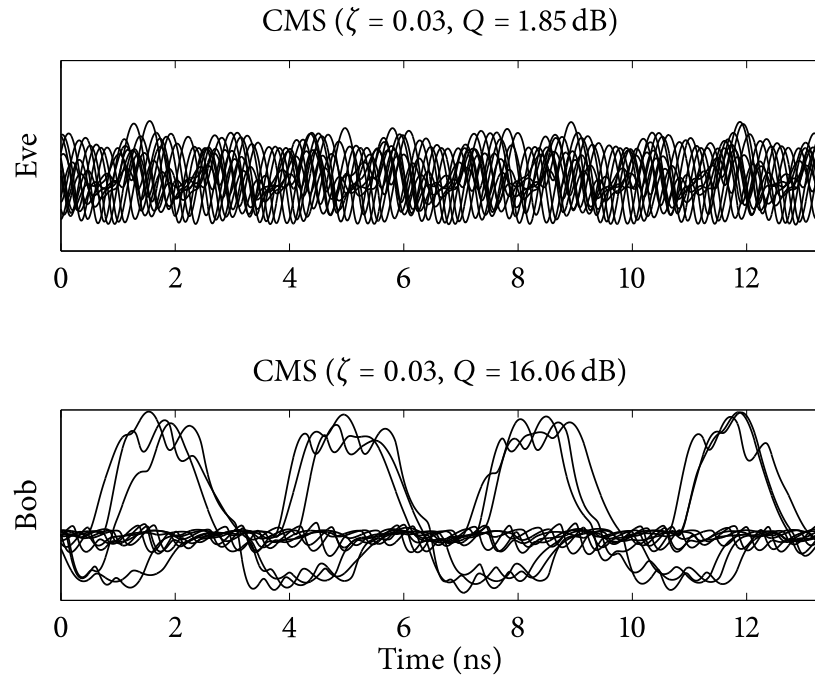


Figure 4.20: Frame level eye diagrams as seen by Bob and Eve for the CMS scheme with a modulation depth of $\zeta = 0.03$, bit rate $R_{\text{bit}} = 150$ MHz, and a message of 24 bits.

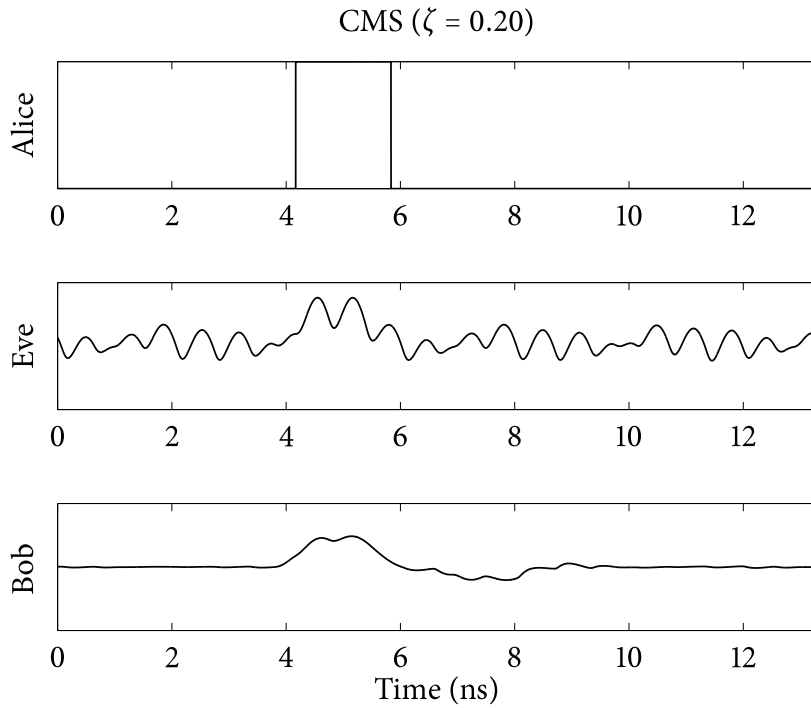


Figure 4.21: Example of a message (bits 01) as seen by Alice, Bob and Eve for the CMS scheme with a modulation depth of $\zeta = 0.2$ and bit rate $R_{\text{bit}} = 150$ MHz.

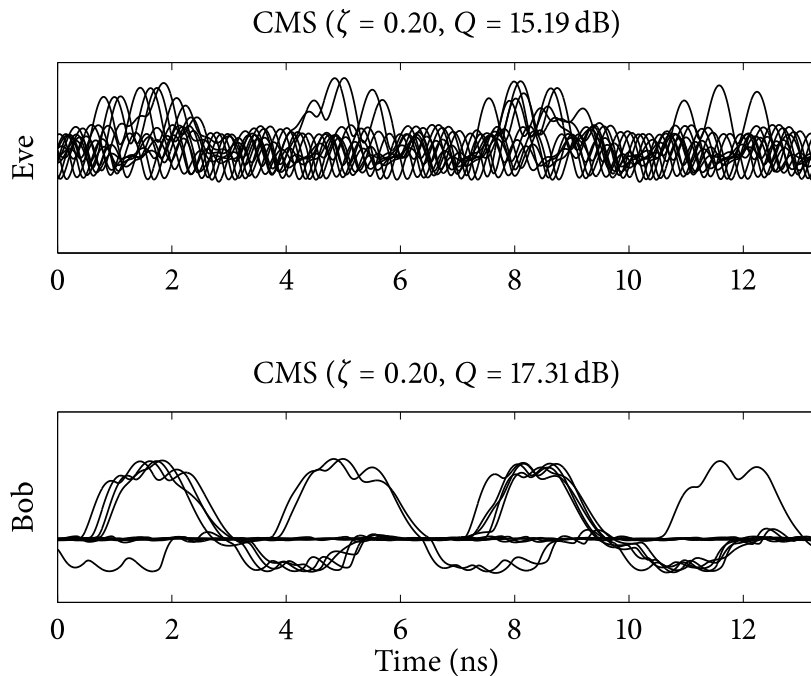


Figure 4.22: Frame level eye diagrams as seen by Bob and Eve for the CMS scheme with a modulation depth of $\zeta = 0.2$, bit rate $R_{\text{bit}} = 150$ MHz, and a message of 24 bits.

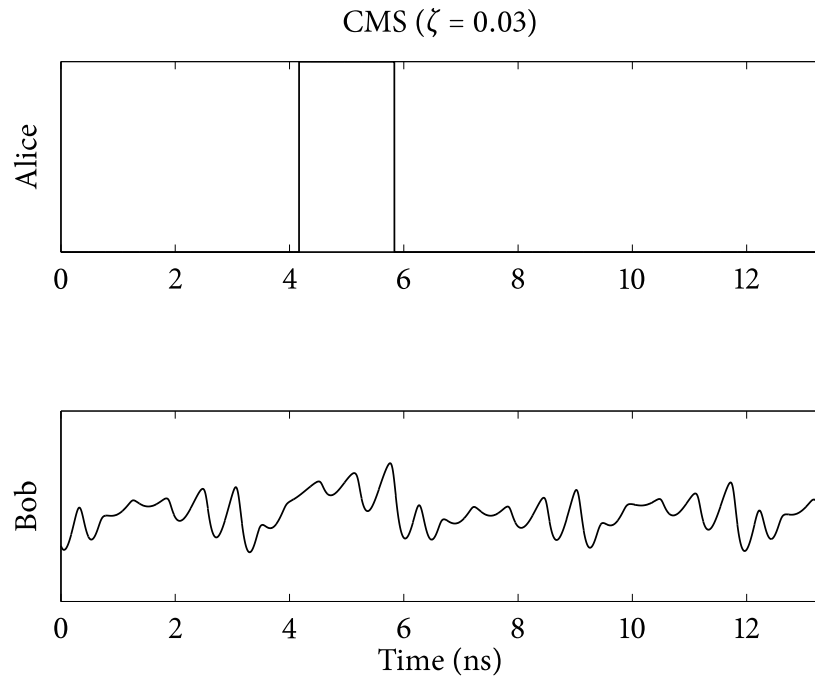


Figure 4.23: Example of a message (bits 01) as seen Bob (or Eve) for the CMS scheme with a modulation depth of $\zeta = 0.03$, bit rate $R_{\text{bit}} = 150$ MHz, and where the receiver differs of 10% in the SL differential gain parameters g_N in respect to that of the ML.

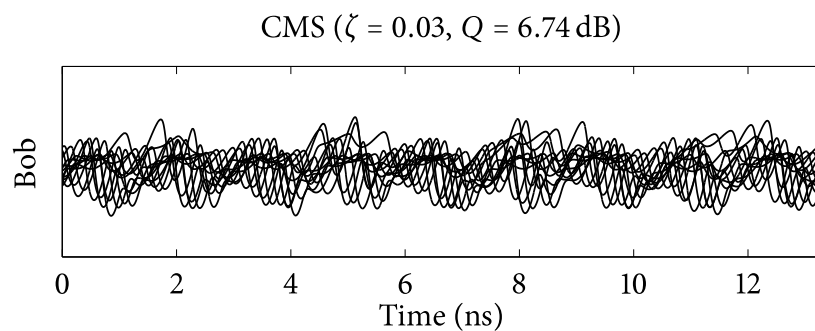


Figure 4.24: Frame level eye diagrams as seen by Bob (or Eve) for the CMS scheme with a modulation depth of $\zeta = 0.03$, bit rate $R_{\text{bit}} = 150$ MHz, and a message of 24 bits, and where the receiver differs of 10% in the SL differential gain parameters g_N in respect to that of the ML.

Chapter 5

Numerical Analysis

No amount of experimentation can ever prove me right; a single experiment can prove me wrong.

Albert Einstein (1879 – 1955)

In this chapter the main results obtained from numerical simulations are presented.

At first, several simulations are performed for the BTB channel configuration, obtaining useful information regarding the setting of some parameters of the system, *e.g.*, the modulation depth ζ and the maximum allowed bit rate.

Then, a simulation for the LOS propagation will show that the receiver must employ a variable gain amplifier in order to maintain the synchronization error into an acceptable range.

Finally, the propagation in a closed indoor environment is considered, and several simulations are performed by varying the transmitter position, orientation and radiation pattern.

Furthermore, while some proposed solutions are easily implementable in an existing system, *e.g.*, the variable amplifier stage, others must be carefully considered at the design phase, *e.g.*, the semiconductor lasers parameters.

5.1 System Specifications

The numerical analysis has been performed by using the scientific computational software `Matlab`. All the simulations are performed for a minimum of 100 statistical realizations of the chaotic waveform and noise, and for each realization a pseudo random message of 128 bit is generated. The system performance is calculated as explained in Section 4.7. The transient time after which the message is embedded onto the chaotic carrier has been chosen to be 250 ns, where the ML output is in a fully chaotic state.

Description	Parameter	Value
wavelength	λ	1550 nm
active region area	A_a	$10 \times 10^{-21} \text{ m}^2$
active region volume	V_a	$150 \times 10^{-18} \text{ m}^3$
active region refractive index	n_a	3.6
linewidth enhancement factor	α	4
confinement factor	Γ	0.4
photon decay rate	γ_c	$240 \times 10^9 \text{ s}^{-1}$
photon lifetime	τ_{ph}	$4.1667 \times 10^{-12} \text{ s}^{-1}$
carrier decay rate	γ_s	$1.458 \times 10^9 \text{ s}^{-1}$
carrier lifetime	τ_s	$685.8711 \times 10^{-12} \text{ s}^{-1}$
steady-state carrier density	N_0	$1 \times 10^{24} \text{ m}^{-3}$
steady-state photon density	S_0	$202.5 \times 10^{18} \text{ m}^{-3}$
normalized bias current density	\tilde{J}_{bias}	1/3
bias current	I_{bias}	$46.7143 \times 10^{-3} \text{ A}$
differential gain	g_N	$5 \times 10^{-12} \text{ m}^3 \text{ s}^{-1}$
gain saturation	g_S	$-15 \times 10^{-12} \text{ m}^3 \text{ s}^{-1}$
differential carrier relaxation rate	γ_n	$1.0125 \times 10^9 \text{ s}^{-1}$
nonlinear carrier relaxation rate	γ_p	$1.2150 \times 10^9 \text{ s}^{-1}$
relaxation frequency	f_r	2.49 GHz
feedback delay time	τ	2.6024 ns
normalized feedback delay time	$\hat{\tau}$	6.48
feedback strength	ξ	0.1

Table 5.1: Parameters of the semiconductor lasers.

The two semiconductor lasers, the one at the transmitter and the one at the receiver, are modeled by using Eqs. 3.21. The simulations are performed by using the numerical integration scheme explained in Appendix A. The time step h is appropriately adjusted based on the type of the message and channel being used, but it is always upper bounded by $h_{\text{MAX}} = 1 \text{ ps}$. The parameters of both semiconductor lasers are listed in Table 5.1.

The photodetector in the feedback loop of the transmitter has been considered ideal, *i.e.*, in the Eqs. 3.21, $f(t) = \delta(t)$. The other photodetectors are modeled as explained in Appendix B, and their band limited behavior is modeled by using a 3rd order Butterworth filter. The parameters of the photodetectors are listed in Table 5.2.

5.2 Modulation Depth

The system performance for 4-PPM, by varying the bit rate R_{bit} and the modulation depth ζ , are shown in Figs. 5.1 to 5.3.

The synchronization error ρ , shown in Fig. 5.1, decreases by increasing the bit rate, and also by decreasing the modulation depth. This can be explained by considering, for example, Fig. 4.8: if the bit rate is increased (or if the modulation depth is decreased) then the net effect is a reduction of the pulse duration (or amplitude), *i.e.*, of the pulse energy. By reducing the pulse energy, the perturbation superimposed onto the chaotic carrier by

Description	Parameter	Value
responsivity	R	0.95 A W^{-1}
dark current	I_D	20 nA
ambient temperature	T	290 K
equivalent load resistance	R_{eq}	50Ω
bandwidth	B_{ph}	30 GHz

Table 5.2: Parameters of the photodetectors.

the message injection, at the transmitter, gets lower and, indeed, the synchronization error is expected to diminish.

The behavior of the Q factor is shown in Figs. 5.2 and 5.3. The quality of the system in hiding the message can be viewed in Fig. 5.2, where, except for the 100 Mbit s^{-1} and $\zeta = 0.2$ cases, all the values are below the 7.33 dB line. Clearly, for higher values of the modulation depth ζ , the probability for Eve to intercept the message is also higher. At 100 Mbit s^{-1} , the message tends to emerge, due to its higher energy, and also due to the low amplitude of the chaotic signal in the base band. The ACM scheme performs better than the CMS, because, as explained in Section 3.3.1, in the ACM case, the dynamics of the ML is affected by the message, and thus the message gains higher masking.

The recovery of the message at the receiver is more problematic, as shown in Fig. 5.3. For both modulation schemes, the quality of the recovery rapidly decay after 300 Mbit s^{-1} and tends to saturate for high ζ . In particular, for $\zeta = 0.03$, the ACM scheme behave optimally up to 250 Mbit s^{-1} , whereas the CMS scheme is optimal only for 150 Mbit s^{-1} and 300 Mbit s^{-1} . For 200 Mbit s^{-1} and 250 Mbit s^{-1} the CMS scheme performs worse, because for these bit rates the negative retarded ripple created by the synchronization process tends to overlap the correct one and to lower it by the difference process (see, for example, Fig. 4.19).

By inspecting Figs. 5.2 and 5.3, a bit rate $R_{bit} = 150 \text{ Mbit s}^{-1}$, together with a message depth of $\zeta = 0.03$, leads to an high hiding of the message from Eve, and at the same time to a good message recovery at the receiver Bob, with both the CMS and ACM schemes. Furthermore, when not otherwise specified, in the following these two parameters values will be used. In Figs. 5.4 and 5.5, the behavior of the CMS and ACM schemes are compared with this choice of parameters.

5.3 Lasers Mismatches

The need for good matching of lasers parameters is shown in Fig. 5.6. The system, for example, can tolerate a maximum change of about 5% of the gain parameter g_N of the SL in respect to that of the ML. An higher variation leads to a fast decay of the performance.

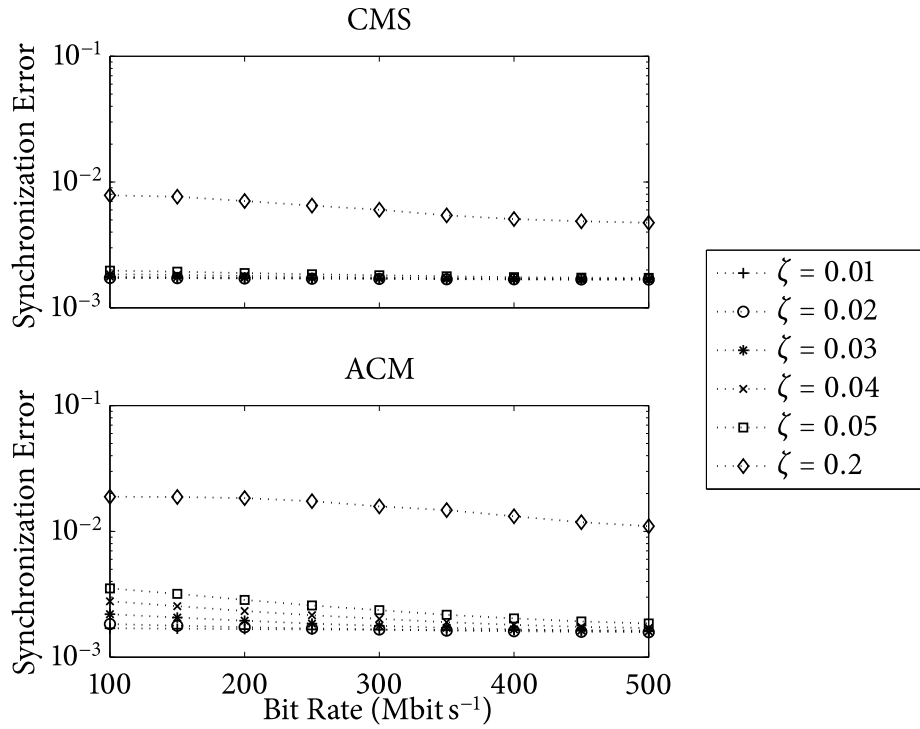


Figure 5.1: Synchronization error vs. bit rate for various modulation depths ζ .

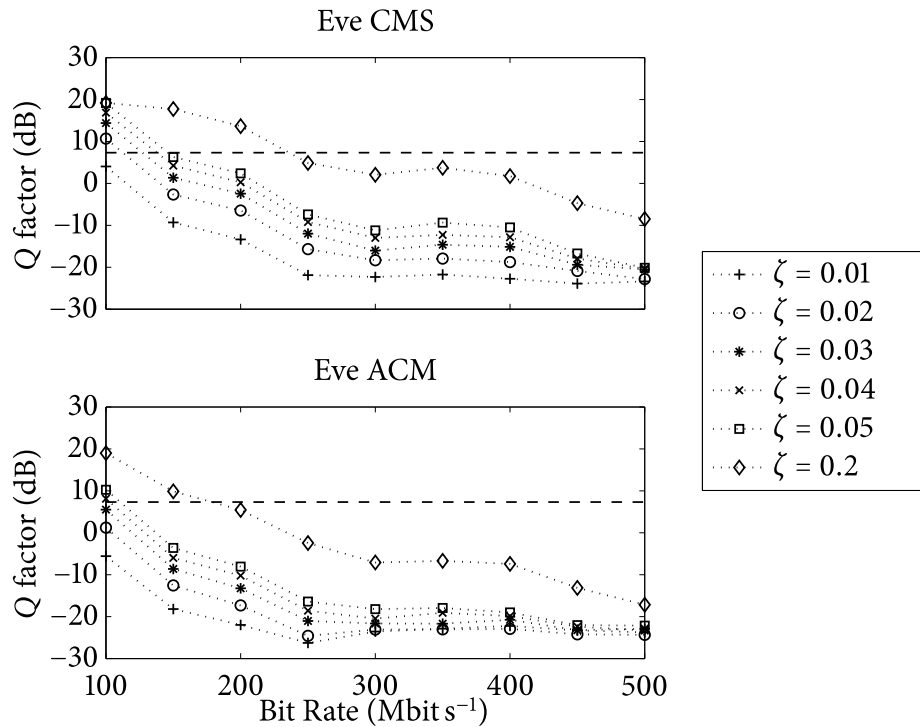


Figure 5.2: Q factor for Eve vs. bit rate for various modulation depths ζ .

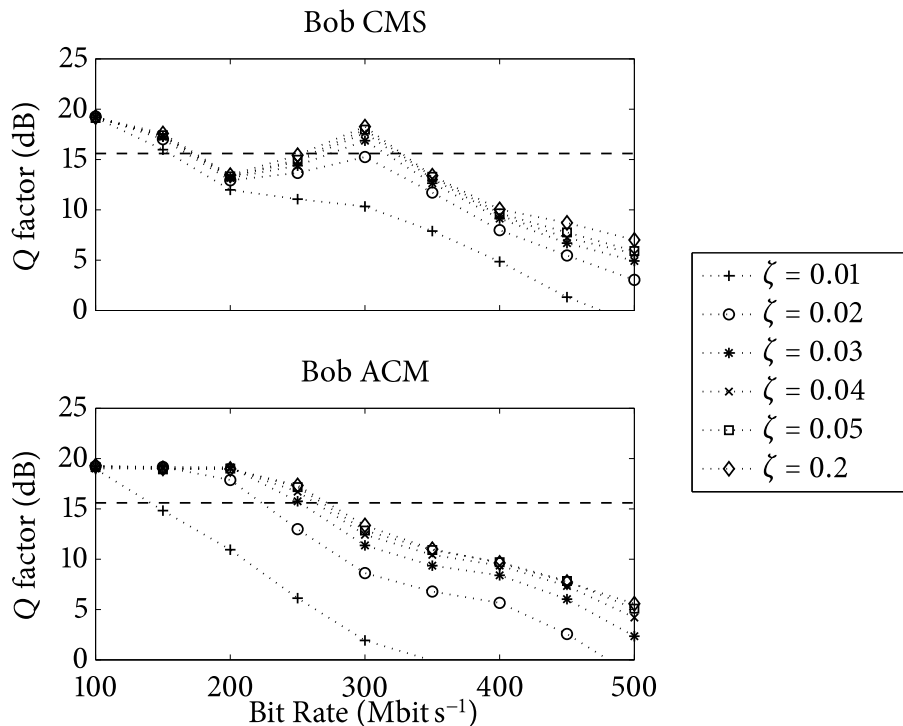


Figure 5.3: Q factor for Bob vs. bit rate for various modulation depths ζ .

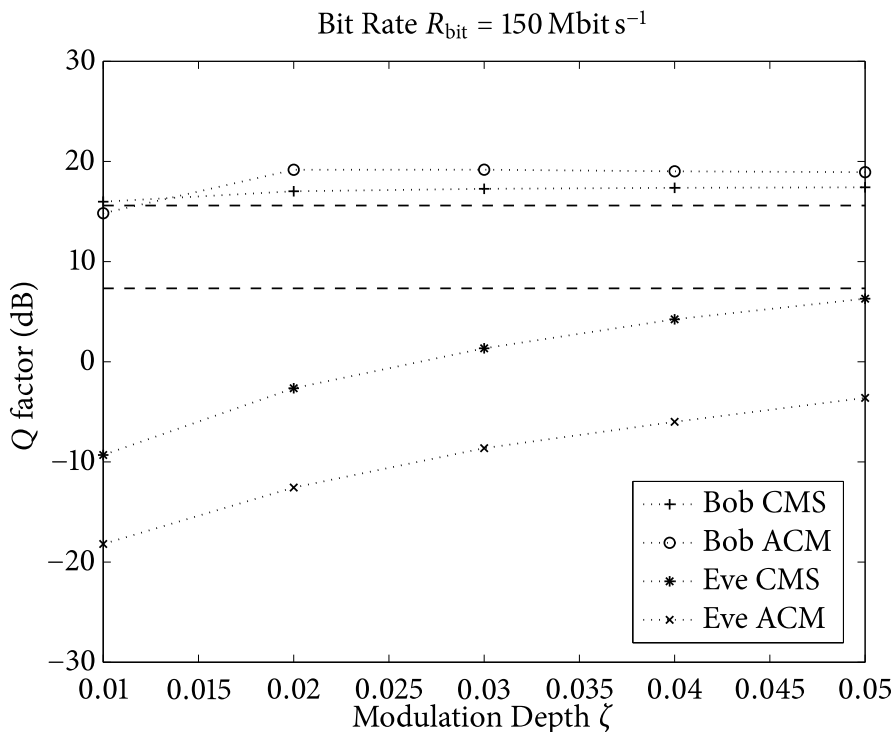


Figure 5.4: Q factor vs. modulation depth ζ , for a bit rate of $R_{\text{bit}} = 150 \text{ Mbit s}^{-1}$.

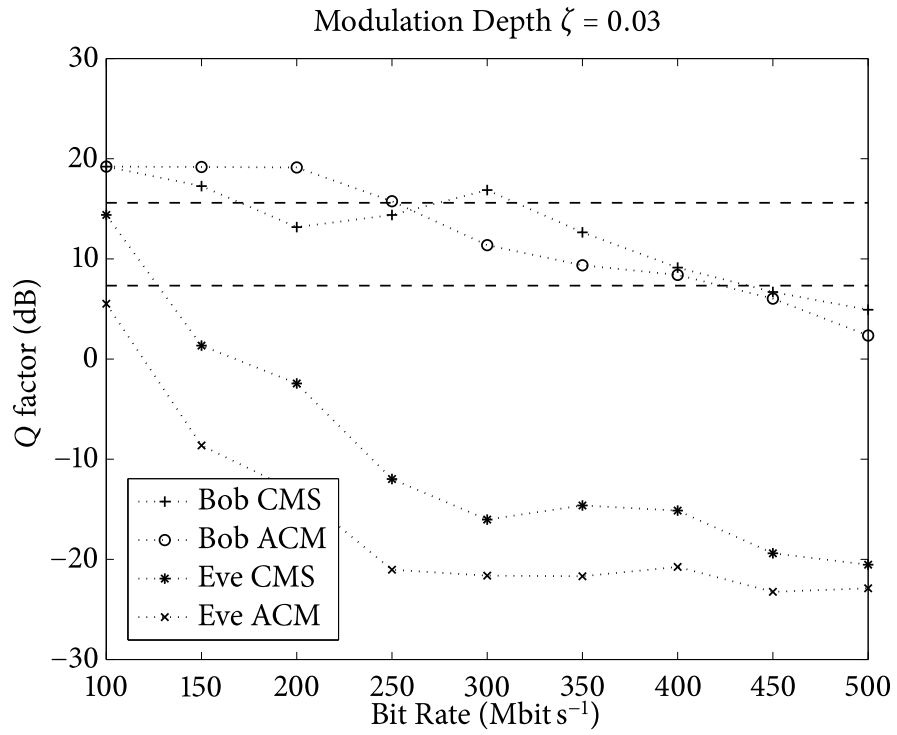


Figure 5.5: Q factor vs. bit rate R_{bit} , for a modulation depth of $\zeta = 0.03$.

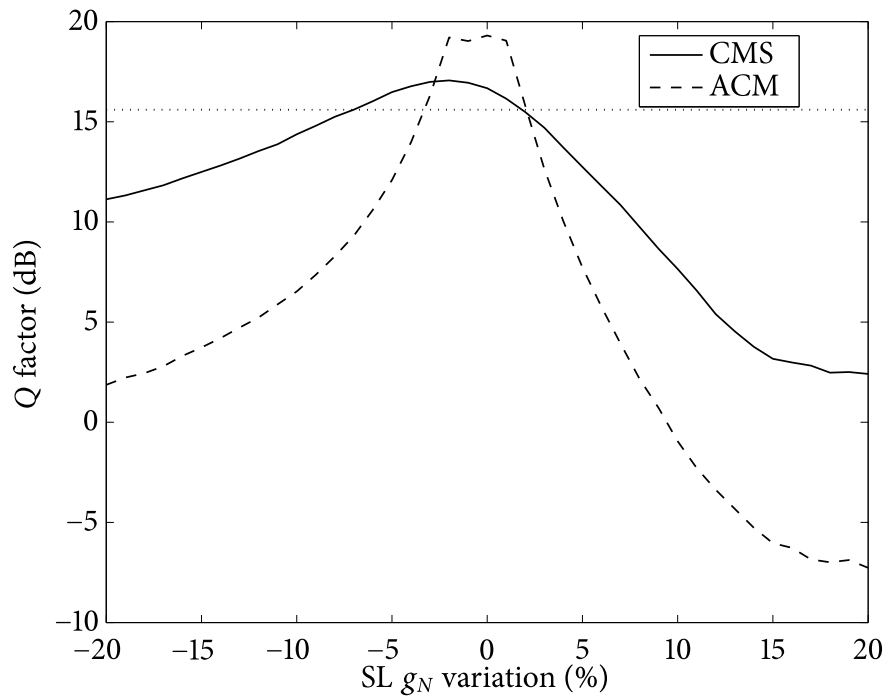


Figure 5.6: Q factor vs. SL gain parameter g_N variation in respect to that of the ML.

5.4 The Role of the Relaxation Frequency f_r

In Figs. 5.7 to 5.12 the system performance are shown by varying the PPM order and duty cycle. The synchronization errors, shown in Figs. 5.7 and 5.8, all follow similar behaviors, which can be explained with the same arguments given in Section 5.2: by increasing the PPM order or the bit rate, the net pulse energy decreases and the synchronization is improved.

By inspecting the Q factor, shown in Figs. 5.9 to 5.12, the ACM scheme performs better than the CMS in both message hiding and recovery. Clearly, by increasing the duty cycle the message recovery quality is increased, at the cost of enhancing also the possibility for Eve to decode the message. However, by increasing the duty cycle, as it can be seen, another good working point for both scheme is at a bit rate of $R_{\text{bit}} = 300$ MHz.

The maximum achievable bit rate is limited by the relaxation frequency f_r of the laser: a qualitative demonstration can be carried out by considering, for example, Fig. 3.6: for stable pulsing, the pulsing frequency is close to the relaxation frequency f_r of Eq. (3.25). In chaotic state, the pulse spacing is not constant, but as a roughly approximation, it can be considered to be equal to that of stable oscillation:

$$T_r \approx \frac{1}{f_r}. \quad (5.1)$$

By observing Fig. 4.8, in order for a message pulse to modulate at least one entire laser pulse, it must be:

$$T_{\text{pulse}} > T_r, \quad (5.2)$$

which, by using the following relation with the bit time

$$T_{\text{pulse}} = \frac{d \log_2 M}{M} T_{\text{bit}}, \quad (5.3)$$

can be rewritten as:

$$T_{\text{bit}} > \frac{M}{d \log_2 M} T_r. \quad (5.4)$$

By taking the reciprocal the relation becomes:

$$R_{\text{bit}} < \frac{d \log_2 M}{M} f_r, \quad (5.5)$$

which is an intrinsic limit for the specific system used in this Thesis. For instance, by following these arguments, the maximum achievable bit rate in the case of 4-PPM with duty cycle $d = 0.5$ and, from Table 5.1, with a relaxation frequency of $f_r = 2.49$ GHz, is:

$$R_{\text{bit,MAX}} = \frac{1}{4} f_r = 622.5 \text{ Mbit s}^{-1}. \quad (5.6)$$

This result, however, is not strictly related with the effective achievable bit rate having good performance, which, as it has been shown in the previous section, is about one half of it.

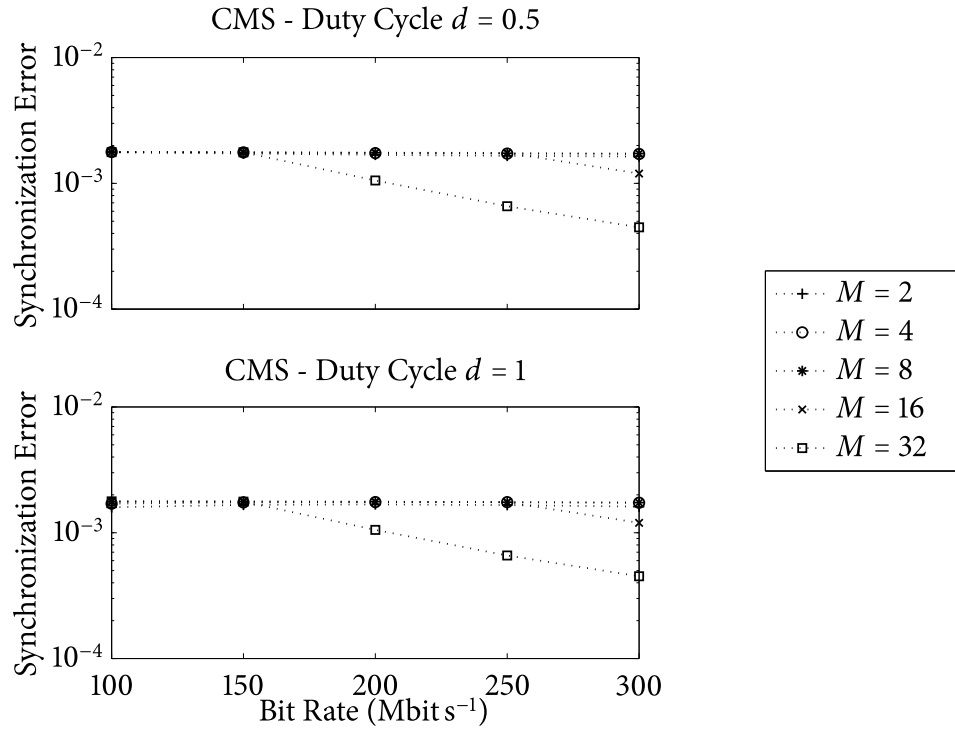


Figure 5.7: Synchronization error vs. bit rate for various PPM orders, CMS case.

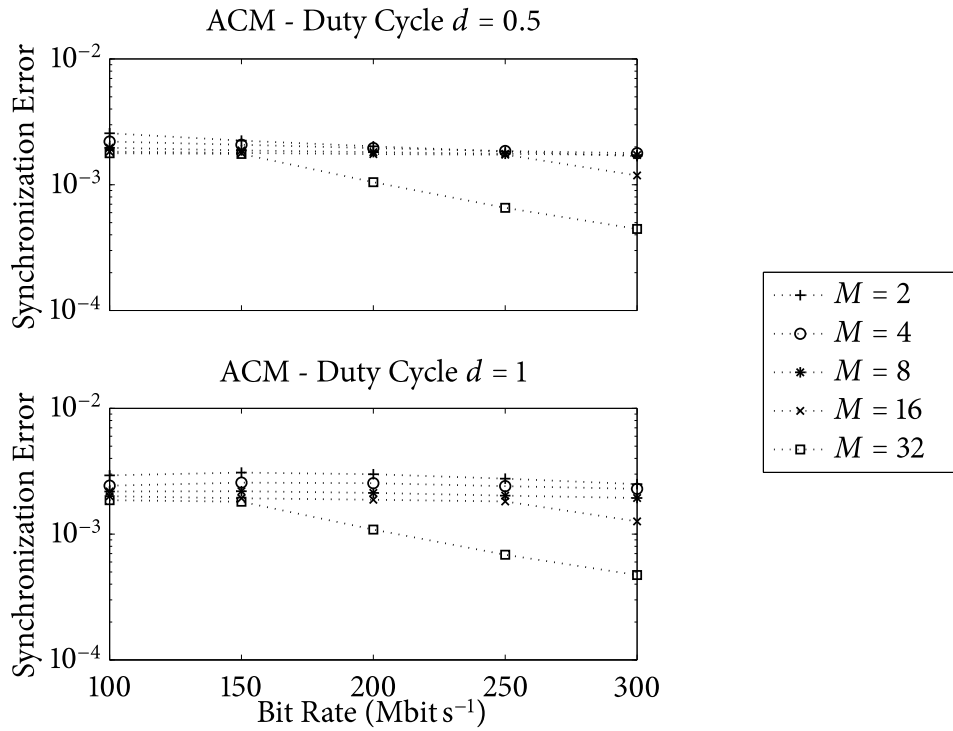


Figure 5.8: Synchronization error vs. bit rate for various PPM orders, ACM case.

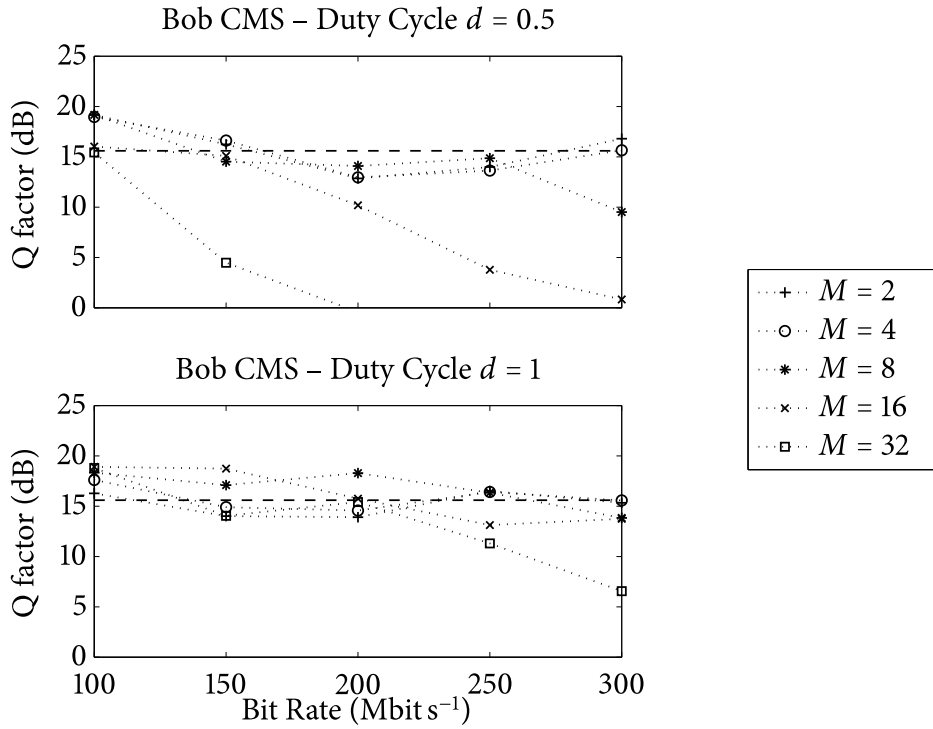


Figure 5.9: Q factor for Bob vs. bit rate for various PPM orders, CMS case.

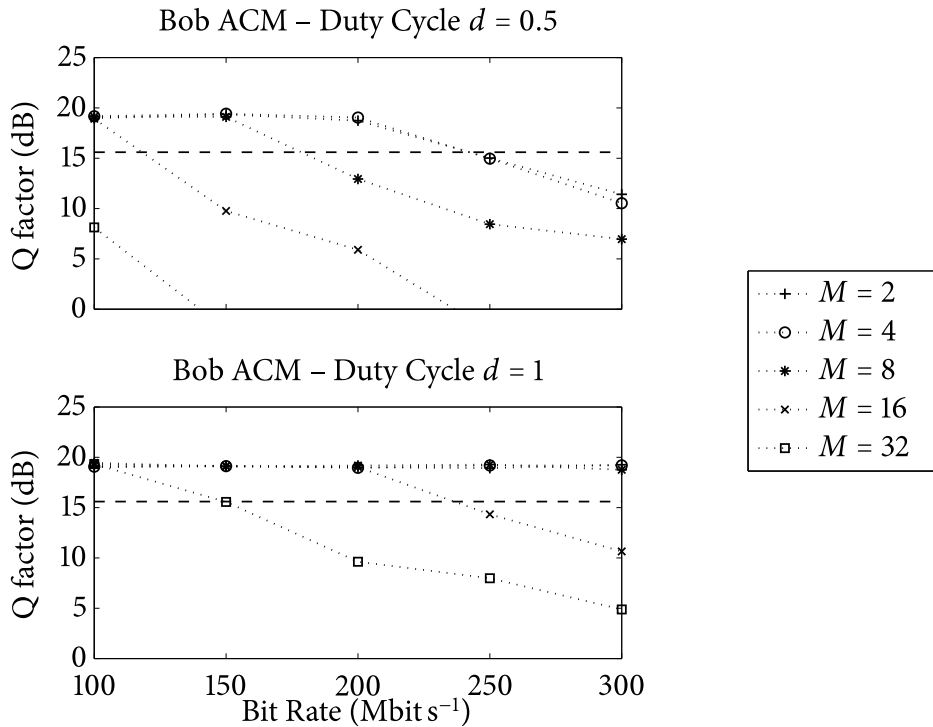


Figure 5.10: Q factor for Bob vs. bit rate for various PPM orders, ACM case.

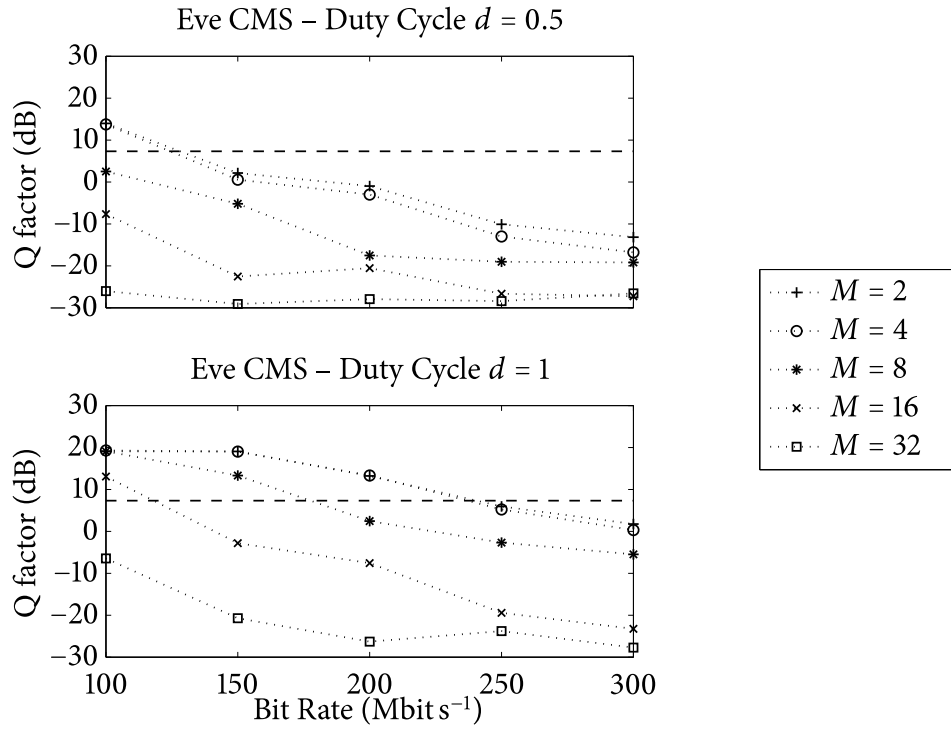


Figure 5.11: Q factor for Eve vs. bit rate for various PPM orders, CMS case.

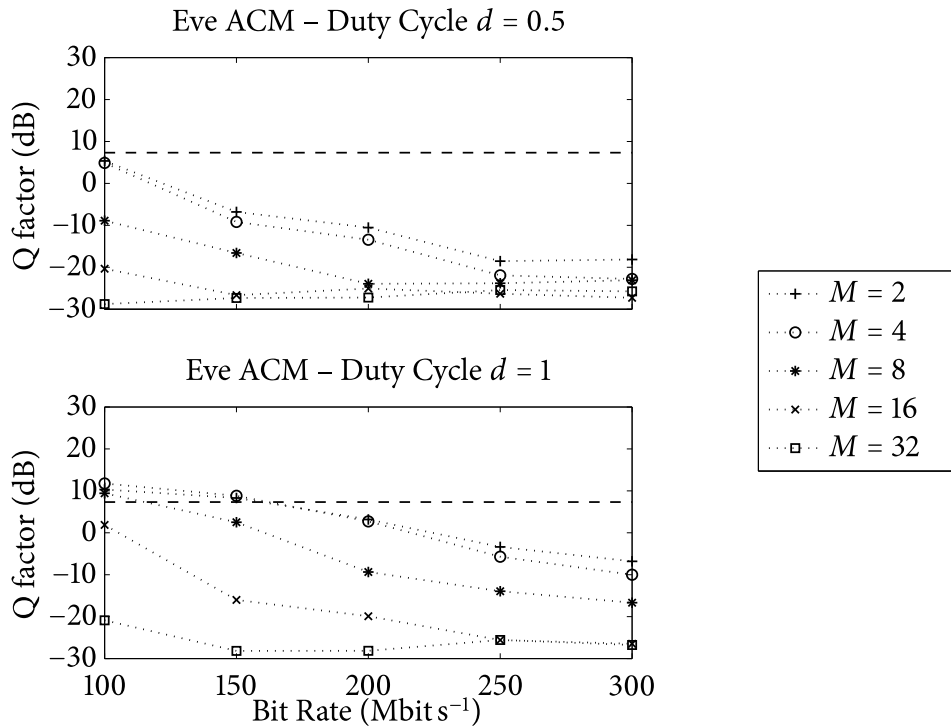


Figure 5.12: Q factor for Eve vs. bit rate for various PPM orders, ACM case.

5.5 Line of Sight Propagation

The main impairment to optical propagation in free-space environments is due to the free-space attenuation. The results presented in this section are obtained by considering only a direct LOS path between the transmitter and the receiver, *i.e.*, by neglecting all non-LOS contributions to the impulse response of the channel. Furthermore, it has been considered also the unrealistic case of an amplifying propagation, which permits to include the effect of the receiver preamplifier.

The synchronization error has acceptable values only within a narrow window of ± 0.5 dB around 0 dB, as shown in Fig. 5.13. Furthermore, the peak of the synchronization error is not exactly centered at 0 dB, but it is slightly shifted to smaller negative values. This can lead to the consideration that, at the receiver, the injection strength to the SL should be slightly lowered. However, in spite of the fact that the LOS attenuation has to be compensated, this peak shift can be ignored. In particular, in order to maintain the synchronization error within the synchronization window, the receiver must employ a variable amplifier, which, being an electronic amplifier (and not optical), it could be also made adaptive and controlled by the mean value of the receiver power or even by an estimation of the synchronization error measured after the difference block (where, however, there is also the presence of the message disturbing the estimation).

The Q factor measured by Bob, shown in Fig. 5.14, confirms the need of a good LOS compensation. Furthermore, the CMS scheme has a wider good range and fall down slowly compared to the ACM scheme. However, the ACM scheme, as in previous results, within its window is more stable and performs better than the CMS.

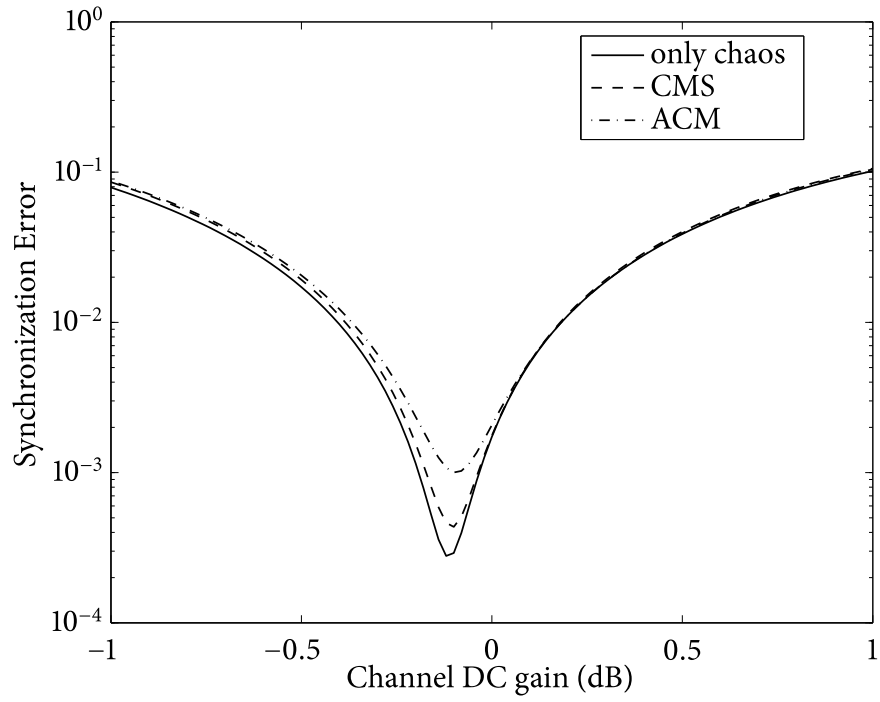


Figure 5.13: Synchronization error vs. LOS DC gain.

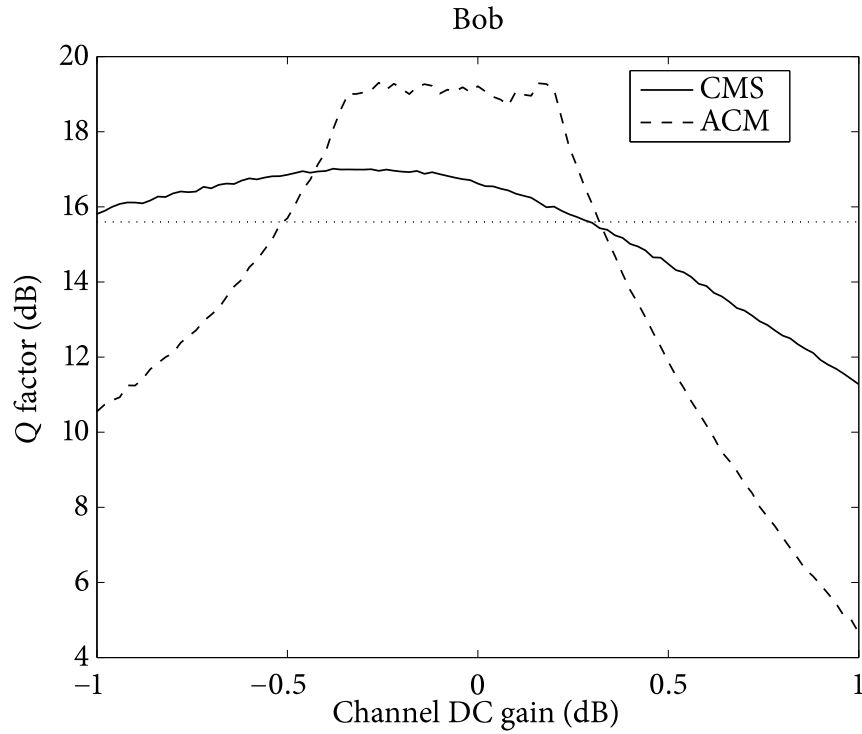


Figure 5.14: Q factor for Bob vs. LOS DC gain.

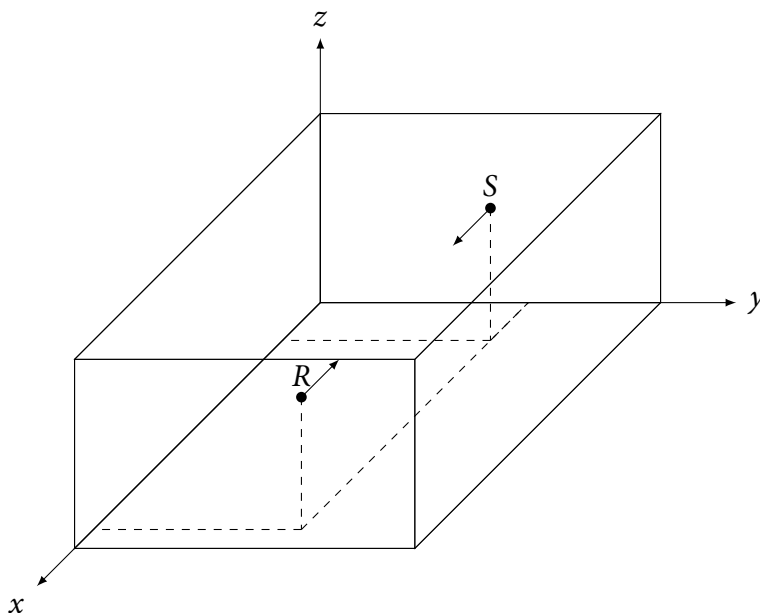


Figure 5.15: Sketch of the indoor environment used in simulations.

5.6 Multipath impairments

All wireless communication systems suffer of multipath impairments due to the reflective nature of real environments. This section considers an indoor propagation within the environment described by the parameters given in Table 4.2, and sketched in Fig. 5.15. In particular, the receiver has been chosen with a Lambertian pattern, *i.e.*, with $\Psi_{\text{FOV}} = 60$ deg. A receiver with such a large pattern collects many high order reflections, so this can be considered as a sort of worst case. In Fig. 5.16 the DC gain and the minimum delay of the channel are shown by varying the transmitter azimuthal angle. In particular, from the plot of the delay, it can be observed that the LOS path persists up to a rotation of more than 80 deg of the transmitter, but, as shown in the upper plot, at about 40 deg the LOS component is strongly attenuated and comparable with the non-LOS reflections (see Fig. 4.14). Just for reference, in Figs. 5.17 and 5.18 the DC gain is shown for a LOS propagation but by varying either the distance or the radiation pattern of the transmitter. More important is the graph in Fig. 5.19, which shows how the ratio of the LOS component to the non-LOS components varies by rotating the transmitter. This figure will serve in the following to understand the crucial role of the LOS path in reducing the distortion effects introduced by the non-LOS components.

In Figs. 5.20 to 5.22, the Q factor is shown as a function of the distance, transmitter radiation pattern and transmitter rotation. The free-space attenuation has already been compensated, *i.e.*, a variable gain amplifier is assumed at the receiver. The results are optimal, because in every investigated configuration there is always a sufficiently strong LOS path (in respect to the non-LOS reflections), and thus, these graphs are in accordance with the BTB choice made in Section 5.2 (see, for instance, Fig. 5.4 for $\zeta = 0.03$).

Worse performance occurs if the power of the LOS component decreases. In Figs. 5.23 and 5.24 the case of a transmitter with an HWHM of 5 deg is considered. As can be seen, after a rotation of more than 15 deg, the system performance drops down very fast. Finally,

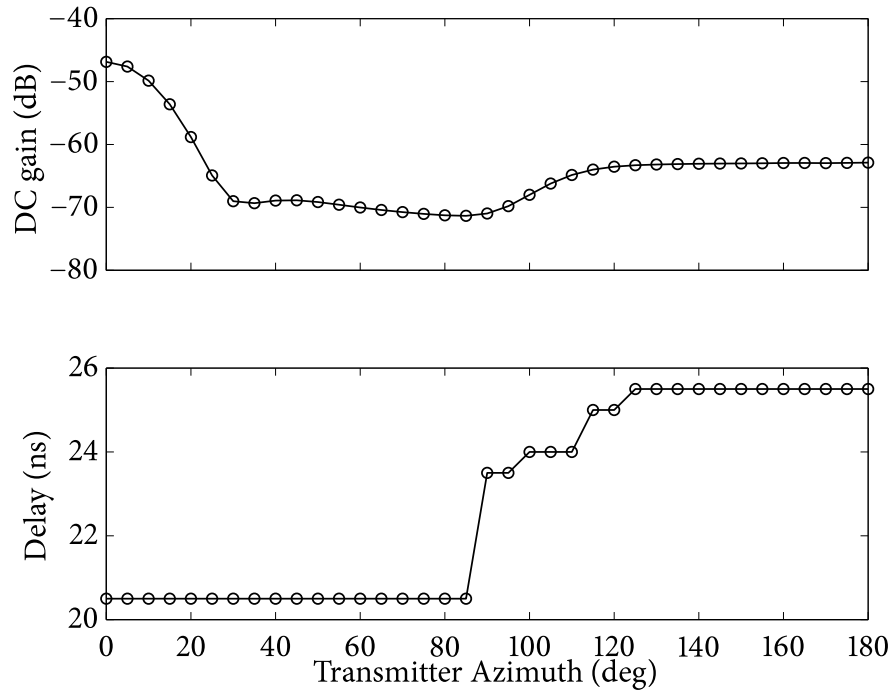


Figure 5.16: Channel DC gain and delay vs. transmitter azimuth.

Figs. 5.25 and 5.26 show what are the Q factor and the synchronization error for a given LOS to non-LOS ratio, or more usefully, what the LOS to non-LOS ratio must be to achieve a sufficient Q factor or synchronization error. In particular, in order to maintain good system performance, the ratio must be higher than 15 dB. The same analysis, for a bit rate of $R_{\text{bit}} = 250 \text{ Mbit s}^{-1}$ is shown in Fig. 5.27, and at least for the ACM scheme, it is quite satisfactory.

For instance, by sending a clear message, *i.e.*, without the chaotic steganographic process, the minimum LOS to non-LOS ratio about 0 dB, as shown in Fig. 5.28.¹ This is quite obvious: by considering, for instance, only one non-LOS reflection, a ratio of 0 dB means that the LOS and non-LOS components have the same power, and, thus, the non-LOS bounce will arrive after the LOS, possibly covering a different slot, and as the ratio decreases, this retarded slot has more power than the right one, degrading the detection. On the contrary, PPM is in fact very good in reflective environments, because even if the first non-LOS component has more power than the LOS, the receiver should synchronize on the non-LOS and the communication remains totally reliable. This is not possible in the steganographic system explored in this Thesis, because the PPM decoding is done after chaos synchronization, which is very sensible to impairments, as shown before.

¹In this figure, the slot synchronization is assumed to happen on the LOS slot, even if it is not present.

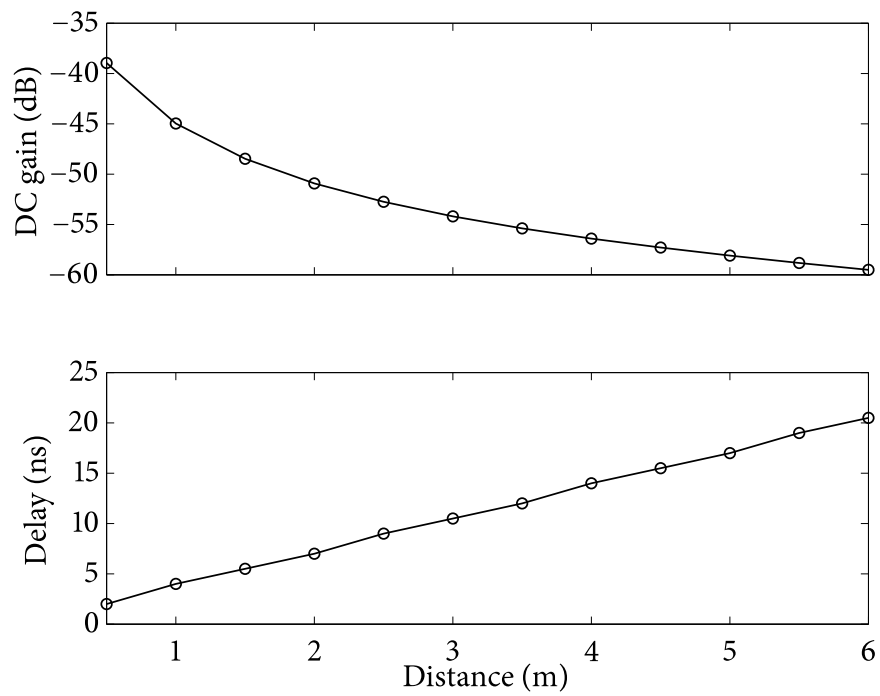


Figure 5.17: Channel DC gain and delay vs. distance.

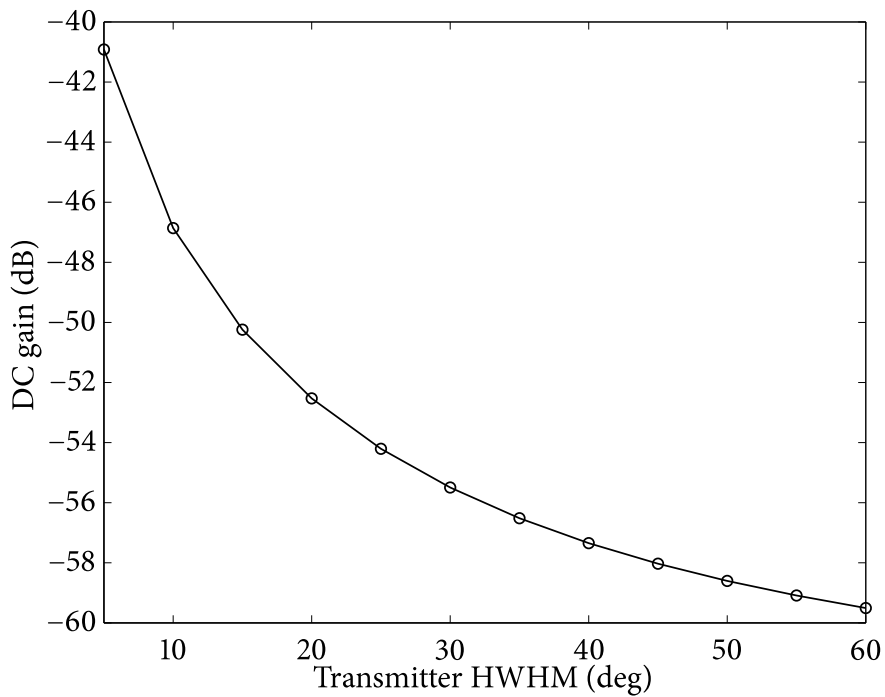


Figure 5.18: Channel DC gain and delay vs. transmitter HWHM.

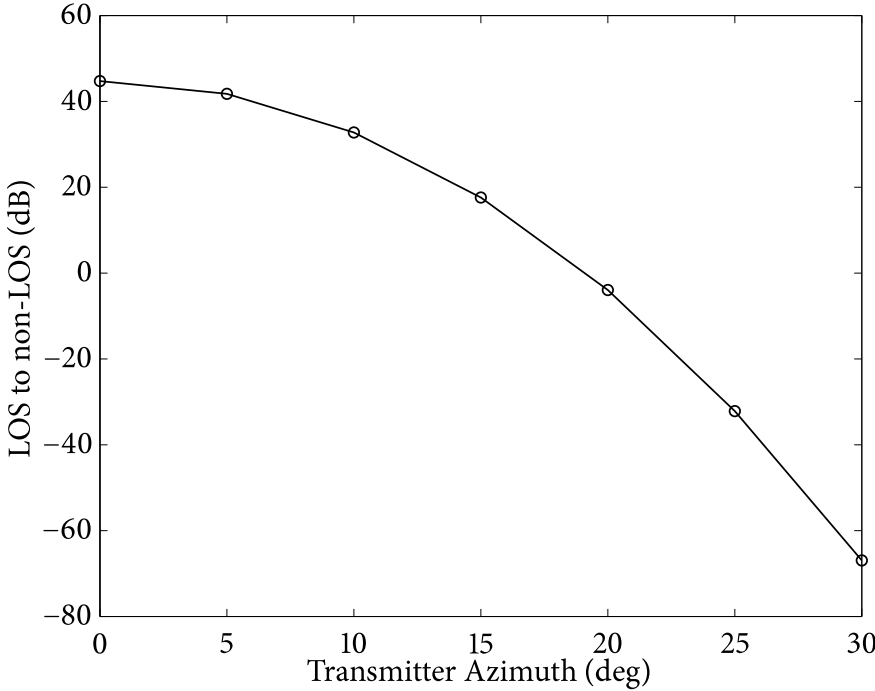


Figure 5.19: Channel LOS to non-LOS ratio vs. transmitter azimuth.

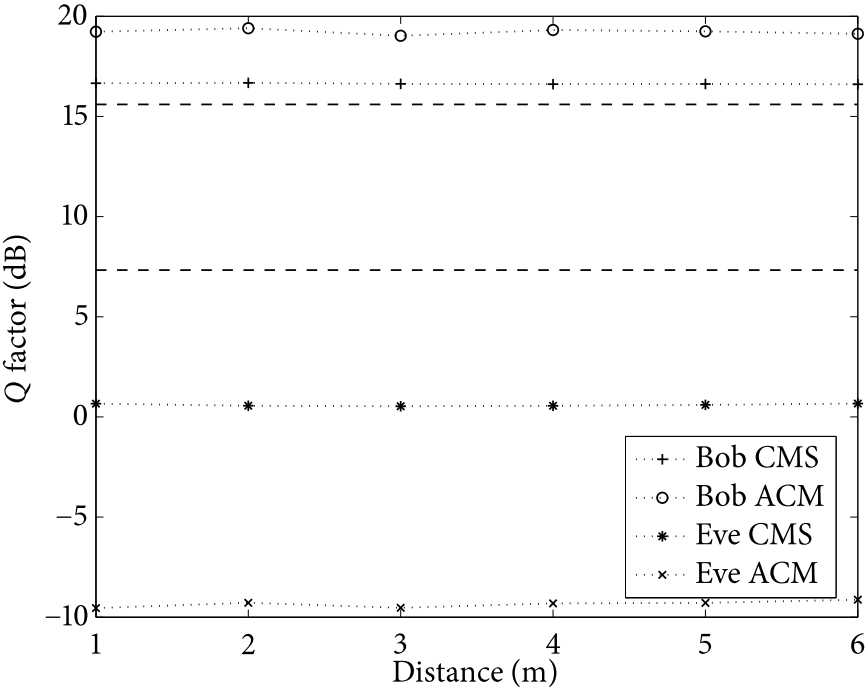


Figure 5.20: Indoor Q factor vs. distance.

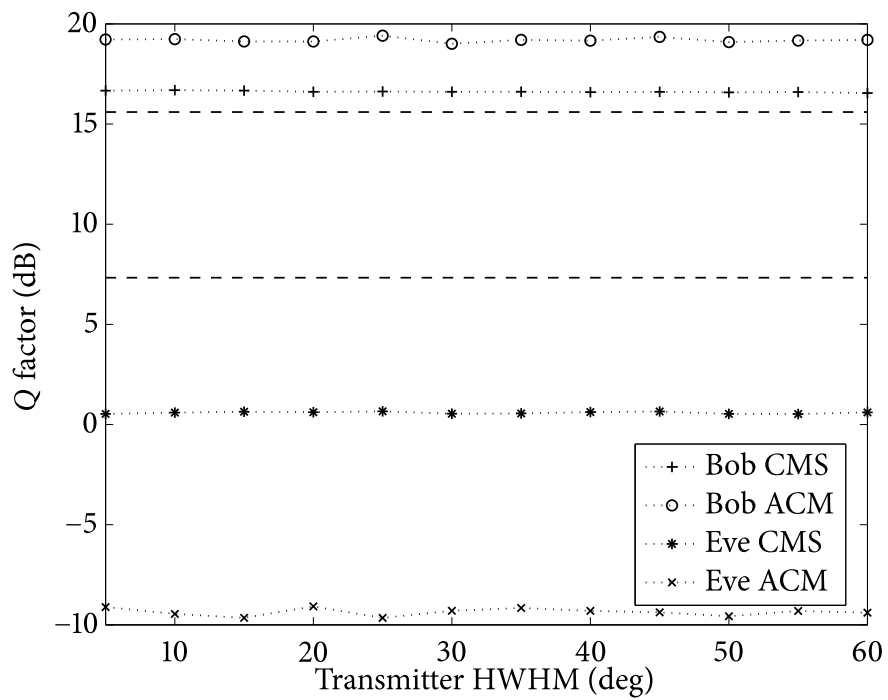


Figure 5.21: Indoor Q factor vs. transmitter HWHM.

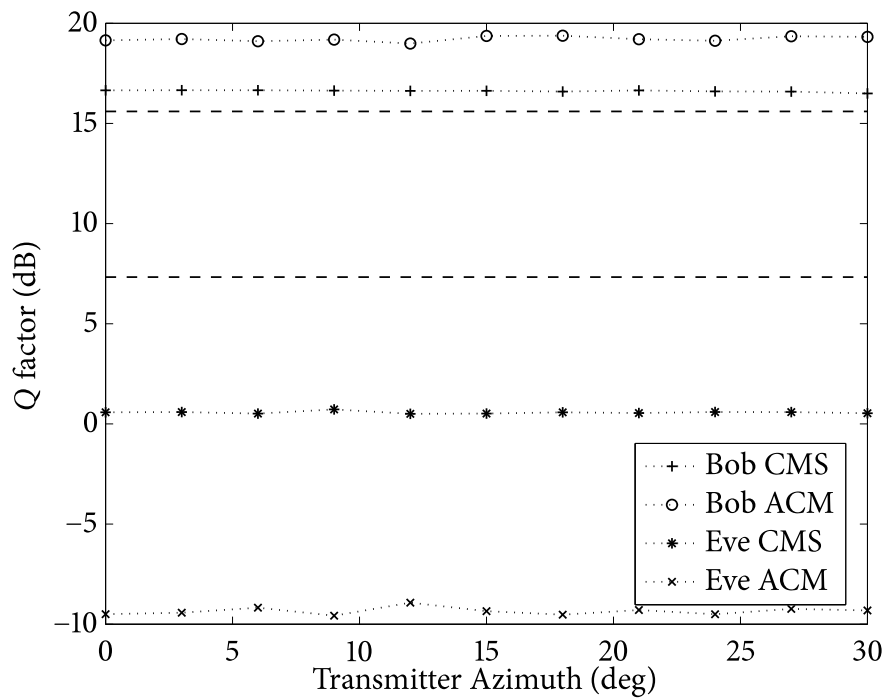


Figure 5.22: Indoor Q factor vs. transmitter azimuth.

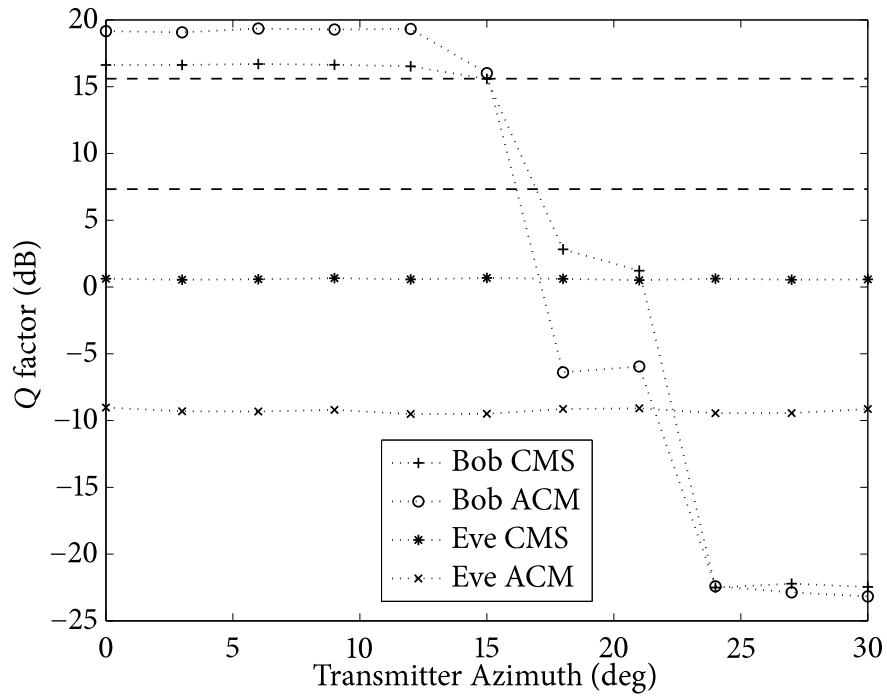


Figure 5.23: Indoor Q factor vs. transmitter azimuth, with a transmitter HWHM of 5 deg.

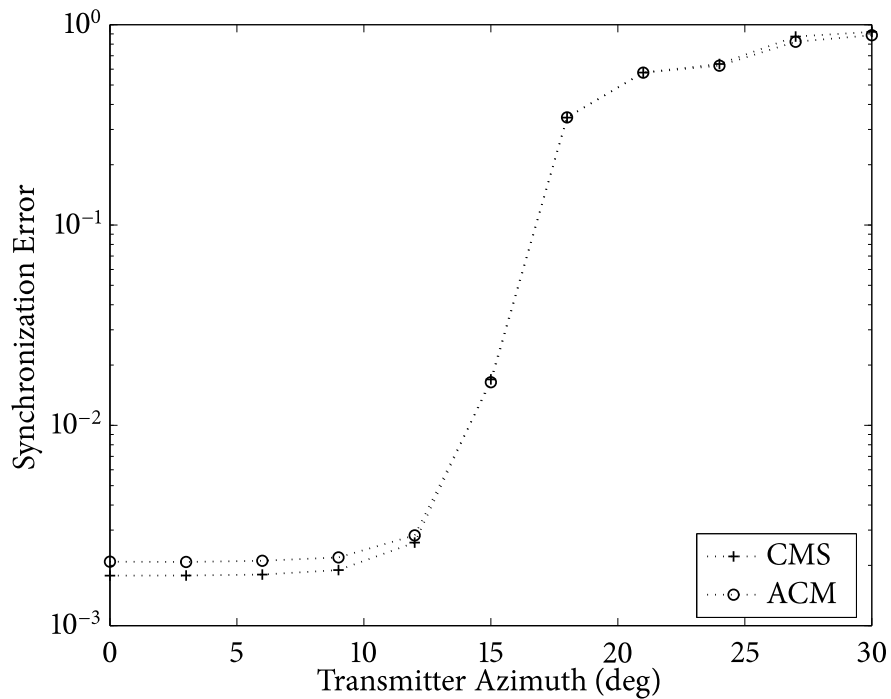


Figure 5.24: Indoor synchronization error vs. transmitter azimuth, with a transmitter HWHM of 5 deg.

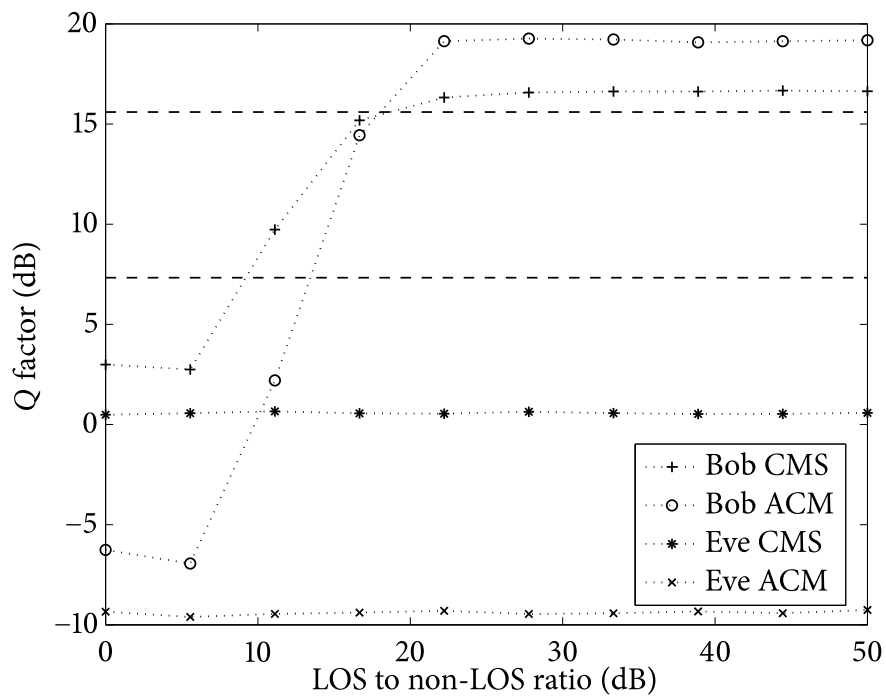


Figure 5.25: Indoor Q factor vs. LOS to non-LOS ratio.

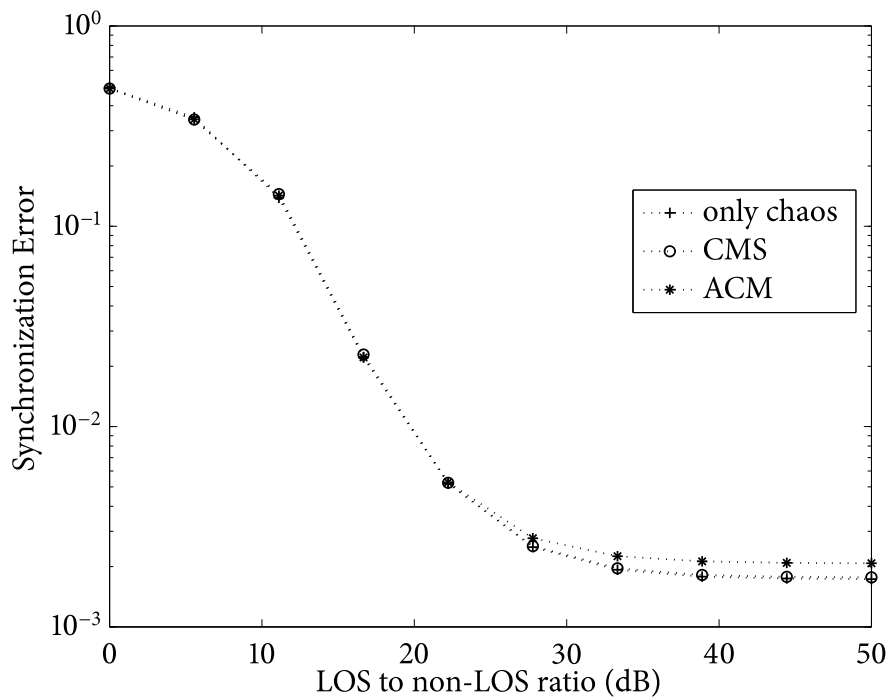


Figure 5.26: Indoor synchronization error vs. LOS to non-LOS ratio.

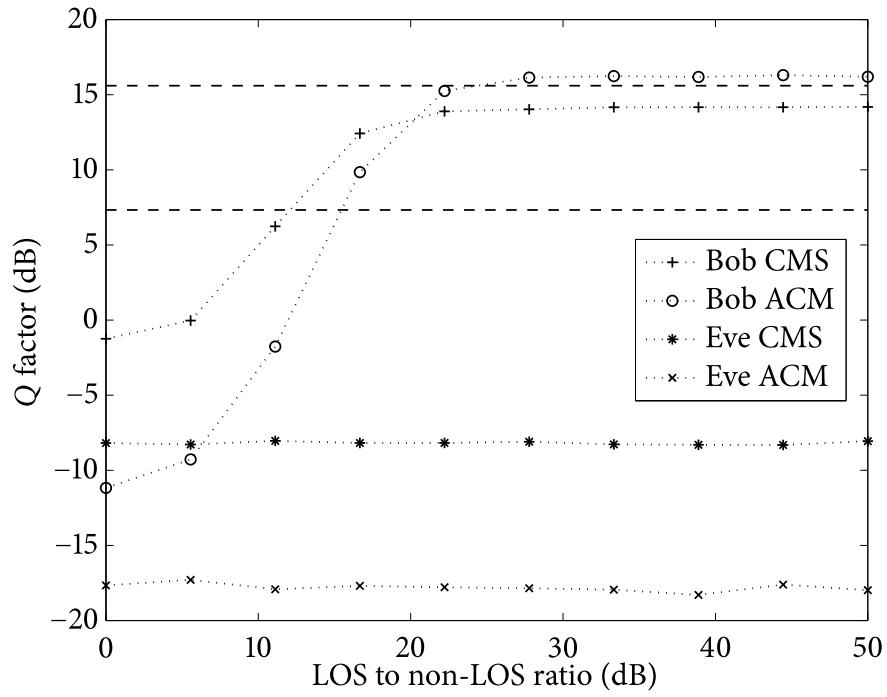


Figure 5.27: Indoor Q factor vs. LOS to non-LOS ratio, for a bit rate of $R_{\text{bit}} = 250 \text{ Mbit s}^{-1}$.

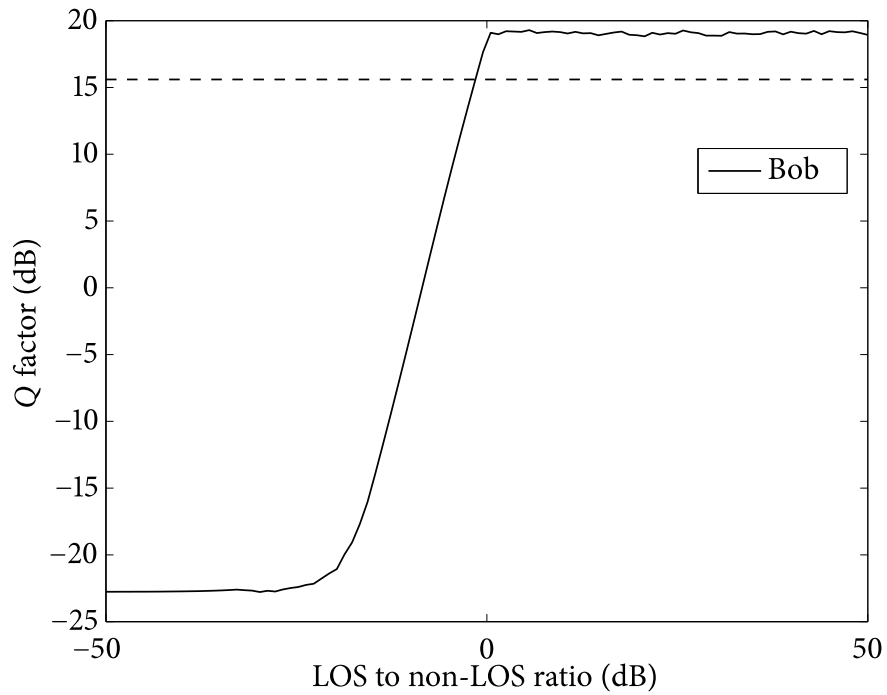


Figure 5.28: Indoor Q factor vs. LOS to non-LOS ratio, by only considering an unmasked message propagation.

Conclusions

The aim of this Thesis has been to study an optical free-space communication system, employing a chaotic carrier, generated by a semiconductor laser with optoelectronic delayed feedback, to obtain the steganography of an information message. At the receiver, a semiconductor laser, similar to that at the transmitter, is used to recreate the chaotic carrier by chaos synchronization and to recover the message by a difference and an appropriate filtering.

The system has been analyzed numerically for different configurations, and its performance evaluated by measuring the synchronization error and the Q factor at two different points: at the receiver to quantify the quality of message recovery, and after the transmitter to quantify the quality of message masking.

A set of BTB simulations has provided information about the maximum performance achievable for a given configuration, and has permitted to extrapolate a good starting point to search optimal values of key parameters, such as the modulation depth ζ and the bit rate R_{bit} .

Next, an analysis of LOS propagation has shown the need of employing a variable gain amplifier stage, at the receiver, to compensate the free-space attenuation.

Finally, the propagation in a closed indoor environment has been considered, where the optical power undergoes multiple reflections in its path between the transmitter and the receiver, with a consequent degradation in the quality of the recovered message. This multipath impairments can be reduced only by achieving a sufficiently high LOS to non-LOS ratio, found to be in the order of 20 dB for the considered environment.

Appendix **A**

Numeric Integration Scheme

Knowing the equations and knowing the solution are two different things. Far, far away.

Tsung-Dao Lee (1926 –)

A.1 Heun's Method

The Heun's method [40] (also called the modified Euler's method [41] or the explicit trapezoidal rule [42]) is a numerical procedure to solve initial value problems (IVPs) within ordinary differential equations (ODEs). It can be seen as an extension of the Euler's method into a two-stage second-order Runge-Kutta method.

In order to solve the following IVP:

$$\frac{dx(t)}{dt} = q(t, x(t)) \quad (\text{A.1a})$$

$$x(t_0) = x_0, \quad (\text{A.1b})$$

the Euler's method defines the predictor for the step h as:

$$x(t+h) = x(t) + hq(t, x(t)), \quad (\text{A.2})$$

which is modified into the following implicit equation:

$$x(t+h) = x(t) + \frac{h}{2}[q(t, x(t)) + q(t+h, x(t+h))]. \quad (\text{A.3})$$

To make it explicit the term $x(t+h)$ on the right hand side can be replaced by the Euler's predictor given in Eq. (A.2) to obtain:

$$x(t+h) = x(t) + \frac{h}{2}[q(t, x(t)) + q(t+h, x(t) + hq(t, x(t)))], \quad (\text{A.4})$$

which is usually rewritten as:

$$k = hq(t, x(t)) \quad (\text{A.5a})$$

$$x(t+h) = x(t) + \frac{h}{2}[q(t, x(t)) + q(t+h, x(t) + k)]. \quad (\text{A.5b})$$

A.2 Stochastic Differential Equations

The stochastic differential equation (SDE) with white noise, also known as a Langevin's equation, is:

$$\frac{dx(t)}{dt} = q(t, x(t) + g(t, x(t)))\xi(t), \quad (\text{A.6})$$

where $\xi(t)$ is a Gaussian stochastic process satisfying:

$$E[\xi(t)] = 0 \quad (\text{A.7a})$$

$$E[\xi(t)\xi(s)] = \delta(t-s), \quad (\text{A.7b})$$

with $\delta(t)$ being the delta function:

$$\delta(t) = \begin{cases} 1 & t = 0 \\ 0 & t \neq 0. \end{cases} \quad (\text{A.8})$$

It can be shown that the optimal Heun's method required to solve Eq. (A.6) is given by [43]:

$$k = hq(t, x(t)) \quad (\text{A.9a})$$

$$l = \sqrt{h}u(t)g(t, x(t)) \quad (\text{A.9b})$$

$$x(t+h) = x(t) + \frac{h}{2}[q(t, x(t)) + q(t+h, x(t) + k + l)] \\ + \frac{\sqrt{h}}{2}u(t)[g(t, x(t)) + g(t+h, x(t) + k + l)], \quad (\text{A.9c})$$

where $u(t)$ is a Gaussian random variable with zero mean and unitary variance:

$$E[u] = 0 \quad (\text{A.10a})$$

$$E[u^2] = 1. \quad (\text{A.10b})$$

This scheme, called the stochastic Heun's scheme (SHS), can be extended to the case of a system of n Langevin's equations [44]:

$$\frac{dx_i(t)}{dt} = q_i(t, \mathbf{x}(t) + \sum_k g_{ik}(t, \mathbf{x}(t)))\xi_k(t), \quad (\text{A.11})$$

where $\mathbf{x} = (x_1, \dots, x_n)$ are the dynamical variables of the system, and the noise sources $\xi_k(t)$ are Gaussian stochastic processes satisfying:

$$E[\xi_k(t)] = 0 \quad (\text{A.12a})$$

$$E[\xi_k(t)\xi_l(s)] = \delta_{kl}\delta(t-s), \quad (\text{A.12b})$$

with δ_{kl} being the Kronecker's delta function:

$$\delta_{kl} = \begin{cases} 1 & k = l \\ 0 & k \neq l. \end{cases} \quad (\text{A.13})$$

In the particular case of diagonal noise, *i.e.*, if $g_{ik} = 0, \quad \forall i \neq k$:

$$\frac{dx_i(t)}{dt} = q_i(t, \mathbf{x}(t) + g_i(t, \mathbf{x}(t))) \xi_i(t), \quad (\text{A.14})$$

the Heun's scheme becomes:

$$k_i = hq(t, \mathbf{x}(t)) \quad (\text{A.15a})$$

$$l_i = \sqrt{h}u_i(t)g_i(t, \mathbf{x}(t)) \quad (\text{A.15b})$$

$$\begin{aligned} x_i(t+h) = x_i(t) + \frac{h}{2} [q_i(t, \mathbf{x}(t)) + q_i(t+h, \mathbf{x}(t) + k_i + l_i)] \\ + \frac{\sqrt{h}}{2} u(t) [g_i(t, \mathbf{x}(t)) + g_i(t+h, \mathbf{x}(t) + k_i + l_i)]. \end{aligned} \quad (\text{A.15c})$$

This method has been used to integrate the dynamical equations of chaotic lasers given in Section 3.3.1.

Appendix B

Photodetection

A theory has only the alternative of being right or wrong. A model has a third possibility: it may be right, but irrelevant.

Manfred Eigen (1927 –)

Photodetectors are used to convert a light signal into an electrical signal, such as a voltage or a current.

In photodiodes, this conversion is typically achieved by the creation of electron-hole pairs (EHPs) by the absorption of photons. There are two types of low-cost and widely available photodiodes: ordinary positive-intrinsic-negative (p-i-n) photodiodes and avalanche photodiodes (APDs) [33, 45].

An APD is essentially a p-i-n photodiode that is operated at very high reverse bias, resulting in internal gain caused by the avalanche effect. APDs are favored in optical receivers only in situations where the external noise induced by ambient light is low. Presently, the majority of commercial infrared links use ordinary p-i-n photodiodes [33].

B.1 Photodiodes

Fig. B.2 shows a schematic of the equivalent circuit of the photodiode in Fig. B.1. The ideal current source models the internal photocurrent I_0 generated by the photodetection process. The current I_0 has a simple linear relation with the incident optical power P_{inc} :

$$I_0 = RP_{\text{inc}}, \quad (\text{B.1})$$

where R (A W^{-1}) is the photodiode responsivity. The responsivity R is related to the quantum efficiency η of the photodiode by the relation

$$R = \eta \frac{e}{h\nu}. \quad (\text{B.2})$$

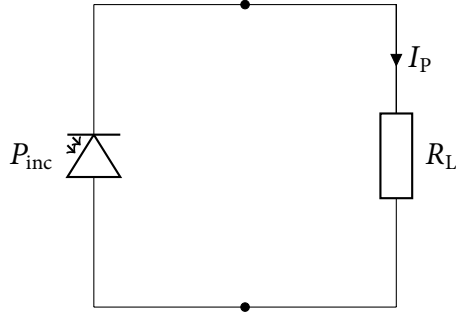


Figure B.1: Scheme of a photodiode connection.

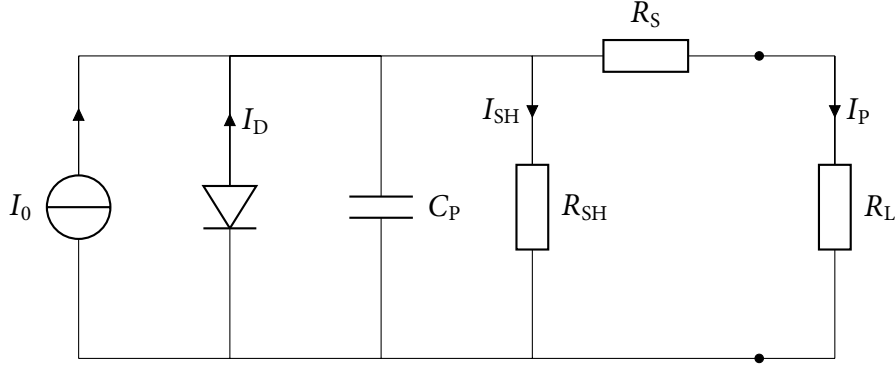


Figure B.2: Schematic of the equivalent circuit of a photodiode.

Eq. (B.2) clearly shows the dependence of the responsivity R on the frequency ν , and it has to be remarked that the quantum efficiency η is also frequency dependent. Fortunately, the responsivity R results constant over the typical frequency bandwidth emitted by a single-mode semiconductor laser. A typical value of the responsivity R for a p-i-n photodiode operating at the wavelength of 1550 nm is:

$$R(\lambda = 1550 \text{ nm}) = 0.95 \text{ A W}^{-1}. \quad (\text{B.3})$$

The ideal diode in Fig. B.2 represents the internal junction of the photodiode, which is responsible of creating the dark current I_D , present even in absence of incident optical power. Usually photodiodes are operated in reverse bias, so the dark current I_D is the reverse saturation current of the junction. A typical value of the dark current is $I_D = 20 \text{ nA}$.

The capacitance C_P is the junction parasitic capacitance. Its value depends mainly on the detector area and on the bias current, in particular it increases approximately linearly with the detector area, and decreases with increasing reverse bias.

The shunt resistance R_{SH} is the leakage resistance of the diode and it has a direct impact on the dark current I_D .

The series resistance R_S takes into account for all other parasitic resistances: the bulk resistance of the photodiode substrate, the ohmic contact diffusions and the resistances of the leads. In normal detection operations the series resistance R_S has a very low impact on the detection performances.

The total current I_P delivered to the load is then:

$$I_P = I_0 + I_D - I_{SH} = RP_{inc} + I_D - I_{SH}, \quad (\text{B.4})$$

where I_{SH} is the current flowing into the shunt resistance R_{SH} .

B.1.1 Noise in Photodiodes

The total noise characteristic of a photodiode comes mainly from two contributions: the shot noise and the thermal noise.

Shot Noise

The shot noise is related to the uncertainty in determining the magnitude of a current due to its fluctuations around its local mean value.

Shot noise can be described as a white noise with a constant power spectral density (PSD) given by [37, 45]:

$$S_{\text{shot}}(f) = eI_P. \quad (\text{B.5})$$

Indeed, being B_{ph} the bandwidth, the variance of the shot noise current is:

$$\sigma_{\text{shot}}^2 = \int_{-B_{\text{ph}}}^{+B_{\text{ph}}} S_{\text{shot}}(f) df = 2eI_P B_{\text{ph}}. \quad (\text{B.6})$$

Thermal Noise

The thermal noise (also known as Johnson-Nyquist's noise [46, 47]) is a phenomenon associated with Brownian's motion of electrons in a conductor. Indeed, it is present in all resistors at a temperature above absolute zero, even when no external current is flowing.

The thermal noise of a conductor of resistance R can be modeled as a noise current generator in parallel with a noiseless resistance R . For frequencies strongly below the visible range, the thermal noise current is white with a PSD given by [37, 48]:

$$S_{\text{thermal}}(f) = \frac{2kT}{R}, \quad \text{for } f \ll \frac{kT}{h}, \quad (\text{B.7})$$

where $k = 1.38 \times 10^{-23} \text{ J K}^{-1}$ is the Boltzmann's constant, $h = 6.626 \times 10^{-34} \text{ J s}$ is the Planck's constant, and T (K) is the temperature. The thermal noise current can be modeled as a Gaussian distribution with zero mean and variance:

$$\sigma_{\text{thermal}}^2 = \int_{-B_{\text{ph}}}^{+B_{\text{ph}}} S_{\text{thermal}}(f) df = \frac{4kTB_{\text{ph}}}{R}. \quad (\text{B.8})$$

Total Noise

The total noise is the sum of the shot and thermal noises, and it can be described as a white noise with a PSD of:

$$\begin{aligned} S_{\text{total}}(f) &= S_{\text{shot}}(f) + S_{\text{thermal}}(f) \\ &= eI_P + \frac{2kT}{R}, \end{aligned} \quad (\text{B.9})$$

and, thus, it can be modeled as a Gaussian distribution with zero mean and variance:

$$\begin{aligned} \sigma_{\text{total}}^2 &= \sigma_{\text{shot}}^2 + \sigma_{\text{thermal}}^2 \\ &= 2eI_P B_{\text{ph}} + \frac{4kTB_{\text{ph}}}{R_{\text{eq}}}, \end{aligned} \quad (\text{B.10})$$

where R_{eq} is the total equivalent shunt resistance.

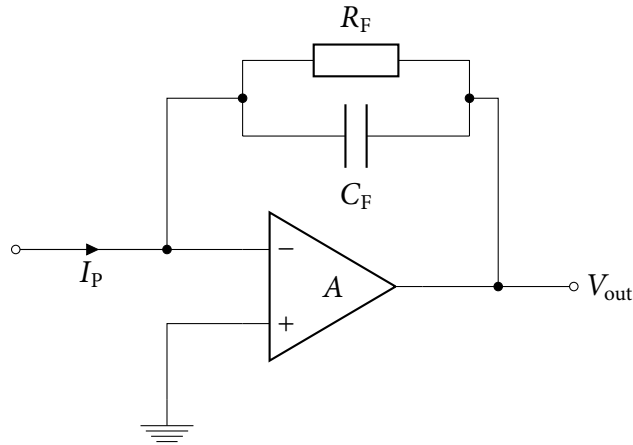


Figure B.3: Schematic of a transimpedance amplifier.

B.2 Preamplifiers

For infrared link applications, one of the most commonly used preamplifier stage used is the trans-impedance amplifier (TIA) (see Fig. B.3), which transforms the current I_p , injected by the photodiode, into a voltage signal, while guaranteeing a large dynamic range and a wide bandwidth, without the need for equalization [33].

B.2.1 Noise in Preamplifiers

In addition to shot and thermal noises induced by the feedback resistor R_F , the total noise of an amplifier circuit depends on the amplifier itself, and it is a function of the amplifier design: three common designs for amplifiers are bipolar, JFET-input, and CMOS-input. While each design can provide low-noise performance, their performances are not equal. Usually, amplifier specifications comes with a total input-referred noise current that take into account the specific amplifier structure.

References

- [1] L. M. Pecora and T. L. Carroll, "Synchronization in chaotic systems," *Phys. Rev. Lett.*, vol. 64, no. 8, pp. 821–824, Feb 1990.
- [2] D. Kanakidis, A. Argyris, and D. Syvridis, "Performance characterization of high-bit-rate optical chaotic communication systems in a back-to-back configuration," *Lightwave Technology, Journal of*, vol. 21, no. 3, pp. 750 – 758, march 2003.
- [3] D. Kanakidis, A. Bogris, A. Argyris, and D. Syvridis, "Numerical investigation of fiber transmission of a chaotic encrypted message using dispersion compensation schemes," *Lightwave Technology, Journal of*, vol. 22, no. 10, pp. 2256 – 2263, oct. 2004.
- [4] A. Argyris, D. Syvridis, L. Larger, V. Annovazzi-Lodi, P. Colet, I. Fischer, J. Garcia-Ojalvo, C. R. Mirasso, L. Pesquera, and K. A. Shore, "Chaos-based communications at high bit rates using commercial fibre-optic links," *Nature*, vol. 438, pp. 343 – 346, 2005.
- [5] D. Kanakidis, A. Argyris, A. Bogris, and D. Syvridis, "Influence of the decoding process on the performance of chaos encrypted optical communication systems," *Lightwave Technology, Journal of*, vol. 24, no. 1, pp. 335 – 341, jan. 2006.
- [6] L. Ursini, M. Santagiustina, and V. Annovazzi-Lodi, "Enhancing chaotic communication performances by manchester coding," *Photonics Technology Letters, IEEE*, vol. 20, no. 6, pp. 401 –403, march15, 2008.
- [7] C. Antonelli, A. Mecozzi, M. Santagiustina, and L. Ursini, "Impairments due to polarization-mode dispersion in chaos-encrypted communication systems," *Photonics Technology Letters, IEEE*, vol. 21, no. 19, pp. 1387 –1389, oct.1, 2009.
- [8] O. Bader and H. Lui, "Laser safety and the eye: Hidden hazards and practical pearls," Feb 1996. [Online]. Available: <http://www.dermatology.org/laser/eyesafety.html>
- [9] G. Longhi, "Sistemi di comunicazione ottica in spazio libero," Tesi di laurea triennale, 2007.
- [10] A. Yariv, *Optical Electronics in Modern Communications (Oxford Series in Electrical & Computer Engineering)*, 5th ed. Oxford University Press Inc, USA, April 1997.
- [11] K. Petermann, *Laser Diode Modulation and Noise*. KTK Scientific Publishers / Tokyo, 1988.

- [12] J. Ohtsubo, *Semiconductor Lasers: Stability, Instability and Chaos*, 2nd ed. Springer, 2008.
- [13] C. G. Someda, *Electromagnetic Waves*, 2nd ed. CRC Press, 2006.
- [14] O. Svelto and D. C. Hanna, *Principles of Lasers*, 4th ed. Springer, 1998.
- [15] D. M. Pozar, *Microwave Engineering*, 3rd ed. Wiley, 2004.
- [16] J. van der Ziel and R. Logan, "Dispersion of the group velocity refractive index in GaAs double heterostructure lasers," *Quantum Electronics, IEEE Journal of*, vol. 19, no. 2, pp. 164–169, Feb 1983.
- [17] M. A. Parker, *Physics of optoelectronics*. CRC Press, 2005.
- [18] D. Botez, "Analytical approximation of the radiation confinement factor for the TE₀ mode of a double heterojunction laser," *Quantum Electronics, IEEE Journal of*, vol. 14, no. 4, pp. 230–232, Apr 1978.
- [19] C. Henry, "Theory of the linewidth of semiconductor lasers," *Quantum Electronics, IEEE Journal of*, vol. 18, no. 2, pp. 259–264, Feb 1982.
- [20] E. N. Lorenz, "Deterministic nonperiodic flow," *Journal of the Atmospheric Sciences*, vol. 20, no. 2, pp. 130–141, 3 1963.
- [21] L. M. Pecora, T. L. Carroll, G. A. Johnson, D. J. Mar, and J. F. Heagy, "Fundamentals of synchronization in chaotic systems, concepts, and applications," *Chaos: An Interdisciplinary Journal of Nonlinear Science*, vol. 7, no. 4, pp. 520–543, 1997. [Online]. Available: <http://link.aip.org/link/?CHA/7/520/1>
- [22] L. Kocarev and U. Parlitz, "General approach for chaotic synchronization with applications to communication," *Phys. Rev. Lett.*, vol. 74, no. 25, pp. 5028–5031, Jun 1995.
- [23] J. P. Eckmann and D. Ruelle, "Ergodic theory of chaos and strange attractors," *Rev. Mod. Phys.*, vol. 57, no. 3, pp. 617–656, Jul 1985.
- [24] J. Mork, B. Tromborg, and J. Mark, "Chaos in semiconductor lasers with optical feedback: theory and experiment," *Quantum Electronics, IEEE Journal of*, vol. 28, no. 1, pp. 93 –108, jan 1992.
- [25] V. Annovazzi-Lodi, A. Scire, M. Sorel, and S. Donati, "Dynamic behavior and locking of a semiconductor laser subjected to external injection," *Quantum Electronics, IEEE Journal of*, vol. 34, no. 12, pp. 2350 –2357, dec 1998.
- [26] R. Lang and K. Kobayashi, "External optical feedback effects on semiconductor injection laser properties," *Quantum Electronics, IEEE Journal of*, vol. 16, no. 3, pp. 347 – 355, mar 1980.
- [27] L. Ursini, "Optical chaotic transmission systems for secure data communication," Ph.D. dissertation, Univerità degli Studi di Padova, Dipartimento di Ingegneria dell'Informazione, January 2009.

- [28] S. Tang and J. Liu, "Chaotic pulsing and quasi-periodic route to chaos in a semiconductor laser with delayed opto-electronic feedback," *Quantum Electronics, IEEE Journal of*, vol. 37, no. 3, pp. 329–336, Mar 2001.
- [29] J. Liu, H. Chen, and S. Tang, "Optical-communication systems based on chaos in semiconductor lasers," *Circuits and Systems I: Fundamental Theory and Applications, IEEE Transactions on*, vol. 48, no. 12, pp. 1475–1483, Dec. 2001.
- [30] F. yi Lin and J.-M. Liu, "Nonlinear dynamics of a semiconductor laser with delayed negative optoelectronic feedback," *Quantum Electronics, IEEE Journal of*, vol. 39, no. 4, pp. 562–568, Apr 2003.
- [31] H. Abarbanel, M. Kennel, L. Illing, S. Tang, H. Chen, and J. Liu, "Synchronization and communication using semiconductor lasers with optoelectronic feedback," *Quantum Electronics, IEEE Journal of*, vol. 37, no. 10, pp. 1301–1311, Oct 2001.
- [32] R. Otte, L. De Jong, and A. Van Roermund, "Slot synchronization by reducing the ppm pulsewidth in wireless optical systems," *Circuits and Systems II: Analog and Digital Signal Processing, IEEE Transactions on*, vol. 45, no. 7, pp. 901–903, Jul 1998.
- [33] J. Kahn and J. Barry, "Wireless infrared communications," *Proceedings of the IEEE*, vol. 85, no. 2, pp. 265–298, Feb 1997.
- [34] J. Carruthers and P. Kannan, "Iterative site-based modeling for wireless infrared channels," *Antennas and Propagation, IEEE Transactions on*, vol. 50, no. 5, pp. 759–765, May 2002.
- [35] J. Carruthers, S. Carroll, and P. Kannan, "Propagation modelling for indoor optical wireless communications using fast multi-receiver channel estimation," *Optoelectronics, IEE Proceedings -*, vol. 150, no. 5, pp. 473–481, Oct. 2003.
- [36] F. Gfeller and U. Bapst, "Wireless in-house data communication via diffuse infrared radiation," *Proceedings of the IEEE*, vol. 67, no. 11, pp. 1474 – 1486, nov. 1979.
- [37] N. Benvenuto and G. Cherubini, *Algorithms for Communications Systems and their Applications*. Wiley, January 2005.
- [38] F. Matera and M. Settembre, "Role of q-factor and of time jitter in the performance evaluation of optically amplified transmission systems," *Selected Topics in Quantum Electronics, IEEE Journal of*, vol. 6, no. 2, pp. 308–316, Mar/Apr 2000.
- [39] M. C. Jeruchim, P. Balaban, and K. S. Shanmugan, *Simulation of communication systems: modeling, methodology, and techniques*, 2nd ed. Springer, 2000.
- [40] J. C. Butcher, *Numerical methods for ordinary differential equations*, 2nd ed. John Wiley and Sons, 2008.
- [41] H. A. Koenig, *Modern computational methods*, ser. Series in computational and physical processes in mechanics and thermal sciences. Taylor & Francis, 1998.

- [42] U. M. Ascher and L. R. Petzold, *Computer methods for ordinary differential equations and differential-algebraic equations*, ser. Miscellaneous Titles in Applied Mathematics Series. SIAM, 1998, vol. Volume 61.
- [43] M. San Miguel and R. Toral, “Stochastic effects in physical systems,” in *Instabilities and Nonequilibrium Structures VI*, ser. Nonlinear phenomena and complex systems, E. Tirapegui, J. Martínez, and R. Tiemann, Eds. Kluwer Academic Publishers, 2000, vol. Volume 5.
- [44] J. L. García-Palacios and F. J. Lázaro, “Langevin-dynamics study of the dynamical properties of small magnetic particles,” *Phys. Rev. B*, vol. 58, no. 22, pp. 14 937–14 958, Dec 1998.
- [45] G. P. Agrawal, *Fiber-Optic Communication Systems*, 3rd ed. John Wiley & Sons, 2002.
- [46] J. B. Johnson, “Thermal agitation of electricity in conductors,” *Phys. Rev.*, vol. 32, no. 1, p. 97, Jul 1928.
- [47] H. Nyquist, “Thermal agitation of electric charge in conductors,” *Phys. Rev.*, vol. 32, no. 1, pp. 110–113, Jul 1928.
- [48] G. Cariolaro, C. De Angelis, and N. Laurenti, “Comunicazioni ottiche,” September 2006.